

# POLITECNICO DI TORINO

Corso di Laurea Magistrale  
in Ingegneria Civile

Tesi di Laurea Magistrale

Suction measurements and Resonant Column-Torsional  
Shear (RCTS) testing of expansive clays from Africa



Relatore  
Prof. Renato Maria Cosentini

Candidato  
Marisa Contrafatto

Correlatrice  
Prof.ssa Giulia Viggiani

Anno Accademico 2019/2020

*A Salvatore*  
*Ai miei nonni*



## Table of contents

1. Introduction.....	1
1.1 Background .....	1
1.2 Scope and structure of the thesis.....	2
2. Literature review relating to unsaturated soils behaviour.....	4
2.1 Introduction.....	4
2.2 Definition of partly saturated soil .....	4
2.3 Soil suction: definition and components .....	6
2.4 Stress and volumetric state variables .....	12
2.5 Volumetric behaviour.....	13
2.6.1 State surfaces .....	13
2.6.2 Soil-Water Retention Curve (SWRC).....	14
2.6.2.1 Van Genuchten's model (1980) .....	16
2.6.3 Compressibility .....	18
2.6 Strength criterion.....	19
2.7 Small strains shear stiffness.....	19
2.8.1 Influence of partial saturation on the soil stiffness .....	23
2.8 Constitutive models for partly saturated soils .....	25
2.9 Hydro-mechanical behaviour of partly saturated soils and constitutive models .....	29
3. Tested materials.....	31
3.1 Introduction.....	31
3.2 Origin and composition of African tropical clay soils.....	31
3.3 Localization and sampling procedure.....	35
3.4 Characterisation.....	37
3.4.1 Particle size distribution.....	37
3.4.1.1 Mechanical sieving.....	37
3.4.1.2 Hydrometer sedimentation test.....	38
3.4.2 Atterberg limits.....	42
3.5 Experimental program.....	47

4.	Testing apparatus and methodology.....	49
4.1	Introduction.....	49
4.2	Soil suction and volume change measurement (WP4C).....	49
4.3	Suction-controlled RCTS (Resonant Column Torsional Shear) apparatus	51
4.3.1	RCTS background .....	51
4.3.2	RCTS test interpretation: physical model .....	54
4.3.2.1	Half power bandwidth method .....	61
4.3.2.2	Logarithmic amplitude decay method .....	64
4.3.3	Control of suction: axis translation technique.....	66
4.3.4	Setting up of the new NRFIS suction-controlled RCTS .....	67
4.3.4.1	The excitation system .....	69
4.3.4.2	The electro-mechanical system.....	70
4.3.4.3	The measurement system .....	72
4.3.4.4	Calibration process.....	76
4.3.4.5	RCTS software .....	77
4.3.5	Saturation of the HAEV porous disc under pressure and permeability test .....	79
4.3.6	Saturation of the HAEV porous disc under vacuum .....	82
4.3.7	Preparation of reconstituted samples.....	83
5.	Results.....	85
5.1	Introduction.....	85
5.2	SWRCs.....	85
5.1.1	Black Cotton clay SWRCs and comparison with previous results.....	85
5.1.2	Atta Clay SWRCs and comparison with previous results.....	92
5.1.3	Best fitting Van Genuchten's retention curve.....	96
5.3	RCTS apparatus.....	101
5.2.1	Set-up of the saturated test .....	101
5.2.2	Saturated test ( $p' = 50$ kPa) – Consolidation phase .....	103
5.2.3	Saturated test ( $p' = 50$ kPa) – Cyclic loading phase.....	110
6.	Interpretation of results.....	117
6.1	Comparison of TS experimental results with Darendeli's model.....	123

6.2	Comparison of TS experimental results with Vucetic&Dobry's model (1991) 129	
6.3	Comparison of experimental results with Italian case studies.....	131
7.	Conclusions and future implications .....	140
	REFERENCES .....	144

## Table of figures

Figure 2. 1 – Liquid-gas configurations in unsaturated soils for decreasing degree of saturation.....	5
Figure 2. 2 – Relative humidity as a function of total suction.....	7
Figure 2. 3 – Components of suction (after Fredlund and Rahardjo, 1993) .....	8
Figure 2. 4 – Schematics of air-water interfaces in soils (after Sharma, 1998).....	9
Figure 2. 5 – Increase of contact force between two spheres of equal diameter due to suction (after Fisher, 1926). .....	10
Figure 2. 6 – Voids ratio state surface under isotropic loading (after Matyas and Radhakrishna, 1968) .....	13
Figure 2. 7 – Wetting and drying cycles starting from (a) a point on primary wetting curve or (b) a point on primary drying curve (after Sharma, 1998).....	14
Figure 2. 8 – Water retention curves of soils with different grading (after Vanapalli <i>et al.</i> , 1996).....	15
Figure 2. 9 – (a) initial shear modulus and secant shear modulus, and (b) secant shear modulus decay with strain (after Foti, 2019). .....	20
Figure 2. 10– Definition of damping ratio (after Zhang <i>et al.</i> , 2005). .....	21
Figure 2. 11 – Qualitative variation of normalised shear modulus, damping ratio and excess pore-water pressure with shear strain level (after Lanzo and Silvestri, 1999).....	22
Figure 2. 12– Isotropic compression line for saturated and unsaturated soil, and definition of apparent pre-consolidation net stress (after Alonso <i>et al</i> , 1990).....	25
Figure 2. 13– (a) changes in particles arrangement due to an increase of net stress (loading) and a reduction of suction (collapse) (after Gens and Alonso, 1992) (b) Loading Collapse and suction increase yield loci (after Alonso <i>et al</i> , 1990). .....	26
Figure 2. 14 –(a) BBM yield surface in $(p-u_a)$ : $q$ : $s$ space and (b) its section at constant suction (after Alonso <i>et al</i> , 1990). .....	27

Figure 3. 1 - Textural classification of black cotton soils based on US Engineers soil classification System (after Gidigasú <i>et al.</i> , 2013).....	32
Figure 3. 2 - Distribution of black cotton soils on the total ice-free area of the earth (after Gidigasú <i>et al.</i> , 2013) .....	33
Figure 3. 3 - Distribution of tropical clay soils in Africa with identification of sites of collection of tested clays.....	35
Figure 3. 4 - (a) Atta Clay 70 mm samples from Steelport (South Africa) and (b) Black Cotton Clay 100 mm samples from Al Fao (Sudan) .....	36
Figure 3. 5 – Hydrometer sedimentation test equipment.....	39
Figure 3. 6 – Particle size distribution curve of Atta Clay (South Africa).....	40
Figure 3. 7 – Particle size distribution curve of Black Cotton Clay (Sudan).....	41
Figure 3. 8 - Cone penetrometer test equipment.....	43
Figure 3. 9 – Cone penetrometer test results and liquid limit of Atta Clay (South Africa).....	44
Figure 3. 10 - Cone penetrometer test results and liquid limit of Black Cotton clay (Sudan) .....	45
Figure 3. 11 – Classification of tested clays according to Casagrande plasticity chart.....	46
Figure 3. 12- Black Cotton clay SWRC resulting from a previous study (after Abdalla <i>et al.</i> , 2019).....	48
Figure 4. 1 – Equipment for sample suction and volume measurements.....	50
Figure 4. 2 - (a) Stokoe-type (after Clayton, C. R. I., <i>et al.</i> , 2009) and (b) Hardin-type (after Li, H. <i>et al.</i> , 2018) resonant column apparatus.....	52
Figure 4. 3 - SDOF system configuration .....	55
Figure 4. 4 – Evaluation of soil damping ratio according to the half power bandwidth method.....	56
Figure 4. 5 - Reference dynamic model for RCTS test interpretation (fixed-free configuration) .....	57
Figure 4. 6 – Amplitude-frequency curves for increasing strain levels .....	59
Figure 4. 7 – Amplification factor changes in a SDOF viscous-elastic system under forced oscillations (after Chopra, 2002).....	62

Figure 4. 8 – Dynamic amplification curve and computation of damping ratio (after Chopra, 2002).....	63
Figure 4. 9 – Free-decay trend on the sample head (after Foti, 2019).....	64
Figure 4. 10 – Suction-controlled RCTS apparatus at NRFIS Geomechanics laboratory (University of Cambridge).....	67
Figure 4. 11 – Overall layout of RCTS apparatus at NRFIS Geomechanics laboratory (University of Cambridge).....	68
Figure 4. 12 – Electro-mechanical system of RCTS apparatus.....	71
Figure 4. 13 – High frequencies measurement sensors .....	73
Figure 4. 14 – Details of measurements system of radial volume changes .....	74
Figure 4. 15 – Software control windows.....	77
Figure 4. 16 – (a) Schematic representation of the bottom drainage circuit and cross section of 38 mm HAEV porous stone and (b) picture showing the 38 mm porous stone rigidly fixed to the base.....	79
Figure 4. 17 – Main specifications of the 5 bar standard flow porous stone (SOILMOISTURE EQUIPMENT CORP. CERAMICS CATALOG).....	80
Figure 4. 18 – (a) Equipment for the saturation process of the HAEV porous disc under vacuum and detailed pictures of (b) 50 mm and (c) 38 mm porous discs .....	82
Figure 4. 19 – (a) Initial conditions of slurry in the 100 mm consolidometer after pouring process and (b) 100 mm reconstituted Black Cotton clay sample .....	83
Figure 4. 20 - Consolidation curve plotted in the void ratio-vertical stress plane.....	84
Figure 4. 21 – Consolidation curve plotted in the semi-logarithmic vertical settlement-time plane.....	84
Figure 5. 1 – Black Cotton clay SWRCs and comparison with previous results (after Abdalla <i>et al.</i> , 2019) in the degree of saturation- gravimetric water content plane .....	87

Figure 5. 2 – Black Cotton clay SWRCs and comparison with previous results (after Abdalla <i>et al.</i> , 2019) in the degree of saturation-total suction plane .....	88
Figure 5. 3 – Black Cotton clay shrinkage line and comparison with previous results (after Abdalla <i>et al.</i> , 2019) in the void ratio-gravimetric water content plane .....	89
Figure 5. 4 – Black Cotton clay SWRCs and comparison with previous results (after Abdalla <i>et al.</i> , 2019) in the void ratio-total suction plane.....	90
Figure 5. 5 – Black Cotton clay SWRCs and comparison with previous results (after Abdalla <i>et al.</i> , 2019) in the gravimetric water content-total suction plane .....	91
Figure 5. 6 – Atta clay SWRCs and comparison with previous results (after Abdalla <i>et al.</i> , 2019) in the degree of saturation-gravimetric water content plane .....	92
Figure 5. 7 – Atta clay SWRCs and comparison with previous results (after Abdalla <i>et al.</i> , 2019) in the degree of saturation-total suction plane.....	93
Figure 5. 8 – Atta clay shrinkage line and comparison with previous results (after Abdalla <i>et al.</i> , 2019) in the void ratio-gravimetric water content plane .....	94
Figure 5. 9 – Atta clay SWRCs and comparison with previous results (after Abdalla <i>et al.</i> , 2019) in the void ratio-total suction plane .....	95
Figure 5. 10 – Atta clay SWRCs and comparison with previous results (after Abdalla <i>et al.</i> , 2019) in the gravimetric water content-total suction plane.....	95
Figure 5. 11 – Van Genuchten’s retention curve and comparison with Atta Clay SWRC in the volumetric water content-suction plane.....	97
Figure 5. 12 – Van Genuchten’s retention curve and comparison with Black Cotton Clay SWRC in the volumetric water content-suction plane.....	98

Figure 5. 13 – Van Genuchten’s retention curve and comparison with Atta Clay SWRC in the degree of saturation-suction plane .....	99
Figure 5. 14 – Van Genuchten’s retention curve and comparison with Black Cotton Clay SWRC in the degree of saturation-suction plane .....	100
Figure 5. 15 –Placement of (a) sample, membrane and O-rings and (b) pressure cell, drive system and measurement sensors.....	101
Figure 5. 16 – Loaded project window .....	103
Figure 5. 17 – Consolidation parameters curves as a function of vertical stress from a previous study on two tropical clays (after Al Haj, K., 2014).....	104
Figure 5. 18 – Consolidation curve of tested reconstituted sample .....	106
Figure 5. 19 – Graphical evaluation of consolidation time according to Taylor’s consolidation theory.....	107
Figure 5. 20 – Consolidation curve plotted in the average degree of dissipation-time plane .....	108
Figure 5. 21 – Influence of the coefficient of consolidation on the average degree of dissipation-time curve for a sample thickness equal to 76 mm (after Al Haj, K., 2014) .....	108
Figure 5. 22 – RC test control window: input parameters, accelerometer response and FFT of the amplitude response signal .....	112
Figure 5. 23 – TS test control window: input parameters, excitation-time and response-time curves and hysteresis cycles .....	114
Figure 5. 24 – DECAY test control window: input parameters, free-decay amplitude response and logarithmic amplitude method for the evaluation of damping ratio .....	115
Figure 5. 25 – Sample condition after RCTS tests .....	116
Figure 6. 1 – Normalized shear modulus degradation curve as strain level increases .....	117
Figure 6. 2 – Damping ratio trend as strain level increases.....	118
Figure 6. 3 – Influence of OCR and plasticity index on normalized shear modulus and damping ratio degradation curves (after Darendeli, 2001) .....	118

Figure 6. 4 – Influence of the number of cycles on shear modulus during TS tests.....	119
Figure 6. 5 – Influence of number of cycles on damping ratio during TS tests ...	120
Figure 6. 6 – Comparison between RC and TS test results in terms of shear modulus with respect to strain levels .....	121
Figure 6. 7 – Comparison between RC, TS and DECAY test results in terms of damping ratio with respect to strain levels .....	122
Figure 6. 8 – Effect of plasticity index on (a) normalized shear modulus and (b) damping ratio degradation curves (after Darendeli, 2001).....	123
Figure 6. 9 – Effect of confinement pressure on (a) normalized shear modulus and (b) damping ratio degradation curves (after Darendeli, 2001) .....	124
Figure 6. 10 – Comparison between experimental results (TS test) and Darendeli’s model in terms of normalized shear modulus degradation curve as shear strain increases .....	128
Figure 6. 11 – Comparison between experimental results (TS test) and Darendeli’s model in terms of damping ratio evolution curve as shear strain increases.....	128
Figure 6. 12 – Comparison between experimental results (TS test) and Vucetic&Dobry’s model in terms of normalized shear modulus degradation curve as shear strain increases .....	129
Figure 6. 13 – Comparison between experimental results and Vucetic&Dobry’s model in terms of damping ratio evolution curve as shear strain increases .....	130
Figure 6. 14 – Comparison between Black Cotton clay and Italian case studies in terms of normalized shear modulus degradation curves as shear strain increases (TS test) .....	133
Figure 6. 15 – Comparison between Black Cotton clay and Italian case studies in terms of damping ratio evolution curves as shear strain increases (TS test).....	133
Figure 6. 16 – Comparison between results of TS test on Po river soil, Darendeli’s model and Vucetic&Dobry’s model in terms of	

normalized shear modulus degradation curve as shear strain increases .....	135
Figure 6. 17– Comparison between results of TS test on Po river soil, Darendeli’s model and Vucetic&Dobry’s model in terms of damping ratio evolution curve as shear strain increases .....	135
Figure 6. 18 – Comparison between results of TS test on Montegiorgio soil, Darendeli’s model and Vucetic&Dobry’s model in terms of normalized shear modulus degradation curve as shear strain increases .....	136
Figure 6. 19 – Comparison between results of TS test on Montegiorgio soil, Darendeli’s model and Vucetic&Dobry’s model in terms of damping ratio evolution curve as shear strain increases .....	136
Figure 6. 20 – Comparison between results of TS test on Tolentino soil, Darendeli’s model and Vucetic&Dobry’s model in terms of normalized shear modulus degradation curve as shear strain increases .....	137
Figure 6. 21 – Comparison between results of TS test on Tolentino soil, Darendeli’s model and Vucetic&Dobry’s model in terms of damping ratio evolution curve as shear strain increases .....	137
Figure 6. 22 – Influence of mean effective confining pressure on modulus degradation curves for (a) non plastic (PI=0) soil and (b) plastic (PI=50) soil (After Ishibashi, 1992) .....	138
Figure 6. 23 – Effect of mean effective confining pressure on normalized shear modulus degradation curves for tested plastic soils .....	139

## List of tables

Table 3. 1 -	Liquid limit of tested clays .....	45
Table 3. 2 –	Summary of classification test results .....	46
Table 3. 3 -	Initial conditions of Atta clay samples for suction measurements .....	47
Table 3. 4 -	Initial conditions of Black Cotton clay samples for suction measurements .....	47
Table 4. 1-	Summary of theoretical hydraulic and geometrical properties.....	80
Table 4. 2-	Initial properties of Black Cotton clay slurry .....	83
Table 5. 1 –	Initial hydraulic conditions of Black Cotton clay samples .....	86
Table 5. 2-	Initial hydraulic conditions of Atta clay samples .....	92
Table 5. 3 –	Saturated, residual and average volumetric water contents of Black cotton and Atta clay samples .....	96
Table 5. 4 –	Van Genuchten’s parameters of the best fitting retention curves in the volumetric water content-suction plane .....	97
Table 5. 5 –	Van Genuchten’s parameters of the best fitting retention curves in the degree of saturation-suction plane .....	98
Table 5. 6 –	Initial geometric and physical properties of tested sample.....	103
Table 5. 7 –	Consolidation parameters of Black Cotton clay reconstituted samples .....	105
Table 5. 8 –	Initial sample properties and input parameters .....	110
Table 5. 9 –	Sample and drive system mass polar moment of inertia .....	111
Table 5. 10 –	Amplitude and corresponding shear strain level for each TS test ..	113
Table 5. 11-	Final geometric and physical properties of tested sample .....	116
Table 6. 1 -	Sample properties and input parameters of TS tests.....	126
Table 6. 2 -	Parameters of Darendeli’s model .....	127
Table 6. 3 –	Summary of soil properties and test conditions of each case study .....	132
Table 6. 4 –	Parameters of Darendeli’s model referred to three Italian case studies.....	134

# 1. Introduction

## 1.1 Background

The work described in this thesis was carried out at the University of Cambridge in the wider context of the WindAfrica research project. This is a collaborative effort involving the Universities of Durham, Cambridge, Pretoria, Khartoum and Dar Es Salaam, and aims to develop a set of design guidelines for piled wind turbine foundations in expansive clay supporting the growth of a sustainable energy market in Africa.

Africa has seen rapid economic growth in the last two decades, with a corresponding increase in the demand for energy. The demand of electricity exceeds the supply in 30 African countries and there are about 600 million people in Africa who have no access to electricity: three quarters of the population in East Africa, about half of the people in West Africa and most of those in Southern Africa. However, renewable energy resources are well developed in the continent, since it is estimated that 55% of the world's potential renewable energy sources are located in the African continent and about 35% of the world resources for wind energy.

Even if the potential for wind in Africa exceeds current demand by orders of magnitude, there are several challenges to developing the necessary infrastructure. Designing suitable foundations to sustain the loads typically applied by wind turbines represents a particular challenge. Site investigations have shown that many areas that have been identified as suitable for wind turbines are characterised by expansive soils. These soils are particularly sensitive to soil moisture changes; as the water content of the soil increases during the wet season, the soil swells causing surface heave. During the dry season, shrinkage occurs producing settlements. This seasonal shrink/swell cycle can cause significant damage to buildings directly founded on these soils.

The main research lines of the project include field and reduced scale centrifuge testing of the cyclic response of foundations on unsaturated expansive soils, extensive laboratory studies on samples of soils taken from potential wind energy locations in Africa, and numerical parametric studies of wind turbine foundations with different layouts. The overall aims are to develop a simplified model for foundation deformation and bearing capacity and to provide foundation design guidelines for wind turbines in Africa.

If successful, WindAfrica will accelerate the development of wind energy in Africa by providing reliable and economical foundation solutions, since reductions in the cost of foundations will lower the cost of generation and therefore the energy prices

for consumers. Half of all energy use in Africa involves traditional biomass consumption, which involves health risks due to smoke inhalation and social disparities in wood collection. As a consequence, development of wind energy is not only beneficial for the economy, it will also improve human health, create social benefits and reduce environmental damage.

It is clear that the potential impact of the research will not be confined to select the most appropriate foundation solution to suit unsaturated expansive soil conditions subject to extreme weather conditions, since ground movements also cause significant damage to existing buildings and road pavements in Africa.

## **1.2 Scope and structure of the thesis**

This thesis focuses on the characterisation of two tropical expansive clays from two locations in Africa: Black Cotton Clay from Al Fao, Sudan (SUD) and Atta Clay from Steelpoort, South Africa (SA).

The first part of the thesis is a review of the technical literature on the mechanical and hydro-mechanical behaviour of unsaturated soils. The distribution of tropical clay soils is then described in terms of typical geology and climate, focusing on the localization of the two materials that were tested and discussing the relative sampling procedures.

The second part of the thesis describes the original experimental work that was carried out as part of this dissertation. This included the characterisation of tested materials in terms of grain-size distributions and Atterberg limits, and the experimental determination of their water retention curves and of their small strain mechanical behaviour. Especially, according to the experimental program the hydraulic behaviour of tested materials is investigated under unsaturated conditions, while the dynamic one under saturated conditions. To obtain the water retention curves, suction measurements on drying were carried out on both clays, whereas the dynamic behaviour at small and medium strains, was investigated using a suction-controlled Resonant Column Torsional Shear apparatus (RCTS). This was designed specifically to test partly saturated soils and allows to measure the shear stiffness,  $G$ , and the damping ratio  $D$ , in isotropic stress conditions.

The work is organised as follows:

**Chapter 2** is a review of the available technical literature on the mechanical and hydro-mechanical behaviour of unsaturated soils.

**Chapter 3** describes tropical clay soils distribution in terms of typical geology and climate, focusing on tested materials sampling procedures and the relative localization. Once illustrated the overall background, the same chapter includes

the characterisation of tested materials, in terms of grain-size distributions and Atterberg limits.

**Chapter 4** reports the description of testing apparatus and methodology for two main experimental works. The first involves soil suction measurements, in order to get Soil-Water retention curves of both clays, while the second one aims to investigate clays mechanical behaviour at small and medium strains by using a controlled-suction resonant column torsional shear cell (RCTS). It has been designed specifically for testing partly saturated soils and allows to measure shear stiffness  $G$  and damping factor  $D$ , starting from isotropic stress conditions.

**Chapter 5** describes Soil-Water Retention Curves and RCTS experimental results.

**Chapter 6** presents the interpretation of RCTS data and the comparison with empirical correlations and Italian case studies.

**Chapter 7** includes the conclusions and summary of the present research work and also provides some recommendations for future work.

## **2. Literature review relating to unsaturated soils behaviour**

### **2.1 Introduction**

In the present chapter general principles about the mechanical behaviour of unsaturated soils and main differences with respect to fully saturated soils are presented. It starts from a general definition of unsaturated soil and a classification of pore-water types, followed by the definition of soil-suction and its components. Then, state variables governing unsaturated soils behaviour are presented, by distinguishing volumetric and stress variables. Finally, the main mechanical and hydro-mechanical models and their evolution are shortly described, in order to provide an overall presentation of unsaturated soils behaviour.

### **2.2 Definition of partly saturated soil**

A partly saturated soil is a system made of three phases: solid particles, water and air.

The main difference with respect to saturated soils regards the presence of air and its influence on the interaction between water and aggregates, expressed in terms of three different types of pore-water, known as free, weakly bound and strongly bound water. The specific amount of each category in a given soil volume is linked to dimensions of the host voids and to the type of interaction with the solid particles (Stepkowska, 1990).

The first type (free water) is typically contained in macro-pores and can be distinguished in bulk water, filling some pores between solid particles, and *meniscus* water, which is only placed in correspondence of contact points between two particles with a meniscus-shape (Wheeler and Karube, 1995).

It moves under the effect of hydraulic gradients, while the “weakly bound” water cannot flow freely and, as a consequence, micro-pores remain saturated at natural suction levels.

The third category of pore water is also known as hygroscopic water and it is absorbed and forced to move only along the surface of clay particles.

Weakly and strongly bound water represent the microscopic water content, which depends on the activity of soil minerals, while free water content is influenced by changes in macro-pores dimension.

Fluid phases in partly saturated soils can be classified into three different liquid-gas configurations (see Figure 2. 1), according to Wroth and Houlsby (1985):

- discontinuous gas phase and continuous liquid phase: this situation is typical of high degree of saturation, when air phase exists as single bubbles. An example is given by natural soils immediately above the phreatic line, with a degree of saturation close to 1;
- continuous gas and liquid phase, which corresponds to intermediate values of degree of saturation (from 50 to 85%);
- continuous gas phase and discontinuous liquid phase, with low degree of saturation. it is typical of arid or semi-arid zones, where the dry layer reaches considerable thickness.

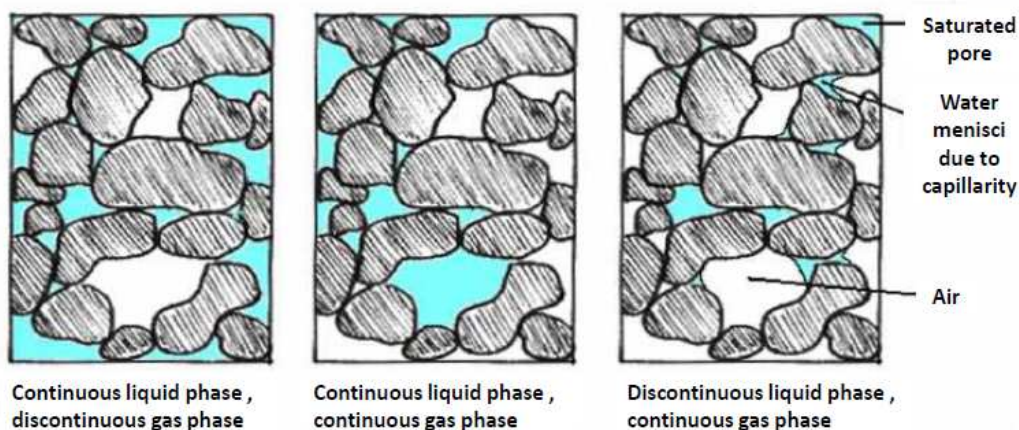


Figure 2. 1 – Liquid-gas configurations in unsaturated soils for decreasing degree of saturation

### 2.3 Soil suction: definition and components

Soil suction is a variable related to the free-energy state of soil-water system and it can be derived by measuring water vapour partial pressure in equilibrium with pore water  $u_v$ , referred to water vapour partial pressure in equilibrium with free water  $u_{v0}$  (Richards, 1965).

The thermodynamic relationship between total soil suction  $\psi$  and the ratio between vapour partial pressures  $u_v/u_{v0}$  is a function of the universal gas constant  $R$ , the absolute temperature  $T$ , the water molar volume  $V_{mol}$ , the water vapour partial pressure in equilibrium with pore water  $u_v$  and the water vapour partial pressure in equilibrium with free water  $u_{v0}$ . This relationship be expressed as:

$$\psi = -\frac{RT}{V_{mol}} \ln\left(\frac{u_v}{u_{v0}}\right) \quad (2.1)$$

The ratio  $u_v/u_{v0}$  is the relative vapour pressure in the air immediately adjacent to water and it is called relative humidity ( $h_r$  or  $RH$ , %); a relative humidity value less than 100% in a soil indicates the presence of suction in the soil.

Figure 2. 2 shows the relationship between relative humidity and total suction corresponding to Equation (2.1).

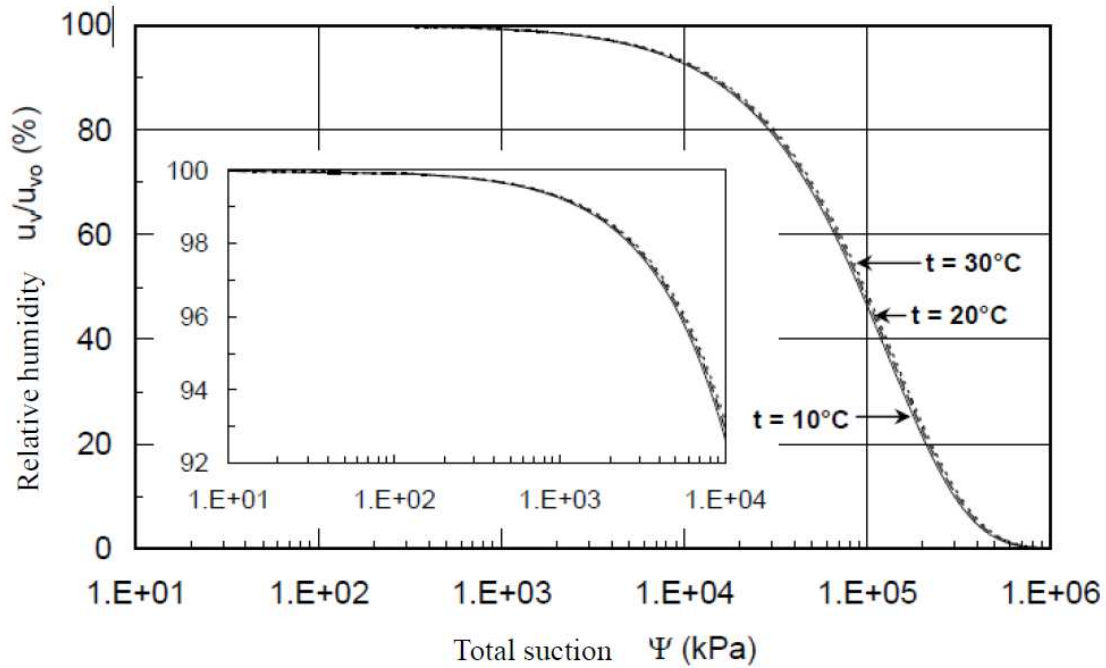


Figure 2. 2 – Relative humidity as a function of total suction

Figure 2. 3 illustrates schematically the two primary components of soil suction, or “matric suction”  $s$  and “osmotic suction”  $\pi$ . The matric component can be derived by measuring water vapour partial pressure in equilibrium with pore water  $u_v$ , referred to water vapour partial pressure in equilibrium with a solution equal to pore-water in composition  $\bar{u}_{v0}$ . As regards the osmotic component, it is the equivalent suction given by measuring water vapour partial pressure in equilibrium with a solution equal to pore-water in composition  $\bar{u}_{v0}$ , referred to water vapour partial pressure in equilibrium with free water  $u_{v0}$ .

By combining the two components, the following equation of total suction  $\psi$  can be derived:

$$\psi = s + \pi = -\frac{RT}{V_{mol}} \ln\left(\frac{u_v}{\bar{u}_{v0}}\right) - \frac{RT}{V_{mol}} \ln\left(\frac{\bar{u}_{v0}}{u_{v0}}\right) \quad (2.2)$$

According to equation (2.2), total suction is equal to the sum of matric suction, which depends on the mechanical interaction between air and water and their pressures, and osmotic suction, which is influenced by the presence of salts in pore-water and their electrostatic interaction with ionic charges surrounding clay particles.

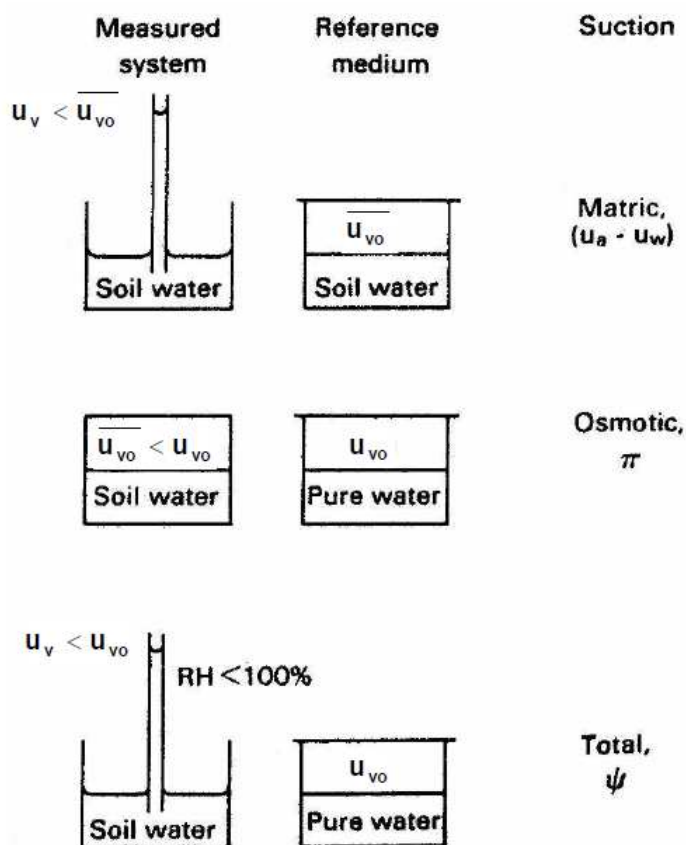


Figure 2. 3 – Components of suction (after Fredlund and Rahardjo, 1993)

Alternatively, according to Miller and Nelson (1993), the matric suction can be defined as the difference between the air and the pore-water pressure  $s = u_a - u_w$ . Due to the phenomenon of capillarity, this difference is higher than zero and this condition corresponds to an air-water interface (meniscus) curved towards the air phase.

The role of the water-air interface can be illustrated with reference to a simplified model, considering a capillary meniscus between two spheres (Figure 2. 4).

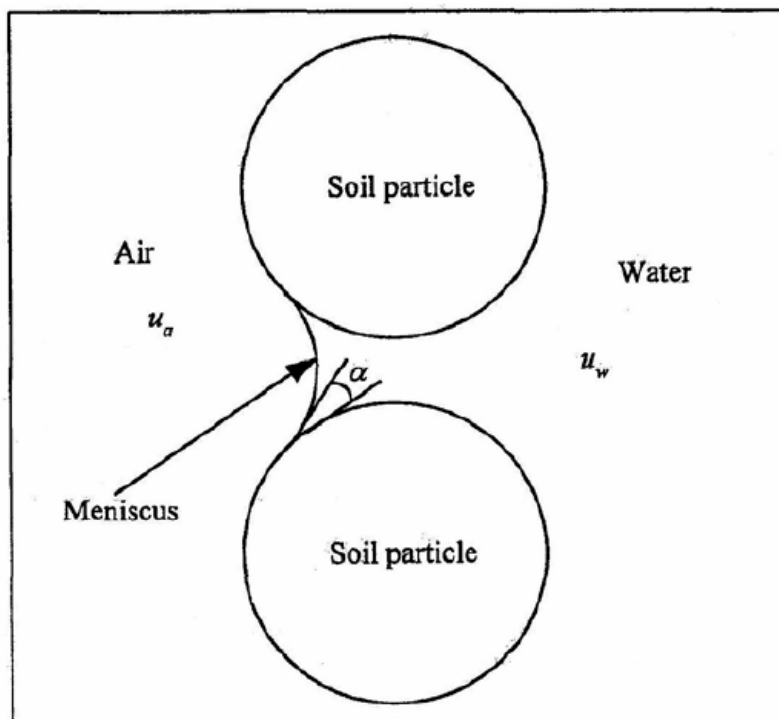


Figure 2. 4 – Schematics of air-water interfaces in soils (after Sharma, 1998)

The interaction between solid particles and pore-fluid is characterised by a contact angle  $\alpha$ , which is often close to zero (Price, 1985) and it corresponds to a curvature towards air phase.

By imposing the equilibrium along the air-water interface, given the surface tension  $T$  and the main curvature radii at the interface  $r_1$  and  $r_2$ , the following relationship valid for matric suction can be obtained:

$$u_a - u_w = T \left( \frac{1}{r_1} + \frac{1}{r_2} \right) \quad (2.3)$$

Usually a generic void has a random shape, characterised by an “ink bottle” configuration with a radius  $\bar{r}$ , computed as the average of different curvature radii at the interface. As a consequence, when measured suction is higher than the corresponding average radius, water comes out from pores with average dimensions bigger than  $\bar{r}$ . This mechanism characterises drying and wetting processes and justifies the hydraulic hysteresis phenomenon.

Figure 2. 5 illustrates a model proposed by Fisher (1926), in order to understand the effect of partly saturation on the frictional behaviour along the contacts between two spherical aggregates. The water meniscus at spheres contacts induces

a force  $\Delta N$  normal to the plane passing through the contact point and orthogonal to the line connecting the centres of the two spheres (Mancuso *et al.*, 2002). This force is only a function of the cross section area of the sphere and the matric suction ( $u_a - u_w$ ), which means that it is equal to zero under saturated condition. During a de-saturation process soil suction decreases and, up to the air-entry value  $s_{ev}$ ,  $\Delta N$  increases at the contact point between two spherical aggregates, according to the following relationship:

$$\Delta N = \frac{\pi D^2}{4} (u_a - u_w) \quad (2.4)$$

where  $D$  is the diameter of the spherical aggregate and  $(u_a - u_w)$  is the matric suction.

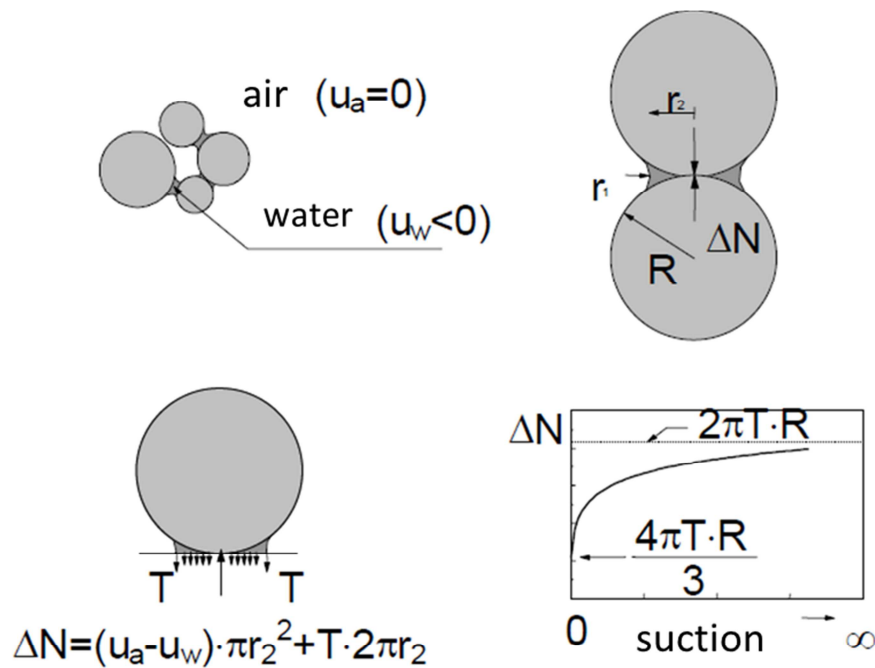


Figure 2. 5 – Increase of contact force between two spheres of equal diameter due to suction (after Fisher, 1926).

According to Fisher's model, under partly saturated condition the presence of soil suction generate an additional contribution in terms of normal force along the contact surface, which leads to an increase of the slip resistance of the two spheres. It follows that unsaturated aggregates of spheres show a stiffer and stronger load response with respect to dry contacts or fully saturated ones (Mancuso *et al.*, 2002).

Following Fisher's model (1926), Sharma (1998) extended it to the case of particles with a flat and long shape and he noticed that the stress increment  $\Delta\sigma$  is constant with suction changes and inversely proportional to particles length.

## 2.4 Stress and volumetric state variables

In saturated soils all measurable effects of change of stress state are due exclusively to a variation of effective stress, according to the definition of effective stress Terzaghi (1936):

$$\sigma' = \sigma - u_w \quad (2.5)$$

In 1959 Bishop proposed to extend this definition to the case of partly saturated soils, in order to take into account the biphasic nature (air and water) of the fluid which fills pores in partly saturated soils. The result is the well-known Bishop's relationship (1959):

$$\sigma' = \sigma - u_a + \chi(u_a - u_w) \quad (2.6)$$

where initially  $\chi = S_r$ , so that for  $S_r = 1$  (saturated case) the definition of effective stress (Terzaghi, 1936) is again obtained.

Then,  $\chi$  became a factor depending on the degree of saturation, varying from 0 (dry soil) to 1 (saturated soil), the soil type and hysteresis effects in wetting and drying process. Following studies led to consider two distinct stress variables (Jennings and Burland, 1962; Bishop and Blight, 1963), since the parameter  $\chi$  is a function of the previous stress history and path (Morgenstern, 1978). As a consequence, three different variables govern the mechanical behaviour of partly saturated soils, pore-air pressure  $u_a$ , pore-water pressure  $u_w$  and total stress  $\sigma$ . Usually they are included in strength criteria by combining them in two independent stress variables: net stress tensor  $|\sigma - u_a|$  and matric suction  $(u_a - u_w)$  (Bishop and Blight 1963).

In the same way the volumetric behaviour of partly saturated soils is described through two independent variables, such as the specific volume  $v$  and the water specific volume  $v_w$ , or specific volume  $v$  and degree of saturation  $S_r$ .

## 2.5 Volumetric behaviour

### 2.6.1 State surfaces

Since the mechanical behaviour of partly saturated soils is commonly described through two independent stress variables, it follows that volumetric strains of saturated soils are due to effective stress changes, while partly saturated soils can be subjected to volumetric changes both for effective stress and matric suction changes.

In order to describe the variation of volume and degree of saturation  $S_r$  as a function of stress state variables, the concept of state surface has been introduced by Matyas and Radhakrishna (1968), on the basis of suction-controlled compression tests. The Authors proposed a double curvature state surface plotted in the  $(\sigma_3 - u_a):e:(u_a - u_w)$  plane, so that both swelling and shrinkage phenomenon could be represented in the same graph. Especially, a decrease of matric suction at low confinement pressure leads to an increase of void ratio (swelling), while a higher confinement  $(\sigma_3 - u_a)$  determines shrinkage effects (Figure 2. 6).

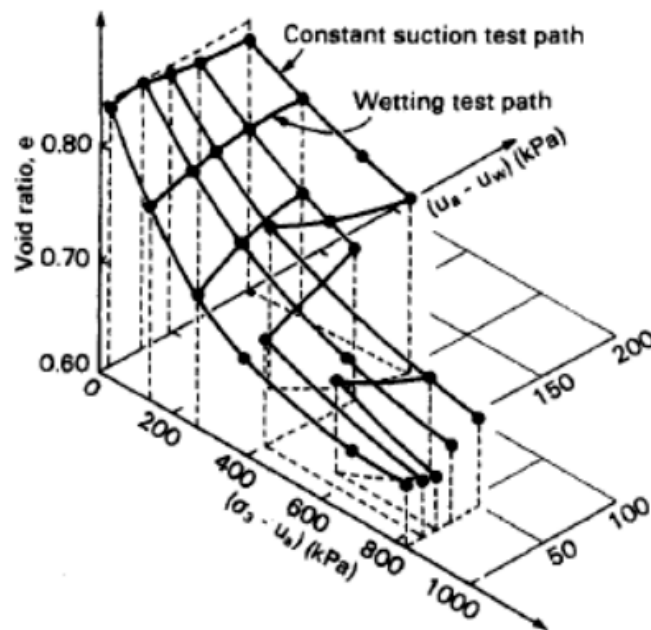


Figure 2. 6 – Voids ratio state surface under isotropic loading (after Matyas and Radhakrishna, 1968)

## 2.6.2 Soil-Water Retention Curve (SWRC)

The Soil-Water Retention Curve (SWRC) is frequently used to investigate the coupled hydro-mechanical behaviour of unsaturated soils (Fredlund *et al.*, 1993) and it is commonly plotted in a semi-logarithmic plane as a function of suction ( $s$ ) and either degree of saturation ( $S_r$ ), void ratio ( $e$ ), volumetric water content ( $\theta_w$ ), or gravimetric water content ( $w$ ).

Usually SWRCs have a sigmoidal form and drying and wetting curves are distinct, since for the same value of suction the water content reached in the wetting path is lower than in the drying one. Starting from fully saturated reconstituted samples, the first segment of SWRCs is called primary drying curve (PDC), since it derives from an incremental drying process up to residual degree of saturation  $S_r$ , which remains constant. Then, the primary wetting curve (PWC) can be derived by adding small amounts of water to the samples and measuring suction at each step.

In Figure 2. 7 wetting and drying cycles are illustrated, by distinguishing two different initial configuration.

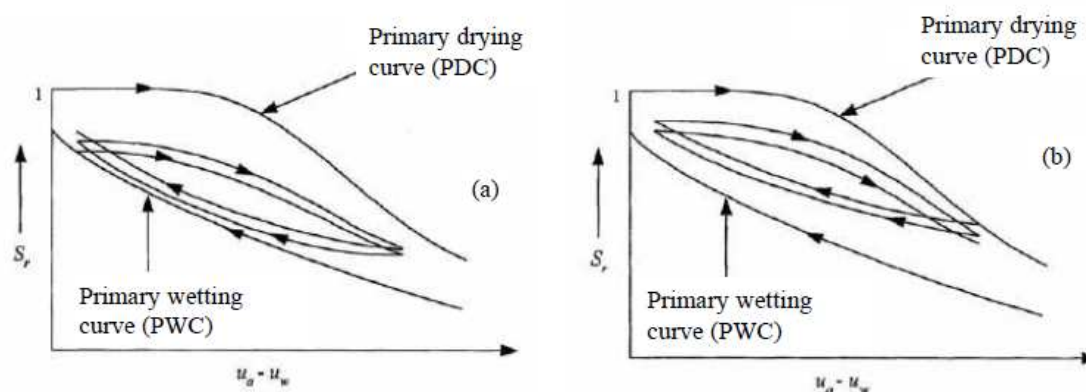


Figure 2. 7 – Wetting and drying cycles starting from (a) a point on primary wetting curve or (b) a point on primary drying curve (after Sharma, 1998)

If drying starts from slurry, the two curves (PDC and PWC) are considered to be boundary curves, which means that any intermediate sample condition is represented through a point  $(u_a - u_w; S_r)$  placed inside the area delimited by these boundaries. Usually, the end of the wetting curve differs from the starting point of the drying curve and, as a consequence, the process of drying and wetting is hysteretic (Abdalla *et al.*, 2019). From a microscopic point of view, hydraulic hysteresis is caused by the different configurations of pore-water, *i.e.* bulk water and menisci water.

If small wetting and drying cycles take place from positions along the PDC or PWC, intermediate curves are created within the primary curves called scanning curves (Al Haj & Standing, 2016).

The retention curve depends on the voids distribution, such as the grain-size distribution and the texture of the material, as shown in Figure 2. 8. In general, a decrease of the average particle size corresponds to an increase of the air-entry value, which is defined as the matric suction value that must be exceeded before air recedes into the soil pores (Fredlund and Rahardjo, 1993).

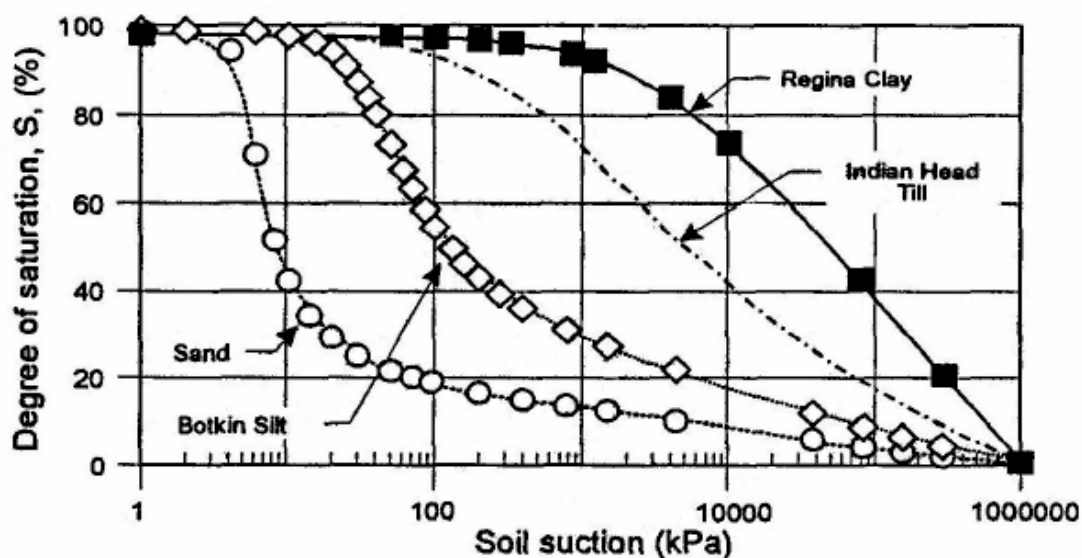


Figure 2. 8 – Water retention curves of soils with different grading (after Vanapalli *et al.* , 1996)

In literature different empirical correlation are available to reproduce SWRCs trend and the most common model is the one proposed by Van Genuchten (1980), which is presented in details in the following section.

### 2.6.2.1 Van Genuchten's model (1980)

In 1980 Van Genuchten developed a methodology to estimate soils permeability curves under unsaturated conditions, in terms of an analytical formulation on the basis of Mualem's model (1976).

In 1976 Mualem derived the following equation as permeability curve:

$$K_r(h) = \theta^{\frac{1}{2}} \left[ \frac{\int_0^\theta \frac{1}{h(x)} dx}{\int_0^1 \frac{1}{h(x)} dx} \right]^2 \quad (2.7)$$

where  $K_r = \frac{K(h)}{K_s}$  is called relative conductivity,  $\theta = \frac{\theta - \theta_r}{\theta_s - \theta_r}$  is called dimensionless water content and it is a function of residual  $\theta_r$  and saturated  $\theta_s$  volumetric water content and  $h$  is the absolute value of pressure head (suction).

Equation (2.7) is an integral equation, which usually can be only solved numerically. Van Genuchten proposed to express dimensionless water content  $\theta$  according to the following relationship

$$\theta = \left[ \frac{1}{1 + (\alpha h)^n} \right]^m \quad (2.8)$$

which can be written in explicit form as

$$\theta = \theta_r + \frac{\theta_s - \theta_r}{[1 + (\alpha h)^n]^m} \quad (2.9)$$

Equation (2.8) describes a type of function compatible with the shape of experimental retention curves, since it is characterised by a S-shape trend and  $\frac{d\theta}{dh}$  values tend to zero for water content levels equal to residual and saturated ones.

By solving (2.7) together with Van Genuchten condition (2.9), it results that

$$K_r(\theta) = \theta^{1/2} \left[ 1 - \left( 1 - \theta^{\frac{1}{m}} \right)^m \right]^2 \quad (2.10)$$

which represents a closed-form solution of Mualem's integral.

It follows that soil permeability and retention curves are uniquely defined once known  $\theta_r$ ,  $\theta_s$ ,  $n$  and  $\alpha$  values, since it is valid the relationship  $m = 1 - \frac{1}{n}$ .

The saturated volumetric water content  $\theta_s$  can be identified through geotechnical surveys on soil samples, while  $\theta_r$  value theoretically is the lower water content that can be reached by increasing suction levels. Since usually water content measuring systems do not allow to reach high suction levels, Van Genuchten's theory allows to assume  $\theta_r (s = -15000 \text{ cm})$ .

As regards  $\alpha$  and  $n$  parameters, the author proposed the following procedure, based on an already measured or estimated retention curve.

The parameter  $n$  can be estimated by deriving  $m$  value through the following equation

$$S_p = 1,151 \frac{m}{1-m} \left( 1 - 2^{-\frac{1}{m}} \right) \quad (2.11)$$

where

$$S_p = \frac{1}{\theta_s - \theta_r} \left| \frac{d\theta}{d(\log h)} \right|_{\theta=\theta_p} \quad (2.12)$$

$$\theta_p = \frac{\theta_s + \theta_r}{2} \quad (2.13)$$

In equation (2.12)  $\frac{d\theta}{d(\log h)}$  is the slope of measured retention curve on a semi-logarithmic plane, corresponding to middle point P between residual and saturated state. Once evaluated the slope,  $m$  parameter can be derived through equation (2.11) by using a numerical solver (Excel) and, as a consequence,  $n$  parameter results as a function of the slope of the retention curve and of residual and saturated water contents.

Finally, the parameter  $\alpha$  can be derived by inverting the following equation

$$h_p = \frac{1}{\alpha} \left( 2^{\frac{1}{m}} - 1 \right)^{1-m} \quad (2.14)$$

where  $h_p$  represents the suction value corresponding to  $\theta_p$  along the measured retention curve. It means that  $\alpha$  parameter identifies the suction level at which air starts to enter inside the porous media, starting from saturated condition.

### **2.6.3 Compressibility**

The compressibility of partly saturated soils is usually investigated through isotropic compression tests or suction-controlled oedometer tests. Similarly to saturated conditions, unsaturated soils show an elastoplastic behaviour along the first loading path, while the following loading and unloading stages are characterised by reversible volume changes. On the basis of results obtained by Josa *et al.* , 1987; Sivakumar, 1993; Rampino *et al.* , 1999a, an increase of suction leads to an increase of the pre-consolidation net stress, which is related to the stabilizing effect of the capillary menisci.

In unsaturated soils a decrease of suction at constant average net stress can lead to positive or negative volume changes (swelling or shrinkage), depending on the initial and final value of suction, the confinement pressure, the previous stress history and the texture of the material (Vassallo, 2003). From a microscopic point of view, according to Fisher (1926) a progressive decrease of suction leads to a decrease of the normal force acting along the surface of contact between two aggregates. As a consequence, the whole stress is applied on solid skeleton and the structural volumetric collapse happens. According to the experimental results by Suriol *et al.* , 1998 the microstructure induced by compaction influences the occurrence of volumetric collapse, since wet optimum compaction tends to produce a more homogeneous, matrix-dominated soil fabric with a single pore-size distribution, while dry of optimum compaction leads to material more susceptible to collapse, due to bimodal pore-size distribution (Mancuso *et al.*, 2002).

## 2.6 Strength criterion

In unsaturated soils the presence of capillary menisci at contact points between solid particles leads to an increase of normal stress and, as a consequence, an increase of shear strength. It follows that in unsaturated soils shear strength is a function of net stress ( $\sigma - u_a$ ) and matric suction ( $u_a - u_w$ ).

In order to take into account the suction effect on shear strength, Fredlund *et al.* (1978) proposed the following equation, by extending the Mohr-Coulomb criterion to the condition of partial saturation:

$$\tau = c' + (\sigma - u_a)\tan\varphi' + (u_a - u_w)\tan\varphi_b \quad (2.15)$$

where  $c'$  and  $\varphi'$  are effective cohesion and friction angle under saturated conditions, while  $\varphi_b$  represents a friction angle that describes the increase of strength due to suction changes. Gan *et al.* (1988) demonstrated that  $\varphi_b$  parameter varies with suctions and for null suction it results  $\varphi_b \sim \varphi'$ , which is valid until suction level reaches the air-entry value.

## 2.7 Small strains shear stiffness

The mechanical response of soils to cyclic loads is characterised by non-linear behaviour, plasticity and energy dissipation and a progressive degradation of mechanical parameters, with an increasing number of applied loading cycles.

However, in earthquake geotechnical engineering applications, the soil is often assumed to behave as a viscous-elastic material, characterised by a shear modulus,  $G$ , and a damping ratio,  $D$ . Non-linearity is introduced assuming that both  $G$  and  $D$  depend on strain level.

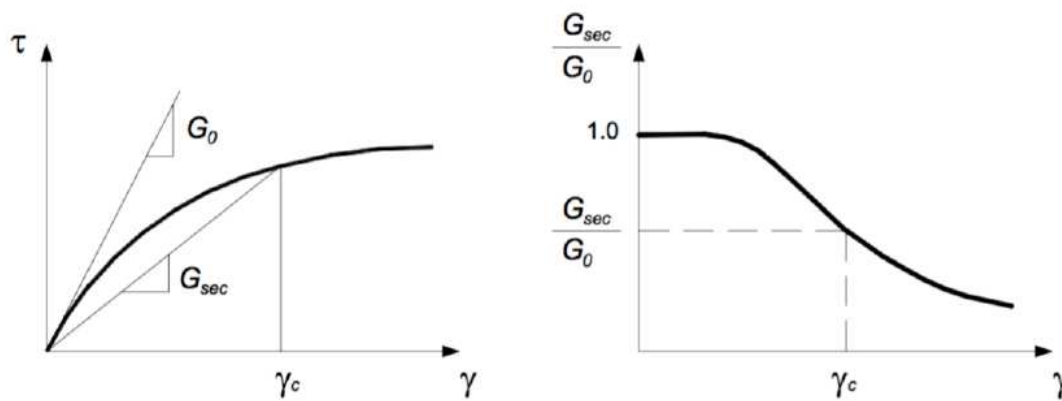


Figure 2. 9 – (a) initial shear modulus and secant shear modulus, and (b) secant shear modulus decay with strain (after Foti, 2019).

Figure 2. 9(a) defines the initial tangent shear modulus,  $G_0$ , and the secant shear modulus,  $G_{sec}$ , at any shear strain,  $\gamma_c$ . Figure 2. 9(b) shows the typical decay of secant shear modulus with the logarithm of shear strain; this is generally represented as a normalised curve, dividing the secant shear modulus at any strain by the initial tangent shear modulus  $G_0$ , which corresponds to the maximum value.

The other fundamental aspect of soil behaviour under cyclic loads is energy dissipation during loading and unloading paths. The parameter used to represent energy dissipation is the damping ratio  $D$ , which is defined as the ratio between the energy dissipated for each loading cycle  $\Delta W$  and the accumulated elastic deformation energy  $W$ , see Figure 2. 10. Experimental observations indicate that the cycles of hysteresis become larger as the shear strain increases, which corresponds to higher energy dissipation.

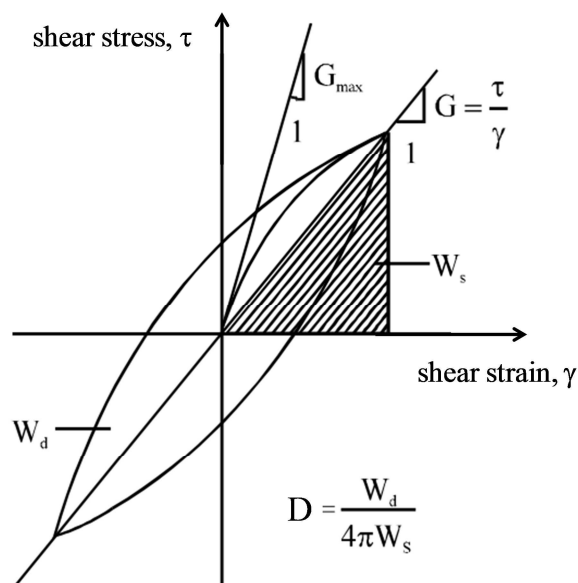


Figure 2. 10– Definition of damping ratio (after Zhang *et al.*, 2005).

Figure 2. 11 shows the qualitative trends of normalised shear modulus, damping ratio and excess pore-water pressure with shear strain level.

Two reference threshold strains can be identified: the cyclic linear threshold strain,  $\gamma_L$ , and the cyclic volumetric threshold strain,  $\gamma_V$  (Vucetic&Dobry, 1991). Below the linear threshold, in the range of the very small strains, the soil response can be represented using a linear elastic or linear viscous-elastic constitutive law, in which the shear modulus is constant and equal to its maximum value  $G_0$ , and the damping ratio is very small and constant.

For strains larger than  $\gamma_L$  but smaller than  $\gamma_V$ , in the range of small to intermediate strains, the shear modulus starts to decay significantly with strain amplitude and increasing values of damping ratio are observed. Soil behaviour is stable, which means that there is no degradation of shear modulus with increasing number of cycles. In this strain range, soil behaviour can be modelled using a non-linear or equivalent linear viscous-elastic model, in which non linearity is introduced by taking into account the dependence of the constitutive parameters, namely  $G$  and  $D$ , on the strain level.

For strains larger than  $\gamma_V$ , the behaviour is strongly non-linear and hysteretic. The main difference with respect to soil behaviour showed up to the volumetric threshold, where shear and volumetric behaviour are de-coupled, *i.e.*, no volume strains are observed in drained conditions and no excess pore water pressures are generated for undrained shearing, for strains larger than the volumetric threshold,

shear and volumetric behaviour are coupled. Such a coupling is a clear indication of plasticity, with significant generation of excess pore water pressures in undrained conditions. The increase of pore-water pressure determines a decrease of soil stiffness at each loading cycle. This type of behaviour can only be described using sophisticated non-linear models.

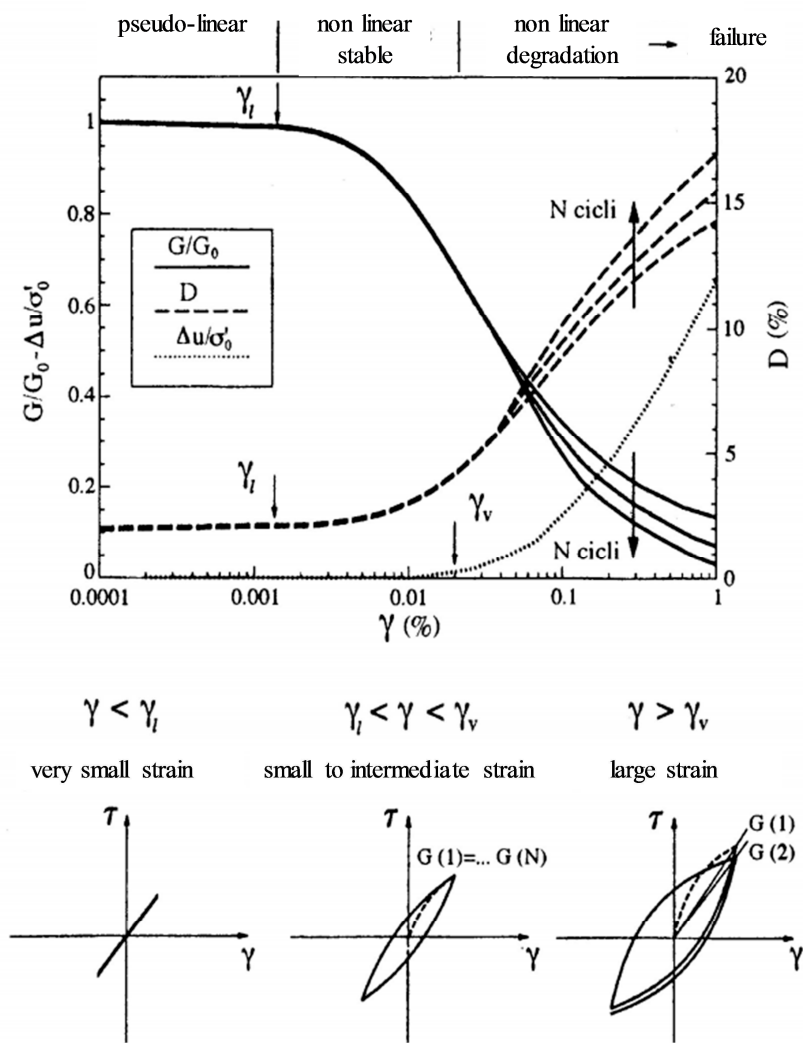


Figure 2.11 – Qualitative variation of normalised shear modulus, damping ratio and excess pore-water pressure with shear strain level (after Lanzo and Silvestri, 1999).

Modulus and damping ratio decay curves depend on soil parameters and physical properties. One of the main factors influencing the degradation of the mechanical properties is the grain-size distribution, since finer grained soils with more inter-particle contacts usually lead to an increase of the linear threshold. For clays, the

linear threshold increases with increasing plasticity index, whereas for sands it increases with increasing confining stress.

Many authors have examined experimentally the factors affecting the cyclic behaviour of soils in the small to medium strain range. Hardin and Black (1968) interpolated experimental results of tests on sand and proposed a relationship for the initial shear stiffness  $G_0$ , in which the small strain stiffness depends non linearly on stress and a function of the voids ratio. This relationship was later extended to normal and over-consolidated clays (Hardin and Black, 1969) by adding one term to account for the over-consolidation ratio.

However, it was later recognised that for clays the effective stress, the voids ratio and the over consolidation ratio are linked by the clay compressibility and cannot be assigned arbitrarily, and alternative formulations that kept the structure of Hardin and Black (1969) were proposed (Rampello et al., 1995).

Effects of the confinement time, which means an increase of stiffness during secondary consolidation, are expressed through dimension-less coefficient  $N_G$ , equal to the variation of  $G_0$  during a logarithmic time cycle with respect to the shear stiffness modulus at a reference time (Anderson and Stokoe, 1978).

Isenhower (1979) proposed a coefficient  $N_\gamma$ , related to strain rate effects on small shear stiffness in terms of the increment for each logarithmic cycle of strain rate with respect to the stiffness at a reference strain rate.

### 2.8.1 Influence of partial saturation on the soil stiffness

Wu *et al.* (1984) and Quian *et al.* (1991) measured small strain stiffness of different unsaturated soils by using a traditional resonant column, without controlling soil suction. The investigation focused on the initial shear modulus,  $G_0$ , and the degradation curve  $G(\gamma)$  obtained for a given applied confining pressure at a given degree of saturation. This experimental procedure allows only for resonant column tests at a suction level equal to the initial one, which means that soil samples can be only subjected to loading and unloading paths without drying and wetting processes (suction changes).

Later, Marinho *et al.* (1995) performed bender elements tests on London clay samples, measuring sample suction using the filter paper technique, while Cabarkapa *et al.* (1998, 1999) used a suction-controlled triaxial cell based on the axis-translation technique to measure soil suction and bender elements to investigate initial shear modulus  $G_0$ . Their results showed the effect of net stress and suction on initial stiffness and were interpreted by extending the equation

proposed by Viggiani and Atkinson (1995) for saturated soils to unsaturated conditions, as shown in the following relationship:

$$\frac{G_0}{p_{ref}} = A (u_a - u_w) \left( \frac{p - u_a}{p_{rif}} \right)^n OCR^m \quad (2.16)$$

where A, n and m are material constants and  $p_{ref}$  is a reference pressure,  $p_{ref} = 1$  kPa.

## 2.8 Constitutive models for partly saturated soils

The first elastoplastic model for unsaturated soils, Barcelona Basic Model (BBM), was proposed by Alonso *et al.* (1987) and then by Alonso *et al.* (1990) in terms of constitutive equations. BBM is an extension to partly saturated conditions of the elastoplastic model for saturated soils, Modified Cam-Clay. It can be applied to moderately expansive unsaturated soils and it aims to reproduce swelling and collapse phenomena, the dependency of specific volume changes on stress paths, irreversible volume decreases due to suction increase and the increment of the apparent cohesion due to suction increase.

The approach by Alonso and co-workers starts from the definition of a yield curve (Figure 2. 12) in the isotropic plane  $(p - u_a):(u_a - u_w)$ . This is then extended to define the yield surface in the stress space  $(p - u_a):q:(u_a - u_w)$ .

Similarly to the saturated case, the Authors proposed the following virgin line equation correspondent to a generic suction level  $(u_a - u_w)$ , a specific volume  $N$  and the corresponding mean net stress  $p^c$  :

$$v = N(u_a - u_w) - \lambda(u_a - u_w) \ln \frac{p - u_a}{p^c} \tag{2.17}$$

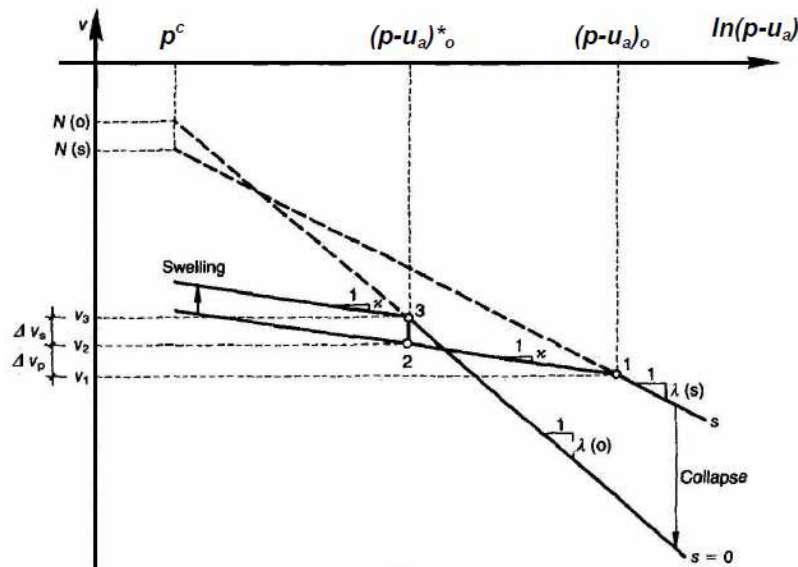


Figure 2. 12– Isotropic compression line for saturated and unsaturated soil, and definition of apparent pre-consolidation net stress (after Alonso *et al.*, 1990).

Equation (2.17) defines a surface in the  $(p - u_a):(u_a - u_w):v$  space, along which elastoplastic strains develop.

The Authors stated that the yielding locus is called LC (Loading Collapse) and it is obtained through a loading path at constant suction (Loading), but it represents also yielding due to suction decrease at constant average net stress, or wetting collapse (Collapse), see Figure 2. 13(a). In order to reproduce the plastic volume changes due to an increase of suction, another yield locus, namely the Suction Increase (SI) locus, is defined as a straight and horizontal line in the  $(p - u_a):(u_a - u_w)$  plane (Figure 2. 13(b)), according to the following equation:

$$(u_a - u_w) = (u_a - u_w)_o \quad (2.18)$$

where  $(u_a - u_w)_o$  is the maximum suction experienced by the soil during its stress history.

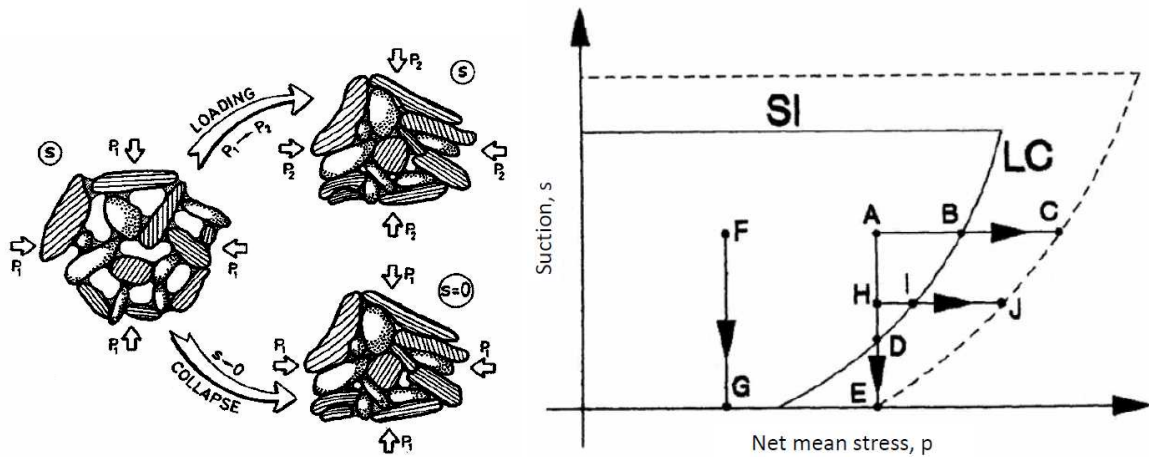


Figure 2. 13– (a) changes in particles arrangement due to an increase of net stress (loading) and a reduction of suction (collapse) (after Gens and Alonso, 1992) (b) Loading Collapse and suction increase yield loci (after Alonso *et al*, 1990).

In order to reproduce anisotropic stress paths, a third stress variable is introduced (deviatoric stress,  $q$ ) and the yield surface is obtained by extending the modified Cam-Clay ellipse to the  $(p - u_a):q:(u_a - u_w)$  space for positive suctions, see Figure 2. 14.

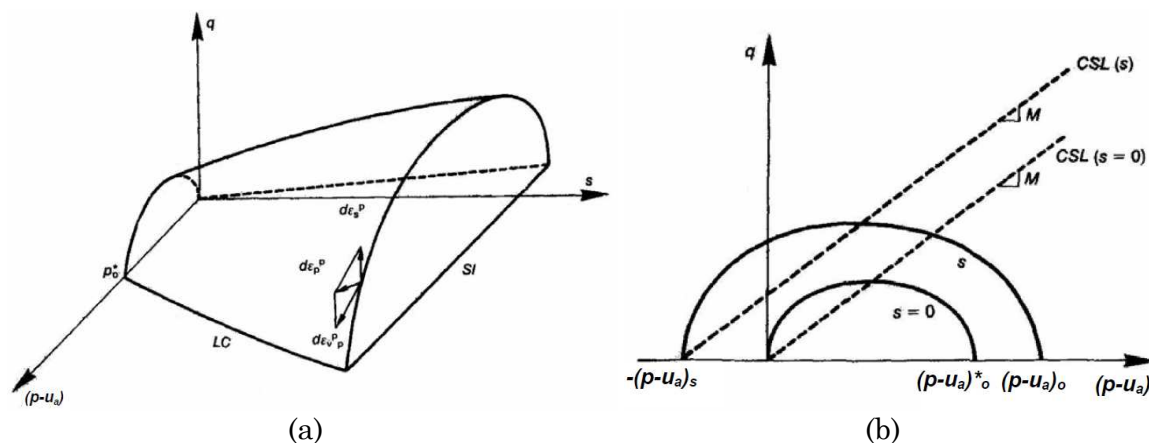


Figure 2.14 –(a) BBM yield surface in  $(p-u_a): q: s$  space and (b) its section at constant suction (after Alonso *et al.*, 1990).

Failure corresponds to a Critical State Line (CSL), parallel to that one under saturated condition, but with a non-zero intercept corresponding to the apparent cohesion. According to Alonso *et al.* (1990) the apparent cohesion is a function of matric suction through a material coefficient  $K$ , as expressed by the following equation:

$$q = M \cdot (p - u_a) + M \cdot K \cdot (u_a - u_w) \quad (2.19)$$

Wheeler and Sivakumar (1995) proposed a modified version of the model by Alonso *et al.* (1990). The main difference is related to the introduction of limit state relationships in terms of stress and specific volume.

Results of isotropic compression tests at constant suction performed by Sivakumar (1993) showed that virgin compression lines are characterised by an increase of the compressibility index  $\lambda$  with suction. For the Loading Collapse locus, the Authors used the same equation as Alonso *et al.* (1990), considering the atmospheric pressure in place of the pre-consolidation pressure.

Triaxial stress paths are obtained by associating to each suction level  $(u_a - u_w)$  a critical state line in the  $(p - u_a): q: v$  space:

$$q = M(u_a - u_w)(p - u_a) + \mu(u_a - u_w) \quad (2.20)$$

$$v = \Gamma(u_a - u_w) - \Psi(u_a - u_w) \ln \frac{(p - u_a)}{p_{atm}} \quad (2.21)$$

where  $M$ ,  $\mu$ ,  $\Gamma$  and  $\Psi$  vary with suction.

Gens and Alonso (1992) modified the original formulation of BBM by Alonso *et al.* (1990) by introducing a double structure level, consisting of a saturated microstructure, made of clay particle aggregates, and an unsaturated macrostructure, characterised by bigger voids.

The Authors stated that the microstructure develops only elastic strains, while macro-structural behaviour depends on microstructure, since microstructure swelling can cause an increase of the global void ratio and, as a consequence, a softening. According to this model, the yield curve, called neutral line, is a straight line with a 45° orientation on the ( $p - u_a$ ) axis.

## 2.9 Hydro-mechanical behaviour of partly saturated soils and constitutive models

The constitutive models described so far (Alonso *et al.* 1990, Gens and Alonso, 1992) consider the stress-strain relationship for unsaturated soils solely in terms of changes of specific volume. In order to introduce the degree of saturation as a characteristic variable in the previous models, a soil-water retention curve is often developed together with the model governing specific volume changes.

Wheeler (1996) was the first to introduce water content changes in an elastoplastic model. The main limitation of Wheeler's model is that it is capable of interpreting the behaviour of an unsaturated soil only if its suction is lower than the maximum value in its previous history. The author assumed that unsaturated soils are usually made of saturated particle aggregates, where micro-pores filled with water up to very high suction levels and macro-pores characterised by more relevant water content changes. In his model Wheeler included the specific water volume in an elastoplastic model based on limit state theory in unsaturated conditions.

Then Buisson and Wheeler (2000) proposed a model by taking into account the phenomenon of hydraulic hysteresis and irreversible volume changes related to wetting and drying processes. The phenomenon of hydraulic hysteresis influences the response of partly saturated soils to applied stress, since the presence of the capillary meniscus leads to an increase of inter-particle strength due to the normal forces  $\Delta N$ , as described by Fisher's model (1926). During a drying process, suction progressively decreases and the soil response is only governed by net stress ( $p - u_w$ ). As a consequence, soil behaviour in terms of irreversible strains changes between drying and wetting paths. Due to the hydraulic hysteresis, the same value of suction corresponds to two different degrees of saturation, which means that the number of water-filled and air-filled voids is different between wetting and drying paths (Vassallo, 2003).

Vaunat *et al.* (2000) proposed an elastoplastic model, which takes into account the coupling between specific volume changes and water specific volume ones. The model takes the void ratio and water void ratio as state variables and integrates the formulation by Alonso *et al.* (1990) with a water retention curve, to describe the hydro-mechanical behaviour.

The model proposed by Vaunat *et al.* (2000) is valid in a single direction, in terms of influence of mechanical behaviour on SWRCs. In order to take into account both directions of hydro-mechanical coupling, Wheeler *et al.* (2003) introduced a new model restricted to isotropic stress state only, by adding a second stress state variable, namely modified suction, to the already known Bishop's stress tensor.

This model was later modified by Lloret-Cabot *et al.* (2017) in order to include both isotropic and anisotropic stress state, by considering an additional deviator stress.

### **3. Tested materials**

#### **3.1 Introduction**

Natural disturbed soils were collected from two locations in Africa: a Black Cotton clay from Al Fao (Sudan) and Atta clay from Steelpoort (South Africa), both of which are expansive soils. The first part of the following chapter focuses on literature review related to tropical clay soils, in terms of mineralogy, pedogenic process, main constituents and typical distribution on the earth area. Climate characteristics of Sudan and South Africa are shortly illustrated, since tested materials are particularly sensitive to soil moisture changes.

In the second part, results of material characterisation and details of the sampling procedure, in terms of location site, geological profile, number of boreholes and sampling intervals, are presented. Characterisation results include soil particle size distribution (PSD) by sedimentation hydrometer analysis, and Atterberg liquid limit by using fall cone method.

#### **3.2 Origin and composition of African tropical clay soils**

Tropical sedimentary clays are poor materials, which are typically found in temperate zone. One of the main fundamental properties of this material is the presence of expansive clay minerals, among which montmorillonite, which are responsible of a highly active and expansive behaviour. As a consequence, the interaction of such clay soils with water leads to volumetric changes, *i.e.* swelling and shrinkage due to wetting and drying processes respectively (Morin, 1971).

The adjective “black” derives from typical colour black or greyish black, directly linked to the mineralogical composition involving clay minerals of smectite group (montmorillonite, kaolinite, halloysite and illite), while the denomination “cotton” seems to come from Indian cotton crops, growing on such tropical soils (Gidigasú *et al.*, 2013).

The most common process of formation of black cotton clays is called “weathering”, which is a pedogenic process starting from the disintegration and decomposition of rocks (Gidigasú *et al.*, 2013). The first stage regards the earth surface level and involves all physical processes of decreasing in size of rocks, while the second one starts when chemically active components of the atmosphere interact with rocks. Then it involves deeper layer through the action of water and leads to biological processes of formation of secondary products.

The physical process regards igneous, sedimentary and metamorphic rocks, while chemicals react especially with mafic igneous rocks (basalt, norite, andesites ..), forming hydrous oxides which develop in clay minerals under suitable conditions (Gidigasú *et al.*, 2013). As regards fundamental properties of African tropical clays, plasticity and high water resistance derive from the absence of quartz, while swelling problems are linked to the presence of magnesium and calcium.

On the basis of classification by Morin (1971), a single trend in tropical soil behaviour cannot be identified, both in terms of the natural moisture content in a profile and the index properties, including silt content (from 58 to 90 %) and clay fraction (from 40 to 70%). Most of the soils is basic (pH values from 6.3 to 9.2).

Figure 3. 1 shows the textural classification of two examples of black cotton soils.

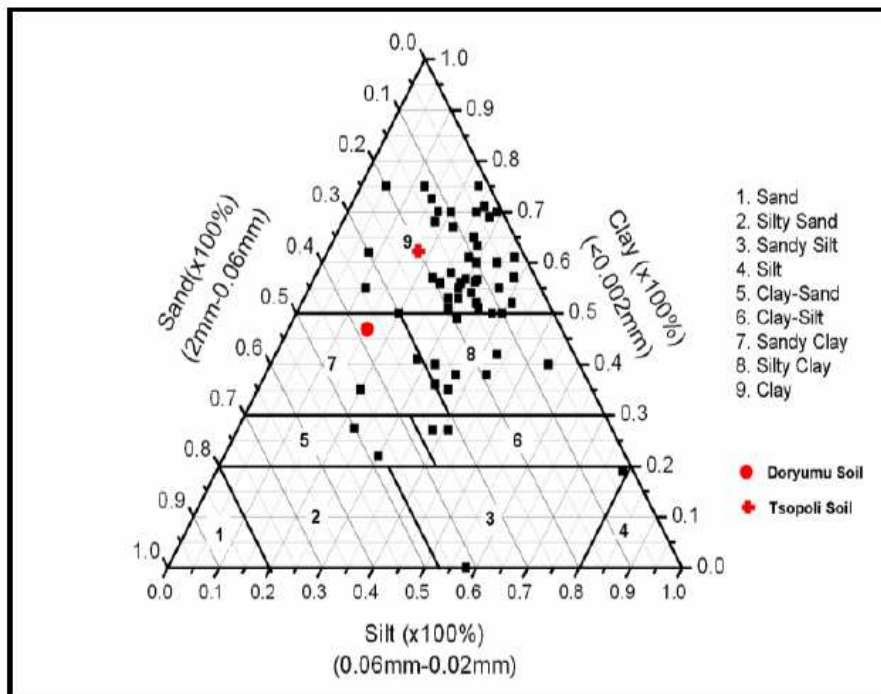


Figure 3. 1 - Textural classification of black cotton soils based on US Engineers soil classification System (after Gidigasú *et al.*, 2013)

A similar variability regards Atterberg limits, with liquid limits varying from 28 to 190 % and plasticity indices from 14 to 145 %. On the basis of these classification properties, Black cotton soils are normally plotted above the A-line and classified as inorganic clay of low to very high plasticity on the Casagrande’s chart (Gidigasú *et al.*, 2013).

As regards Classification Systems, the denomination usually attributed to Black cotton soils are: A-7-5 and A-7-6 by the AASHTO Classification System, CH and CL

by the Unified Soil Classification System and clay, sandy-clay, silty-clay on the U.S. Engineers textural classification chart.

In terms of distribution on the earth surface, black cotton soils are mostly present in Africa, India and Australia, as shown in Figure 3. 2.

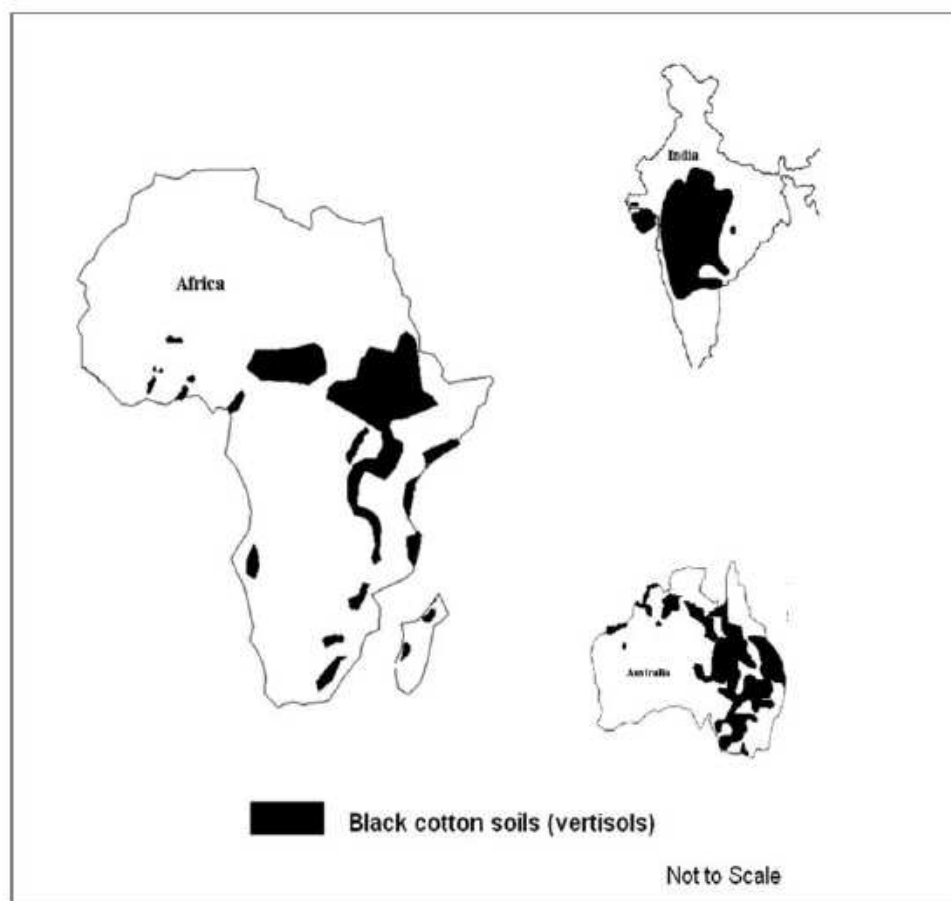


Figure 3. 2 - Distribution of black cotton soils on the total ice-free area of the earth (after Gidigasú *et al.*, 2013)

According to the climatic classification of Köppen (1931), Sudanese regions are typically arid or semi-arid zones with a low-latitude dry climate (Buursink 1971). Such a dry climate leads to shrinkage and cracking phenomena for much of the year, followed by swelling during wet seasons.

As regards South Africa, three main types of climate are identified: Mediterranean in the southwestern corner of the country, temperate in the interior plateau and subtropical in the northeast., together with desert climate interesting a small area in the northwest. Rainfall generally occurs during summer (November through

March) all over the country, but in the southwest often occurs in winter (June through August).

Average temperatures range in a little interval from south to north and maximum temperatures often exceed 32°C in the summer and reach 38°C in some areas of the far north.

By referring to annual rainfall, it remains below 200 mm in the northwest, while the eastern climate is the wettest one, since rainfall level varies from 500 mm to 900 mm with occasional peak of 2,000 mm. The central area is characterised by an intermediate rainfall level (about 400 mm), with a wide variation closer to the coast.

### 3.3 Localization and sampling procedure

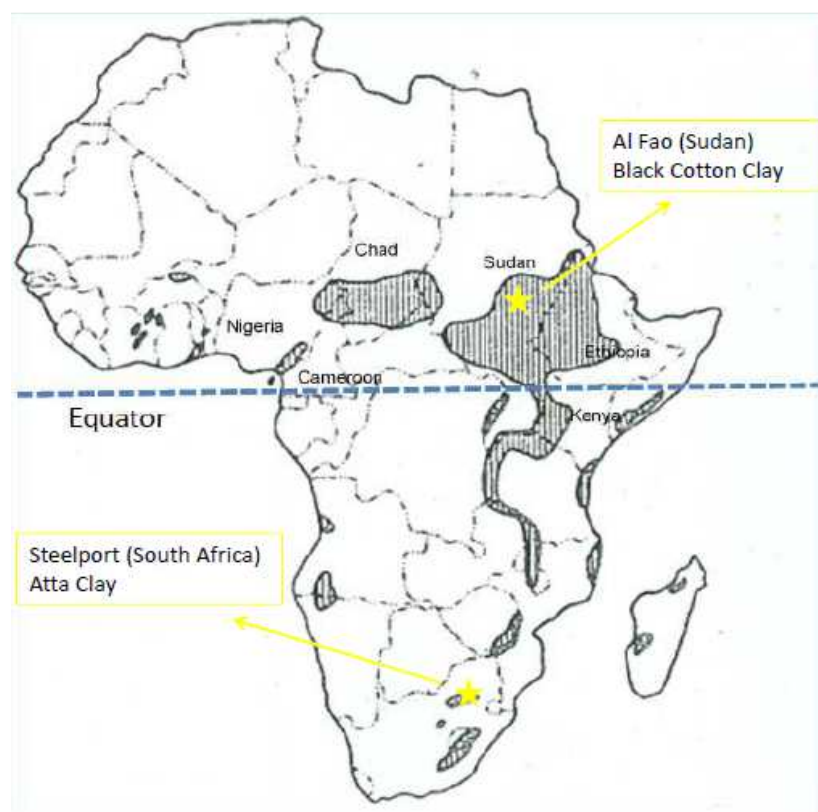


Figure 3. 3 - Distribution of tropical clay soils in Africa with identification of sites of collection of tested clays

Tested materials were collected in two different site location (yellow stars in Figure 3. 3): Atta Clay samples come from Steelpport (South Africa), while Black Cotton Clay samples from Al Fao area (Sudan). As regards the first type (Figure 3. 4(a)), fieldworks were carried out between 15/10/2018 and 22/01/2019 through 2 boreholes, reaching a depth of 17 m. High quality samples with a diameter of 70 mm were collected with intervals of 1.2 m. Fieldwork regarding Black Cotton Clay samples (Figure 3. 4(b)) developed between 01/10/2018 and 02/10/2018 and involved one borehole, from which high quality 100 mm samples of expansive clay were collected up to a depth of 15 m with intervals of 1.5 m, according to the British Standard General Purpose 100 mm Sampler (BS5930:1981).



(a)



(b)

Figure 3. 4 - (a) Atta Clay 70 mm samples from Steelport (South Africa) and (b) Black Cotton Clay 100 mm samples from Al Fao (Sudan)

## 3.4 Characterisation

### 3.4.1 Particle size distribution

Particle size analysis aims to identify the percentage distribution by weight of grains, according to their dimensions. This specific tests consists of two phases: mechanical sieving, which allows to isolate solid fraction bigger than 63  $\mu\text{m}$  (gravel and sand), and sedimentation test for finer particles (silt and clay).

#### 3.4.1.1 Mechanical sieving

The mechanical sieving analysis consists in allowing soil sample to pass through different sieves with an increasing diameter, which are placed on a mechanical shaker. The soil mass retained on each sieve is weighted and the corresponding weight is indicated as  $T_1, T_2, \dots, T_n$ . The percentage of soil passing through the generic sieve  $i$  is obtained according to the following expression:

$$P_i(\%) = \frac{P_t - (T_1 + T_2 + \dots + T_i)}{P_t} * 100 \quad (4.1)$$

The particle size distribution curve is plotted on a graph, where the x-axis represents dimensions of the sieve mesh (equivalent particle diameter) and the y-axis refers to percentages of soil passing through each sieve.

Since tested materials are both clays, it has been decided to perform directly the hydrometer sedimentation test, as described in the following section.

### 3.4.1.2 Hydrometer sedimentation test

The hydrometer sedimentation method is used to obtain the particle size distribution (PSD) of both clay soils, according to British standard (BS 1377:1990: Part 2). It aims to provide the relative percentage of gravel, sand, silt and clay in each sample.

This method is based on Stoke's law, which gives a relationship between the falling velocity of particles and their diameters, starting by the assumption that large particles suspended in a liquid settle more quickly than small ones, with similar densities and shapes.

The velocity  $v_t$  of a spherical particle falling freely in a fluid is given by the following equation:

$$v_t = \frac{D^2 g (\gamma_s - \gamma_l)}{18\eta} \quad (4.2)$$

where

- $v_t$  is the falling velocity;
- $D$  is the particle diameter;
- $\gamma_s$  is the specific weight of solid particle;
- $\gamma_l$  is the specific weight of the fluid (liquid);
- $\eta$  is the dynamic viscosity of the fluid;
- $g$  is the gravity acceleration.

The soil passing the 63  $\mu\text{m}$  sieve is mixed with a dispersant solution made of distilled water and the dispersing agent (sodium hexametaphosphate). Once obtained the soil suspension, it is transferred to a 1000 ml suspension cylinder and then the cylinder is shaken by up-ending about 60 times for 2 minutes. At the end of this procedure the cylinder is placed in an upright position and the time of sedimentation starts. The hydrometer is inserted to float freely and readings taken with time.

In the following Figure 3. 5 test configuration is showed. It involves one cylinder for each tested clay, as indicated by specific labels, one cylinder with distilled water and a thermometer to control room temperature, one cylinder filled with dispersant solution to get initial reading  $R_0$  and the calibrated hydrometer.

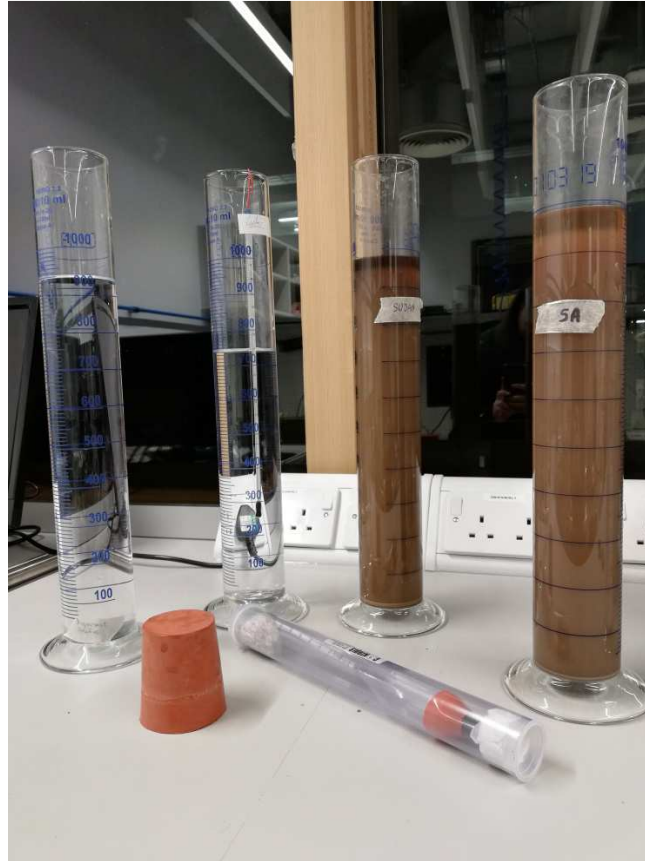


Figure 3. 5 – Hydrometer sedimentation test equipment

Results of hydrometer sedimentation test are expressed in terms of equivalent particle diameter  $D$  and the percentage finer than  $D$  (passing percentage  $K$ ). The equivalent diameter is computed according to the following equation:

$$D = 0.005531 \sqrt{\frac{\eta H_R}{(\rho_s - 1)t}} \text{ [mm]} \quad (4.3)$$

where  $H_R$  is the effective depth in mm corresponding to each value of observed hydrometer reading as obtained by the calibration curve,  $\eta$  is the dynamic viscosity of water in  $mPa \cdot s$  at the test temperature (obtained by interpolation of known values of water viscosity at certain levels of temperature),  $\rho_s$  is the particle density ( $Mg/m^3$ ) and  $t$  is the elapsed time (minutes).

The second variable  $K$  is calculated according to

$$K = \frac{1000\rho_s R_d}{m(\rho_s - 1)} \text{ [%]} \quad (4.4)$$

where  $m$  is the initial sample dry mass [g], which is chosen on the basis of the type of soil, and  $R_d$  is the modified hydrometer reading, consisting of the decimal part only.

The results of the hydrometer sedimentation analysis are expressed by plotting the value of  $K$  corresponding to each value of  $D$  on a semi-logarithmic chart in the form of a continuous curve (Figure 3. 6-Figure 3. 7).

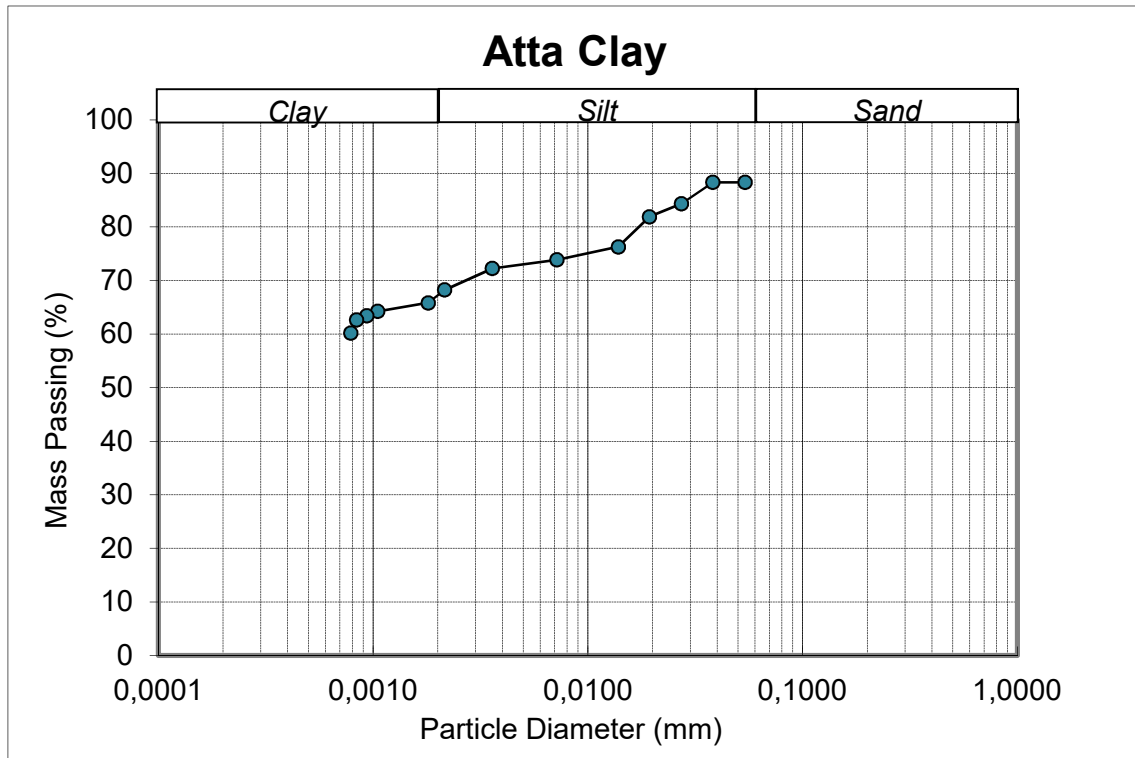


Figure 3. 6 – Particle size distribution curve of Atta Clay (South Africa)

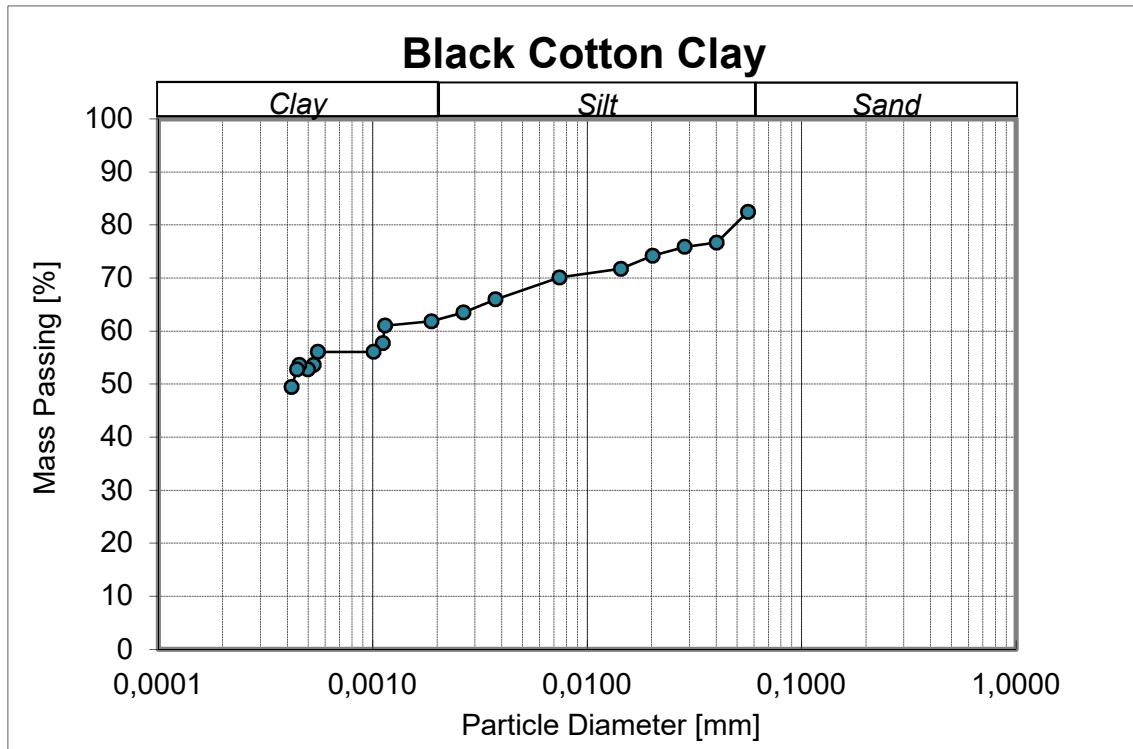


Figure 3. 7 – Particle size distribution curve of Black Cotton Clay (Sudan)

Results show that Atta clay contains a lower sand/gravel content (around 12 %) than Black cotton clay, which is equal to about 17 %, and roughly the same silt content (22 %) with respect to Al Fao clay (21 %). As regards the clay content, Black cotton clay has a slightly lower percentage (62 %) than Atta clay (66 %).

The description names are assigned according to BS5930 (1999):

- Principal soil type: CLAY
- Secondary (< 35%): slightly sandy
- Secondary (terms used to reflect secondary fine constituents where this is important): silty CLAY

It results that Black Cotton and Atta clay are both slightly sandy silty clay.

### 3.4.2 Atterberg limits

The soil condition can be changed by varying the moisture content. If the moisture content is gradually reduced starting from slurry condition, the soil changes through four states: liquid, plastic, semi-plastic and solid state. Moisture contents at each state boundary are known as the Atterberg limits: Liquid limit (LL), Plastic limit (PL) and Shrinkage limit (SL).

As regards liquid limit, it can be determined according to two main methods:

- Casagrande's method
- Cone penetrometer method

In the present work it is determined using the second method according to BS 1377:1990.

Once dried at room temperature, the sample is crushed and sieved on a 425  $\mu\text{m}$  sieve. Then, the soil is placed on a tray, distilled water is added and mixed thoroughly until an homogeneous paste is formed. To allow a uniform hydration process, the mix is sealed and left for 24 hours. A portion of obtained mix is used for the plasticity tests, while the remaining part is again mixed with a little amount of water, in order to ensure that the first cone penetration reaches the minimum value of 15 mm, according to BS 1377:1990. At least four points are required to estimate the liquid limit, which means that tests at four different water contents are performed by gradually adding water to the mixture. Each test corresponds to a point on the water content-cone penetration plane and obtained experimental results are fitted by a straight line. The liquid limit (LL) of tested material is defined as the water content corresponding to a cone penetration equal to 20 mm.

In Figure 3. 8 test configuration is showed and it includes dynamic cone penetrometer and a cup filled with tested clay at different water contents.



Figure 3. 8 - Cone penetrometer test equipment

Figure 3. 9 and Figure 3. 10 represent results of cone penetrometer tests performed on both Atta Clay (South Africa) and Black Cotton clay (Sudan), in terms of single measurements, then fitted by straight lines, whose equations are showed on the same graph.

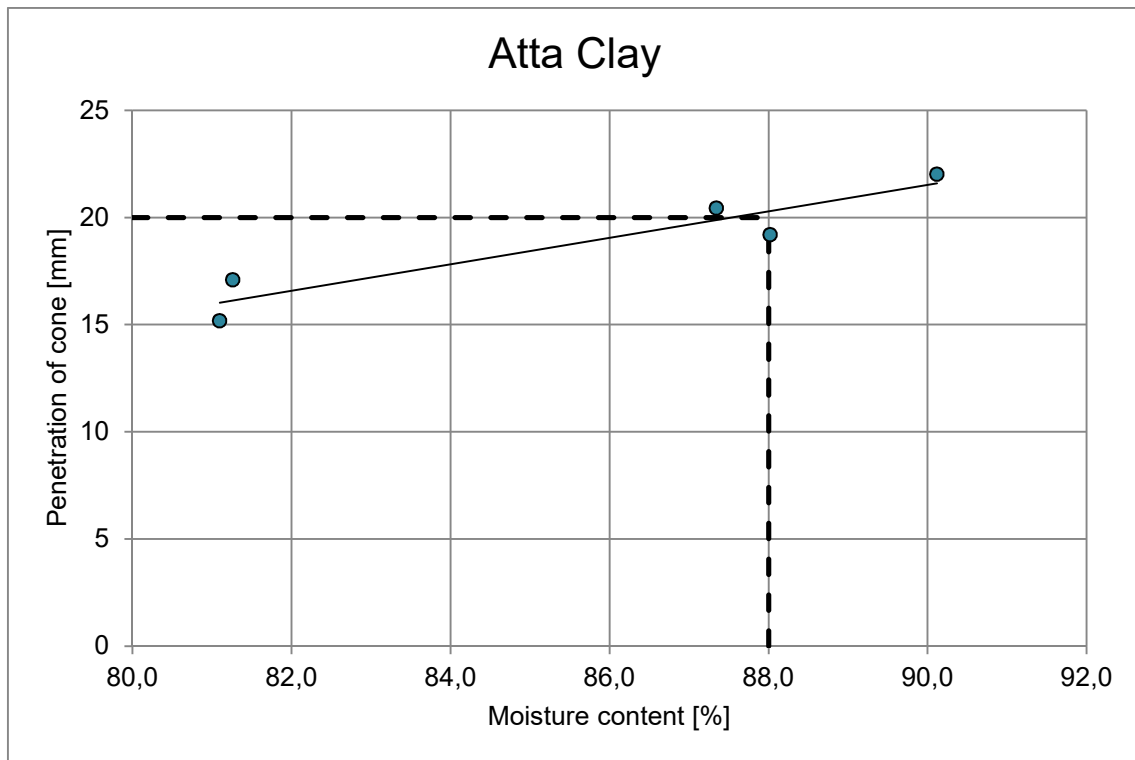


Figure 3. 9 – Cone penetrometer test results and liquid limit of Atta Clay (South Africa)

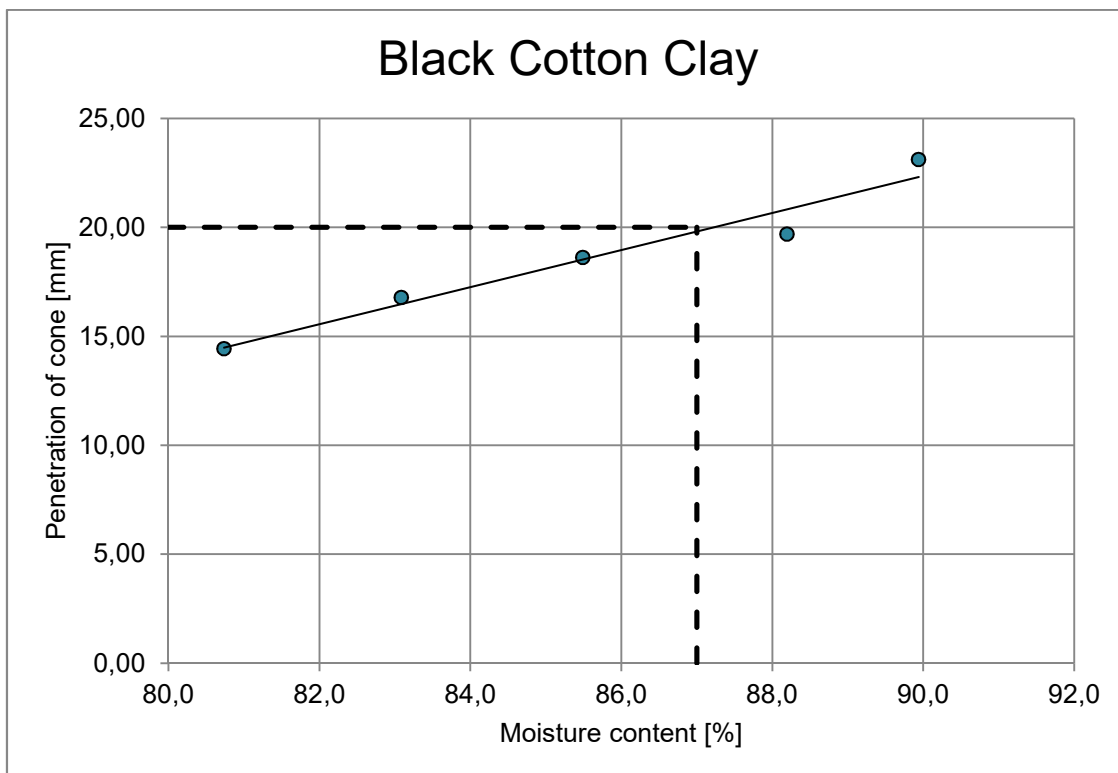


Figure 3. 10 - Cone penetrometer test results and liquid limit of Black Cotton clay (Sudan)

According to the described procedure, liquid limits for tested materials are defined as the moisture contents corresponding to a cone penetration equal to 20 mm and results are listed in Table 3. 1:

Table 3. 1 - Liquid limit of tested clays

Material	Liquid limit (%)
Atta Clay (South Africa)_ Depth: 1.0-1.2 m	88
Black cotton clay (Sudan)_ Depth: 1.0-1.5 m	87

The rest of prepared mix was used to determine the plastic limit according to BS 1377:1990. The soil was rolled to form a ball which is divided into four parts and each of them was pressured and kneaded by fingers until the thread started to crumble. The first crumbling point is the plastic limit and the final value is assumed equal to the average of the four water content measurements.

The difference between the liquid limit and plastic limit gives the plasticity index ( $I_p$ ) of the soil.

According to Casagrande plasticity chart, Atta Clay and Black Cotton Clay have a liquid limit of 88% and 87% respectively, so they are both classified as sandy fat clay (CH). As shown in Figure 3. 11, both the plasticity data lie above the A-line, so the two soils can be considered to exhibit clay behaviour.

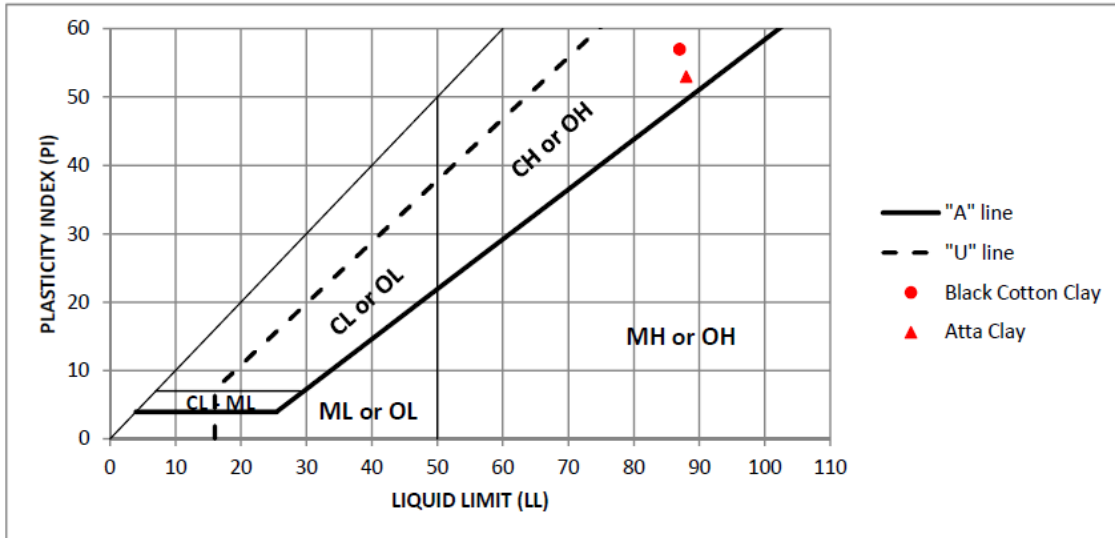


Figure 3. 11 – Classification of tested clays according to Casagrande plasticity chart

In Table 3. 2 results of characterisation are summarized for both tested materials.

Table 3. 2 – Summary of classification test results

Soil type	Black cotton clay	Atta clay
Gravel (%)	/	/
Sand (%)	17	12
Silt (%)	21	22
Clay (%)	62	66
Liquid limit, LL (%)	87	88
Plastic limit, PL (%)	30	35
Plasticity index, PI (%)	57	53
Activity (PI/clay content)	0.92	0.80
BS classification	slightly sandy silty clay	slightly sandy silty clay
ASTM classification	Sandy fat clay (CH)	Sandy fat clay (CH)

### 3.5 Experimental program

As initially introduced, the experimental program mainly involves soil suction measurements through dewpoint potentiometer (WP4C), in order to get Soil-Water retention curves of both clays, and the dynamic

characterisation at small and medium strains of tested materials by using a controlled-suction resonant column torsional shear cell (RCTS).

As regards suction measurements, both soils are reconstituted from slurry in a consolidometer to a vertical total stress of 200 kPa. Four discs for each soil were trimmed from the resulting soil cakes and initial water content and volume measured.

Initial discs conditions are listed in Table 3. 3 and Table 3. 4 for both Atta Clay and Black Cotton Clay samples respectively.

Table 3. 3 - Initial conditions of Atta clay samples for suction measurements

SAMPLE	Initial water content [%]	Initial volume [cm <sup>3</sup> ]
1	63,30	7,34
2	63,30	6,34
3	63,30	7,52
4	63,30	7,33

Table 3. 4 - Initial conditions of Black Cotton clay samples for suction measurements

SAMPLE	Initial water content [%]	Initial volume [cm <sup>3</sup> ]
1	79,06	7,37
2	79,06	6,63
3	79,06	6,06
4	79,06	6,93

Discs are allowed to gradually dry in a controlled-temperature laboratory and total suction and volume changes are daily measured, in order to obtain the Soil-Water Retention Curves (SWRC) for each tested clay.

By referring to RCTS tests, initially the experimental program involved a saturated test (closed air circuits) and two suction-controlled test at two different values of suction equal to 100 kPa and 300 kPa, in order to investigate suction effects on the small and medium strains behaviour of expansive clays.

Results obtained by a previous study (Abdalla *et al.*, 2019) related to the same tested materials (WindAfrica project) included Soil-Water retention curves of Black Cotton Clay. As illustrated in Figure 3. 12, tested material tends to remain saturated ( $S_r \approx 90 \div 100\%$ ) up to high suction values, about 2 MPa, as a consequence of its high plasticity (PI=57).

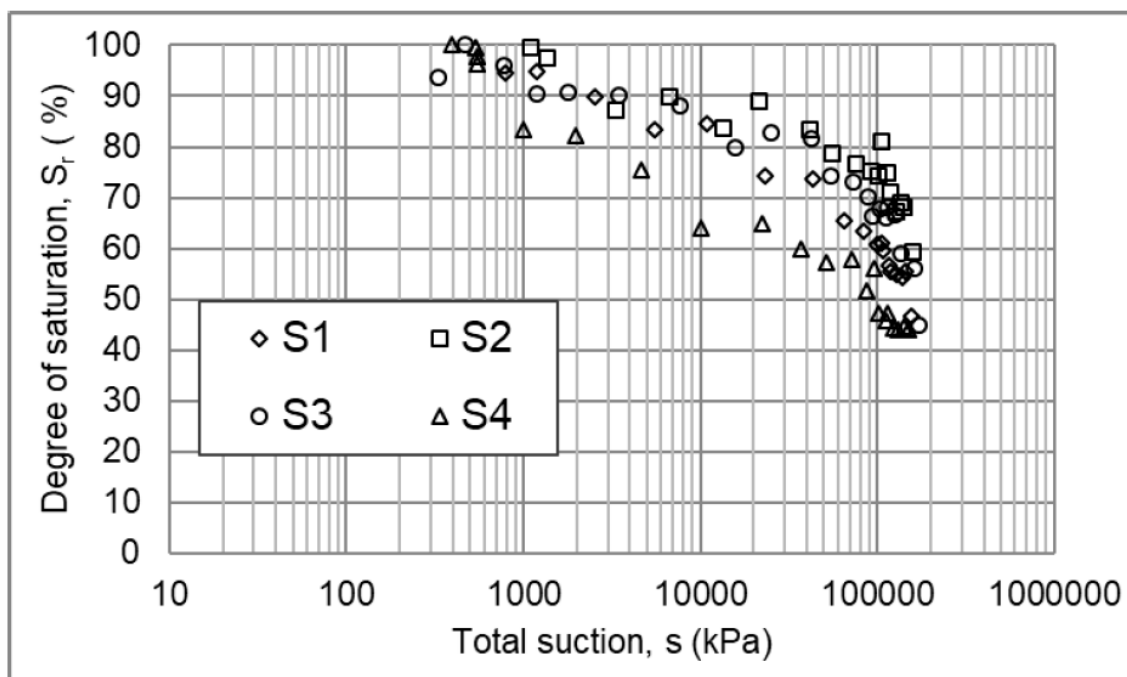


Figure 3. 12- Black Cotton clay SWRC resulting from a previous study (after Abdalla *et al.*, 2019)

It follows an incompatibility between tested material and specific characteristics of RCTS apparatus, in terms of suction-controlling during partly saturated tests. Indeed, this specific expansive clays reach an unsaturated condition at suction levels (2 MPa) higher than the maximum value that can be controlled by the present RCTS apparatus, equal to the air-entry value of the chosen porous disc (0,5 MPa).

As a consequence, the initially developed experimental program has been modified by including only a saturated test. It means that the hydraulic behaviour of tested materials is investigated under unsaturated conditions, while the dynamic one under saturated conditions.

## 4. Testing apparatus and methodology

### 4.1 Introduction

The following chapter presents testing apparatus and methodology by distinguishing between the two experimental procedures, soil suction measurements and RCTS tests. As regards the first, specifications and limits of WP4C device are illustrated, in order to clarify reasons of obtained results. Then, RCTS apparatus is described in terms of an overall theoretical background, which includes models for test interpretation and technique of control of suction, and a detailed description of each part of the apparatus, set up at the NRFIS laboratory (University of Cambridge). Finally, Chapter 4 illustrates preliminary testing procedures, regarding the saturation of all water circuits and the porous stone, and samples preparation.

### 4.2 Soil suction and volume change measurement (WP4C)

A dewpoint potentiometer (WP4C) is used to measure samples suction. As described in chapter 2.3, soil suction can be derived by measuring water vapour partial pressure in equilibrium with pore water  $u_v$ , referred to water vapour partial pressure in equilibrium with free water  $u_{v0}$  (Richards 1965). As a consequence, the sample is placed in the sealed chamber and the relative humidity of the air above the sample is measured through the chilled mirror technique, once reached the equilibrium between the sample and the vapour. At the dew point, the WP4C measures both mirror and sample temperature within 0.001 °C. The device can measure suction ranging between -0.1 MPa to -300 MPa with an accuracy of  $\pm 0.05$  MPa from 0 to -5 MPa and 1% from -5 to -300 MPa.

Tested discs are incrementally dried in stages and, each time, suction, diameter and height are measured by using a caliper; volume changes are computed through the average values of diameter and height. The drying process allows to develop the PDC of SWRC for tested soils, but due to the upper limit of suction that that could be measured by means of the WP4C device (-300 MPa), the final residual state cannot be reached.

In the following Figure 4. 1 is showed the overall set of instruments (scale, caliper and WP4C device) used during one of daily steps of measurements.

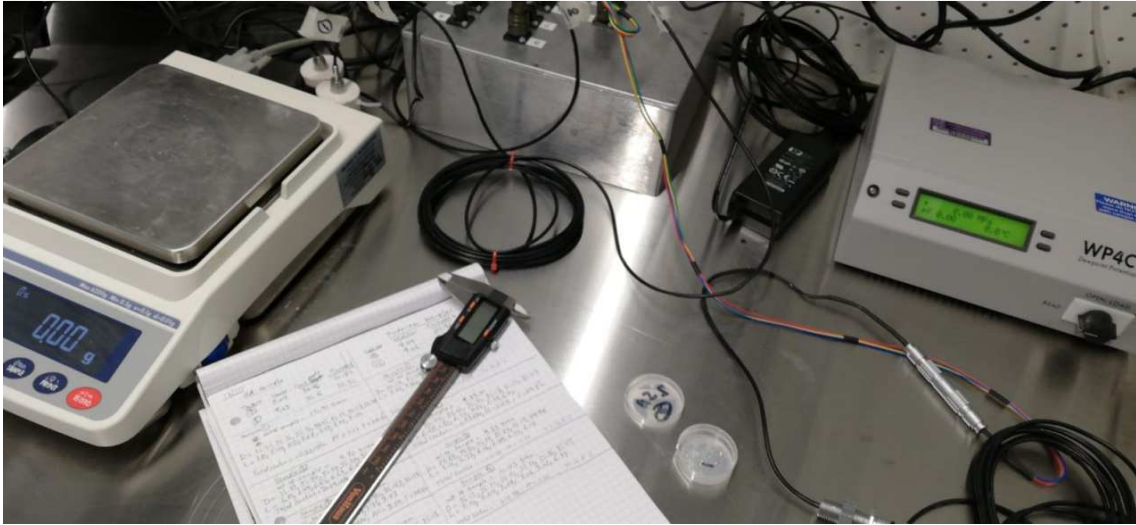


Figure 4. 1 – Equipment for sample suction and volume measurements

### 4.3 Suction-controlled RCTS (Resonant Column Torsional Shear) apparatus

#### 4.3.1 RCTS background

On the basis of the analysed strain levels, dynamic and cyclic laboratory tests are distinguished into two main groups: low and medium strain level tests (as the resonant column RC test) and high strain level tests (as torsional shear TS test). One of the main difference between the two groups is the way of application of loads, since the first group involves applied loads with frequencies between 1 and 100 Hz and not negligible inertial forces, while the second one is characterised by lower frequencies between 0.01 Hz and 1 Hz and negligible inertial forces.

The dynamic shear modulus is the principal soil property for evaluating shear wave propagation in soils and the dynamic response of foundations. Several laboratory and field tests can be used to measure shear wave velocity, which is proportional to the shear modulus. The resonant column (RC) test is a widely used non-destructive test that gives very accurate results for strain amplitude as low as 0.001%.

In terms of soil dynamics and geotechnical earthquake engineering, the response of the geotechnical material to shearing motions can be expressed by means of the shear modulus  $G$  according to the following equation:

$$G = \rho \cdot V_s^2$$

where  $\rho$  is the soil volume density and  $V_s$  is the S-wave propagation velocity.

The shear modulus at very small strains is called primary ( $G_0$  or  $G_{\max}$ ) and the RC test is considered the most consistent estimation method of this initial strength value.

The main objective of this technique is to analyse the response of materials subjected to harmonic vibrations representing seismic loads. According to the most common configuration, the sample is placed in a triaxial stress chamber, the base of the soil specimen is fixed against rotation and the free end is excited in torsion (fixed-free configuration). Applied stress is generated by an electromagnetic motor operating up to a range of frequencies in which inertial forces are not as negligible as in static conditions. Measurement of the resonant frequency and vibration amplitude of the sample using elastic wave propagation theory allows for estimation of wave velocity and damping in the sample.

The test procedure includes a certain number of measurements of shear modulus against the increasing levels of shear strains, in order to define the diagram ( $\gamma$ -G). For each level of strain the damping ratio is also calculated, in order to define the diagram ( $\gamma$ -D).

Resonant column apparatus was initially developed to study metal and rock behaviour and only later soil behaviour.

For this reason two main different versions of RC can be distinguished:

- *Hardin apparatus* (Figure 4. 2(a)), which allows to apply an harmonic torsional moment together with an harmonic vertical load, so that both S-wave and P-wave velocities can be determined (and thus Poisson coefficient and longitudinal modulus respectively), and anisotropic consolidation of the tested sample can be obtained (Drnevich *et al.* , 1978);
- *Stokoe apparatus* (Figure 4. 2(b)), which allows only to apply a torsional moment and to get an isotropic consolidation (Allen, J. C., and K. H. Stokoe, 1982).

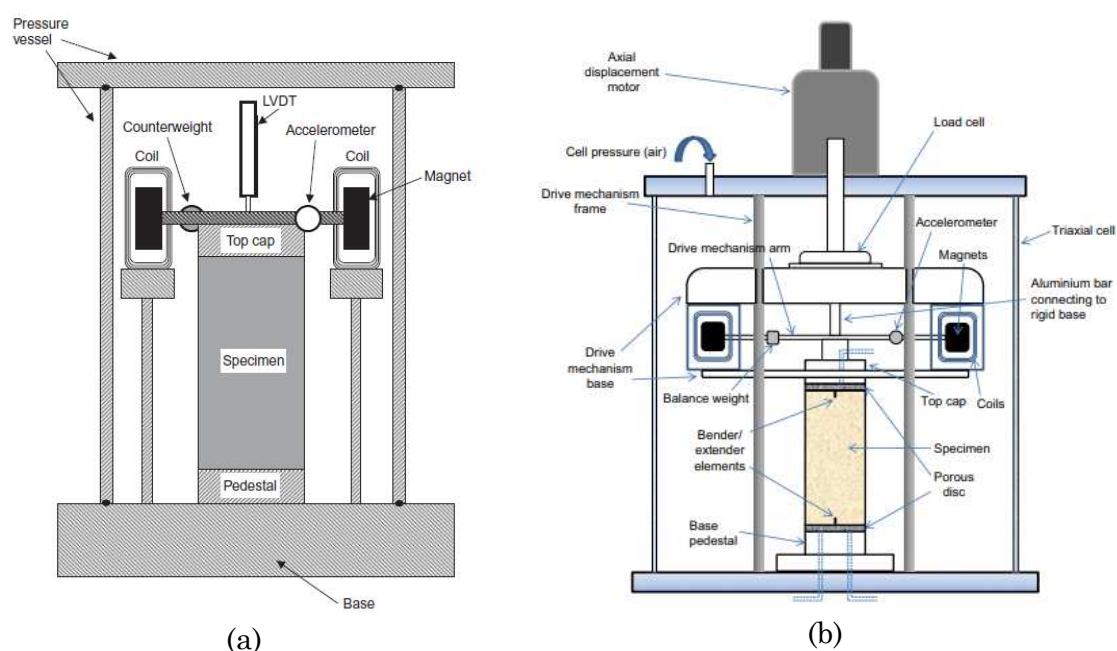


Figure 4. 2 - (a) Stokoe-type (after Clayton, C. R. I., *et al.* , 2009) and (b) Hardin-type (after Li, H. *et al.* , 2018) resonant column apparatus

Test results are resonance frequency and rotation of the sample free head (Richard *et al.*, 1970). The first allows to compute shear-wave propagation velocity and the correspondent shear modulus  $G$ , while tangential strains can be obtained by measuring sample head rotations. Since RC test involves typical frequencies of a cylindrical sample, test frequencies are relatively high (10-100 Hz).

### 4.3.2 RCTS test interpretation: physical model

The sample subjected to harmonic torsional waves may be described by physical models, such as a twisted rod with one degree of freedom, whose behaviour can be analysed by solving equations of propagation of elastic waves.

During RC test a sinusoidal electrical signal, which can be varied in amplitude and frequency, is generated through a function generator and a power amplifier. The electrical signal  $V(t)$  is turned in a torsional mechanical stress  $M_t(t)$ , by means of an electromagnetic motor made of 8 coils, which interact with 4 permanent magnets, placed on the sample head, through a drive plate. Frequency varies until the system reaches the condition of resonance, which is defined as the frequency value that corresponds to a phase angle between torsional excitation and system rotation equal to  $\frac{\pi}{2}$  and to a maximum response amplitude.

Test configuration can be compared to the propagation of a torsional wave through a bar, since the wave induced from the top base (free) is reflected by the bottom one (fixed); direct and reflected waves generate a destructive interference, if they have opposite phases, or a constructive interference if they have the same phase, so that the resonance phenomenon results.

In the same way, by considering a beam with one fixed end, a negligible mass, a given axial stiffness  $k$  and a concentrated force  $F$  applied to the free end, the beam itself absorbs elastic energy and shows a static deformation. Otherwise, by adding a mass  $m$  to the free end, an inertial component appears in the equation of motion and, as a consequence, an exchange between elastic and inertial energies occurs.

The obtained system behaves as a Single Degree of Freedom (SDOF) system (Figure 4. 3).

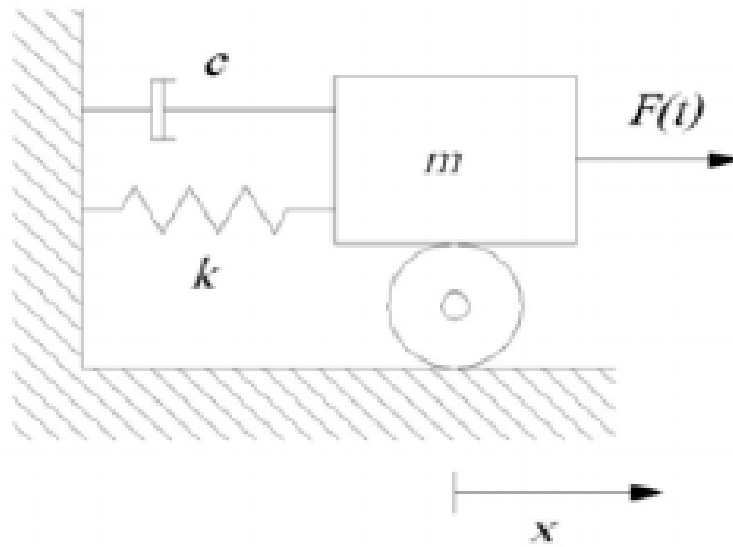


Figure 4. 3 - SDOF system configuration

The resonance condition corresponds to the maximum strain (maximum response amplitude), which is equal to the condition of the minimum kinetic energy and maximum elastic deformation energy.

The resonance frequency is described by the following equation:

$$f_R = \frac{1}{2\pi} \sqrt{\frac{K}{m}} \quad (5.1)$$

The shape of the curve of the response amplitude  $A$  as a function of frequency  $f$  is characterised by the dissipation and it is described by means of the frequencies range  $[f_1, f_2]$ , which defines the frequency bandwidth corresponding to a response amplitude equal to  $\frac{A_{max}}{\sqrt{2}}$ , according to the half power bandwidth method (Figure 4. 4). Higher is the bandwidth and the distance of each frequency from the peak, higher is the damping of the system.

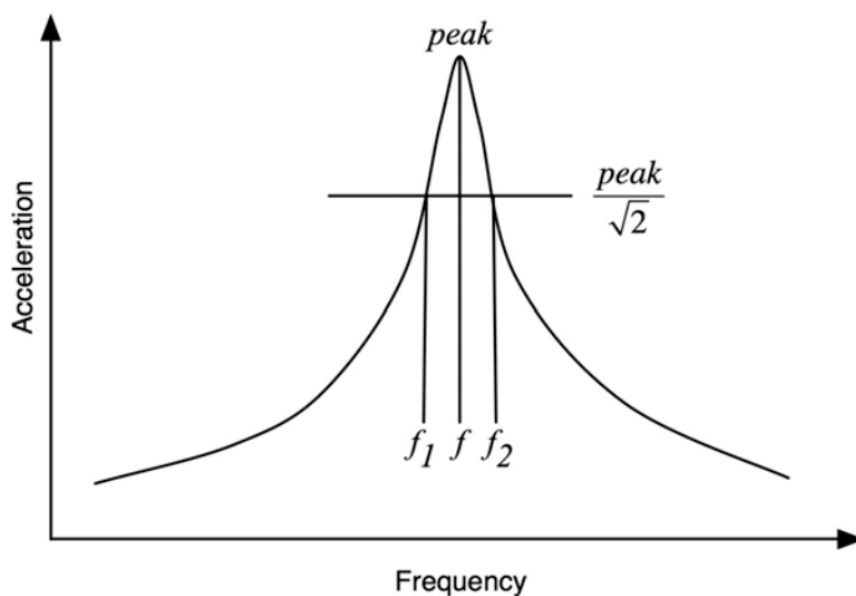


Figure 4. 4 – Evaluation of soil damping ratio according to the half power bandwidth method

Soil behaviour can be described through the described physical model by substituting the beam with a spring with a given inertia. By considering a soil sample (Figure 4. 5) with a height  $h$  and a given torque applied to the top base  $M_o(t)$ , each “layer” of the sample is characterised by an angular rotation  $\theta$ , which decreases towards the centre. According to the fixed-free configuration, tangential strain  $\gamma$  varies from the maximum value at the loaded end to zero at the fixed end.

As regards the equation of motion, the main difference with respect to a SDOF system is the presence of two inertial components (soil mass and external rigid mass), described in terms of:

- $I_p$ , sample polar inertia;
- $I_t$ , drive system polar inertia.

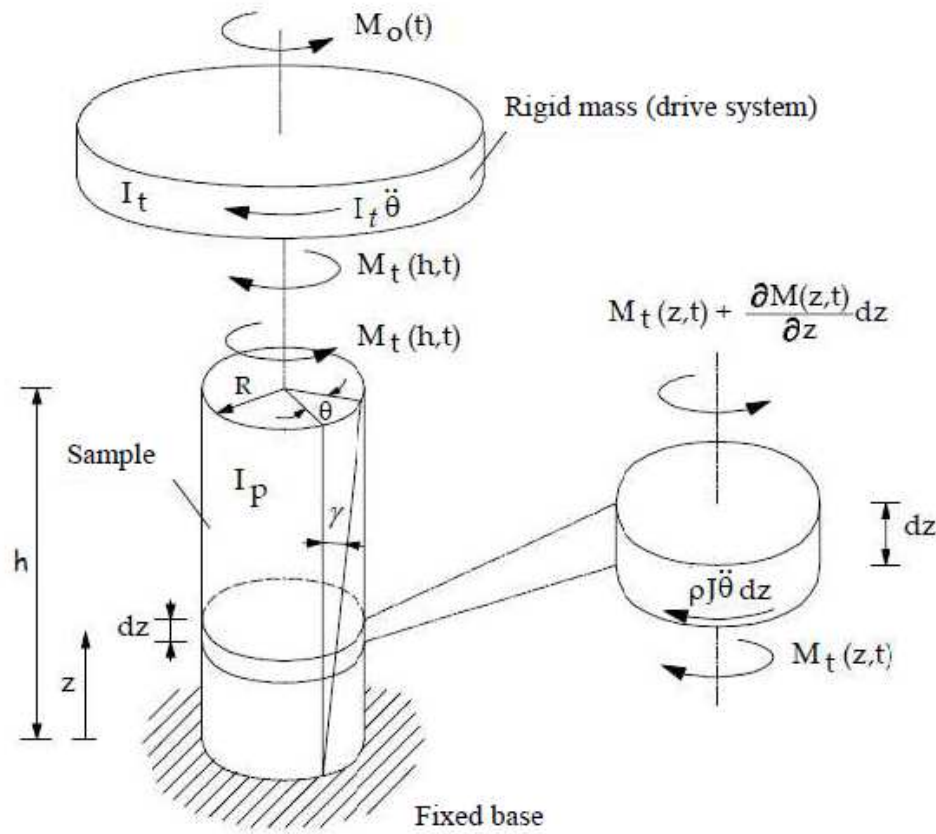


Figure 4.5 - Reference dynamic model for RCTS test interpretation (fixed-free configuration)

By considering a resonant column specimen of height  $h$  in a fixed-free test configuration, with polar moment of inertia  $J_p$ , subjected to harmonic torsional loading, under dynamic equilibrium condition of the rigid mass, the torque applied on the top of the specimen due to its elastic resistance

$$M_t(h, t) = GJ_p \frac{\partial \theta}{\partial z} = G \frac{I_p}{\rho} \frac{\partial \theta}{\partial z} \quad (5.2)$$

must be equal to the inertial torque of the loading system (Kramer, 1996)

$$M_t(z, t) = -I_t h \frac{\partial^2 \theta}{\partial t^2} \quad (5.3)$$

where  $I_p$  is the sample polar inertia and  $I_t$  is the drive system polar inertia.

Assuming that rotations of the specimen  $\theta(z, t)$  are also harmonic, they can be described by

$$\theta(z, t) = (C_3 \cos kz + C_4 \sin kz)(C_1 \cos \omega t + C_2 \sin \omega t) \quad (5.4)$$

The values of each constant can be derived by applying the following boundary conditions:

- $\theta(z = 0, t) = 0$  (fixed base)  $\rightarrow C_3 = 0$
- $G \frac{I_p}{\rho} \frac{\partial \theta}{\partial z} = -I_t h \frac{\partial^2 \theta}{\partial t^2}$  (dynamic equilibrium at the top under applied torque)

so that

$$\begin{aligned} G \frac{I_p}{\rho} C_4 k_n \cos k_n h (C_1 \cos \omega t + C_2 \sin \omega t) \\ = -I_t h (-\omega_n^2 C_4 \sin k_n h) (C_1 \cos \omega_n t + C_2 \sin \omega_n t) \end{aligned} \quad (5.5)$$

which can be expressed as

$$\frac{I_p}{I_t} = \left( \frac{\omega_n \cdot h}{V_s} \right) \cdot \tan \left( \frac{\omega_n \cdot h}{V_s} \right) = \beta \cdot \tan \beta \quad (5.6)$$

where  $f_R$  is the resonant frequency,  $h$  is the sample height,  $I_p$  is the sample polar inertia and  $I_t$  is the drive system polar inertia.

For a given value of the ratio  $\frac{I_p}{I_t}$ , the equation (5.6) has infinite solutions  $\beta$ , corresponding to the infinite mode shapes of the mechanic system. RC tests are usually performed at the minimum value of the resonance frequency (first mode shape), at which the amplitude response of the system is maximum.

By using an iterative method, the solution  $\beta$  of the implicit equation (5.6) is obtained and the corresponding shear-wave propagation velocity results equal to:

$$V_s = \frac{2\pi f_R L}{\beta} \quad (5.7)$$

Shear modulus  $G$  is then computed as a function of sample density and shear-wave propagation velocity, by means of the well-known relationship:

$$G = \rho V_s^2 \quad (5.8)$$

Soils non-linear behaviour leads to two different phenomena linked to strain level increasing:

- softening spring, which is a reduction of the soil stiffness;
- increasing of dissipation.

The decrease of stiffness as strain level increases corresponds to a reduction of the shear-waves propagation velocity or, equally, a reduction of the resonant frequency, which graphically means a translation of the resonance frequency peak towards lower frequencies. At the same time, an increase of dissipation determines a reduction of the amplitude response, so the overall result of soils non-linear behaviour is that the resonance peak translates towards left and it decreases. The amplitude-frequency curve is also characterised by an a-symmetric shape, due to a reduction of soil stiffness as strain level increases (Figure 4. 6).

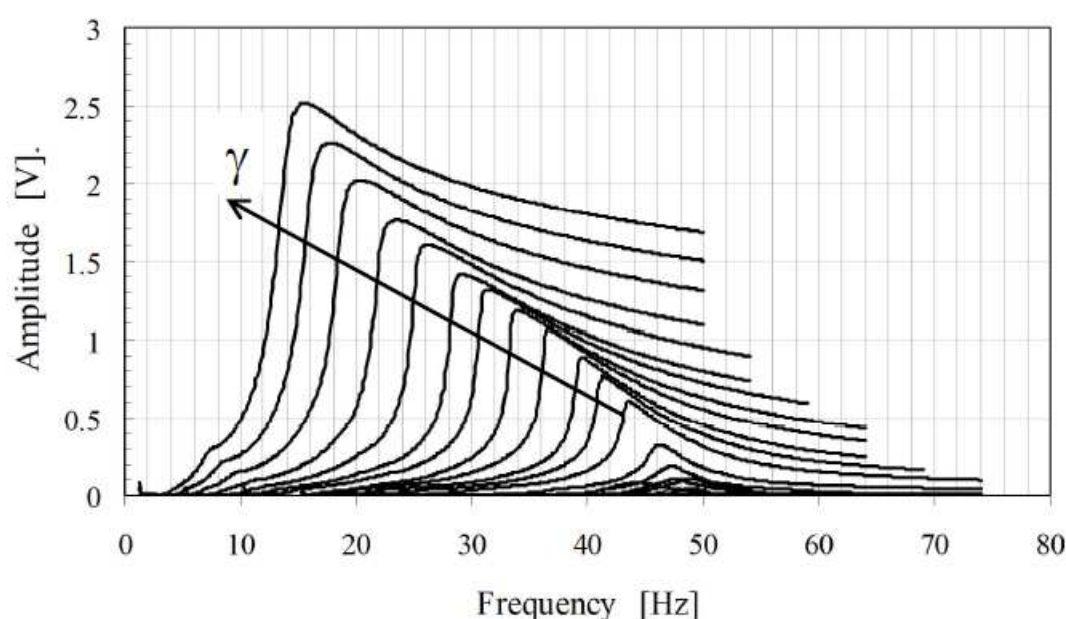


Figure 4. 6 – Amplitude-frequency curves for increasing strain levels

A static test ( $f=0$ ) allows to apply a static angular deformation, which corresponds to  $G_{max}$ , while a dynamic test (frequency sweep) leads to the determination of the whole amplitude-frequency curve and, as a consequence, the resonance peak. The frequency related to the maximum amplitude response (resonance frequency) allows to determine the shear modulus  $G$  corresponding to a strain level equal to

$$\gamma = \frac{2}{3} \cdot \frac{R}{h} \cdot RCF \cdot A_{acc} \quad (5.9)$$

where  $R$  and  $h$  are respectively the sample radius and height,  $RCF$  is a calibration factor proportional to the inverse of the square of frequency and  $A_{acc}$  is the

acceleration amplitude. The constant  $2/3$  derives from the observation that shear strain due to torque is not constant along a cross section, but it varies from the centre towards boundaries of the cylindrical sample. As a consequence, it is necessary to assume a reference value  $\gamma_{rif}$ , which is conventionally equal to the strain value measured at a distance of  $\frac{2}{3}R$  from the centre (Hardin and Drnevich 1972a).

RC test allows also to determine the damping ratio  $D$  through two main methods: half power bandwidth method or logarithmic amplitude decay method.

### 4.3.2.1 Half power bandwidth method

According to the half power bandwidth method, frequency is gradually increased to find the response amplitude-frequency curve, which allows to determine the maximum shear modulus and the range of frequencies  $[f_1, f_2]$  required to get the damping coefficient.

The amplification factor  $M_f$  is equal to the ratio between dynamic and static response and it is defined according to the following equation:

$$M_f = \frac{\vartheta}{\vartheta_s} = \frac{1}{\left[ \left(1 - \frac{\Omega^2}{\omega^2}\right)^2 + \left(\frac{2\zeta\Omega}{\omega}\right)^2 \right]^{1/2}} \quad (5.10)$$

where  $\vartheta_s$  is the static rotation,  $\vartheta$  is the dynamic one,  $\Omega$  is the forcer pulsation,  $\omega$  is the system pulsation and  $\zeta$  is the decay factor of the system. In Figure 4. 7 amplification factor is plotted against  $\frac{\Omega}{\omega}$  for different values of decay factor  $\zeta$ .

The equation (5.10) allows for the following considerations:

- if  $\frac{\Omega}{\omega} \ll 1$ , the forcer frequency is strongly lower than system natural frequency and the dynamic amplification factor  $M_f$  results equal to 1 for any values of the decay factor  $\zeta$ . It means that the system response is quasi-static;
- if  $\frac{\Omega}{\omega} \gg 1$ , the forcer frequency is definitively higher than the natural one and, as a consequence, the amplification factor tends to zero, which means that the system does not show big deformations under the applied forcer;
- if  $\frac{\Omega}{\omega} = 1$ , the system is in the resonance condition and the factor  $M_f$  results equal to:

$$M_f = \frac{1}{2\zeta} \quad (5.11)$$

Equation (5.11) shows that an increase in the decay factor leads to a reduction of the amplification factor and, as a consequence, of the dynamic response  $\vartheta$ .

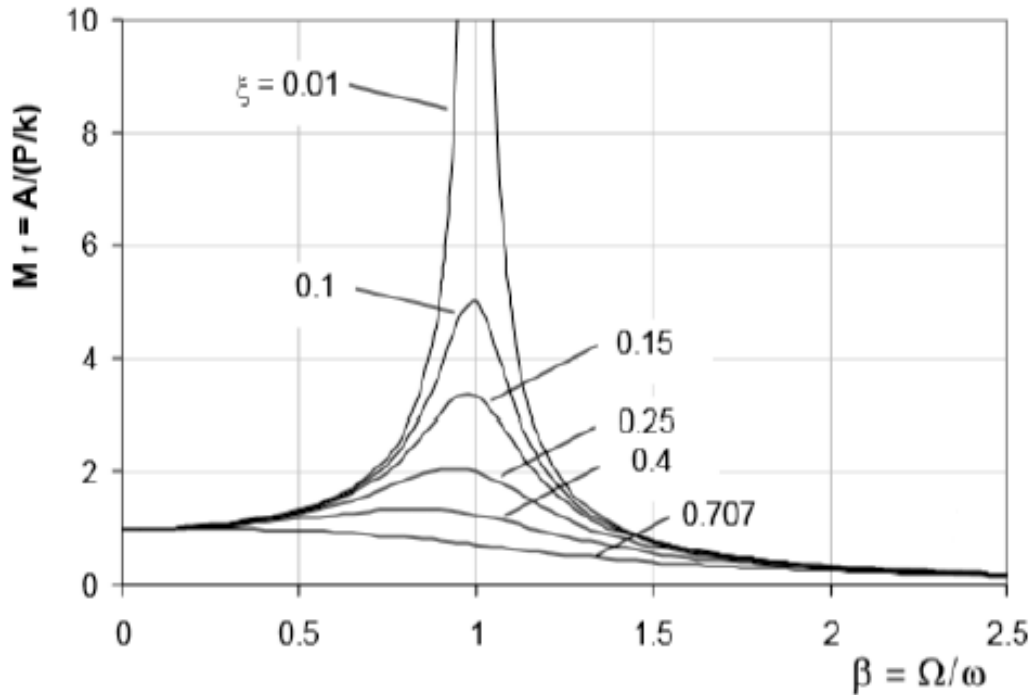


Figure 4. 7 – Amplification factor changes in a SDOF viscous-elastic system under forced oscillations (after Chopra, 2002)

By computing the first derivative of the amplification factor with respect to the ratio  $\frac{\Omega}{\omega}$ , it results equal to zero for a value of forcer frequency correspondent to the resonance condition:

$$\Omega = \omega \cdot \sqrt{1 - 2\zeta^2} \quad (5.12)$$

It follows that the maximum value of the amplification factor results

$$M_{f,max} = \frac{1}{2\zeta \cdot \sqrt{1 - 2\zeta^2}} \quad (5.13)$$

By imposing  $M_f$  equal to  $M_{f,max}/\sqrt{2}$ , it follows

$$\frac{1}{\left[ \left(1 - \frac{\Omega^2}{\omega^2}\right)^2 + \left(\frac{2\zeta\Omega}{\omega}\right)^2 \right]^{1/2}} = \frac{1}{\sqrt{2}} \frac{1}{2\zeta} \quad (5.14)$$

If  $\frac{\Omega}{\omega} = \beta$  it is possible to get the two solutions:

$$\beta_{1,2} \approx 1 - \zeta^2 \mp \zeta \cdot \sqrt{1 - \zeta^2} \quad (5.15)$$

from which

$$\beta_2 - \beta_1 \approx 2\zeta\sqrt{1 - \zeta^2} \approx 2\zeta \quad (5.16)$$

According to the half power bandwidth method (Figure 4. 8), the decay factor can be approximated as

$$\zeta \approx \frac{\beta_2 - \beta_1}{2} = \frac{\Omega_2 - \Omega_1}{2\omega} \quad (5.17)$$

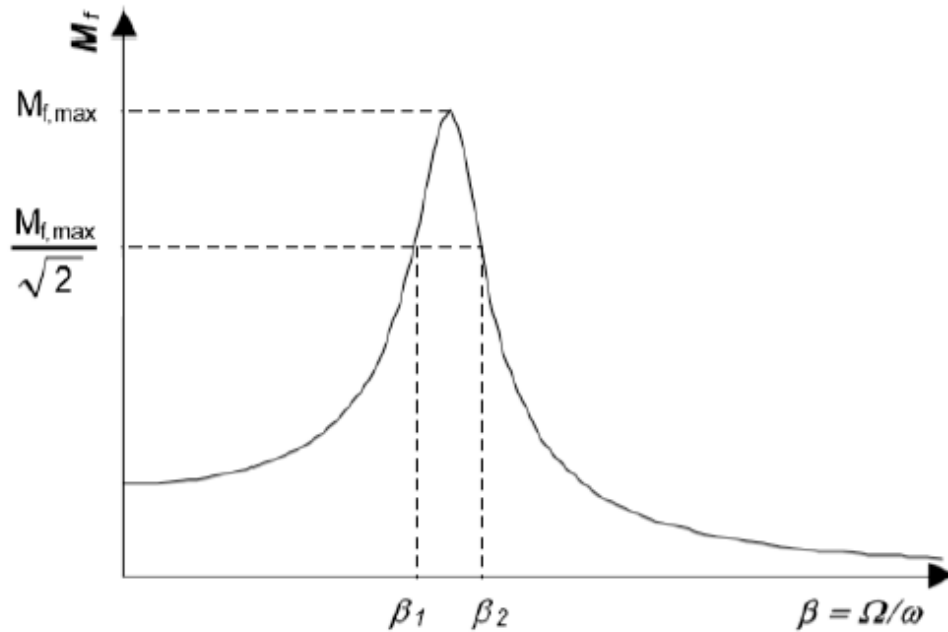


Figure 4. 8 – Dynamic amplification curve and computation of damping ratio (after Chopra, 2002)

The main limit of the half power bandwidth method is the assumption of linear elastic behaviour of the material, which is valid for soils only below the linear elastic strain threshold. By increasing the applied excitation (torque on the free base), strain levels overcome the linear threshold and, as a consequence, resonance frequency progressively decreases. As shown in Figure 4. 6, the shape of the response amplitude-strains curve results no more symmetric, which leads to an overestimation of the decay factor computed by means of the half power bandwidth method. Since an overestimation of decay factor at high strain levels does not result in safety condition, an alternative method is the logarithmic amplitude decay method.

### 4.3.2.2 Logarithmic amplitude decay method

As regards the free-decay test, it is usually performed after RC test, since samples are loaded with the same amplitude of RC test and a constant frequency, equal to the resonance one. Once reached stationary conditions, external loads are removed and the accelerometer measures the typical response of the free-decay oscillation, which allows to determine damping ratio by applying the logarithmic amplitude decay method.

This method is based on the evolution of sample head oscillations starting from the interruption of the forcer applied on the system.

By considering the harmonic-type solution related to the evolution of damped oscillations, the following equation derives:

$$x(t) = e^{-\zeta\omega t} \cdot \left( \frac{\zeta\omega x_0}{\omega_D} \sin\omega_D t + x_0 \cos\omega_D t \right) \quad (5.18)$$

The time evolution of the oscillation amplitude is defined by the negative exponent of the equation (5.18), which means that higher is the decay factor  $\zeta$ , quicker is the oscillation damping.

In the following Figure 4. 9, the free decay evolution is showed.

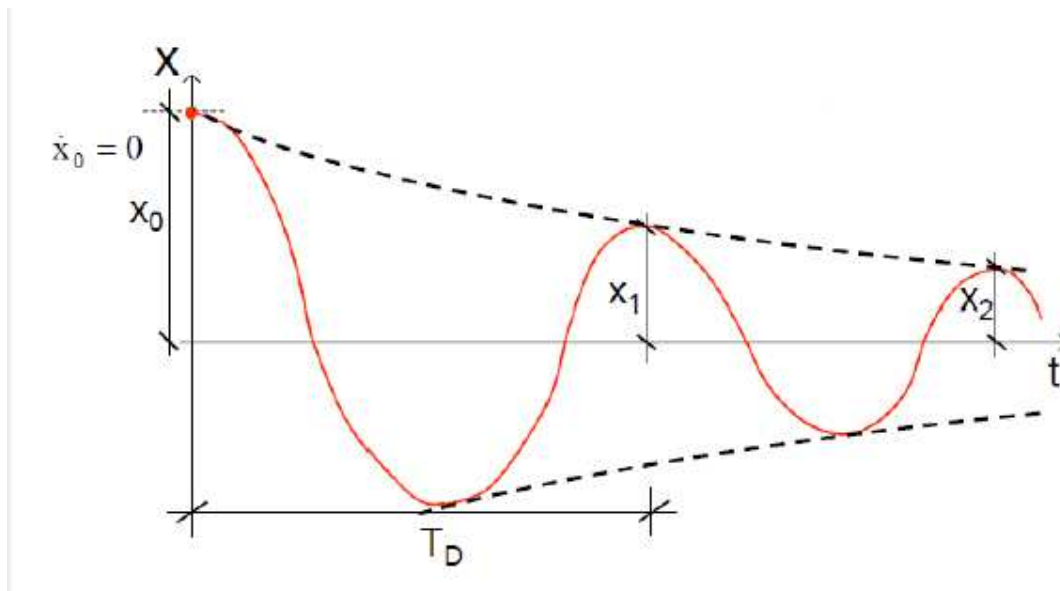


Figure 4. 9 – Free-decay trend on the sample head (after Foti, 2019)

The damped pulsation  $\omega_D$  and period  $T_D$  are defined respectively as

$$\omega_D = \omega \cdot \sqrt{1 - \zeta^2} \quad (5.19)$$

$$T_D = \frac{2\pi}{\omega_D} \quad (5.20)$$

It can be noted that since the decay factor is always strongly lower than 1, the damped pulsation and, as a consequence, the damped period result equal to the natural pulsation and period respectively.

It follows that the ratio between two consecutive amplitude values can be expressed as:

$$\frac{x_n}{x_{n+1}} = e^{2\pi\zeta\frac{\omega}{\omega_D}} \quad (5.21)$$

from which the decay factor is defined as a function of the logarithmic decrement  $\Delta_l$

$$\Delta_l = \ln \frac{x_n}{x_{n+1}} = 2\pi\zeta \frac{\omega}{\omega_D} \approx 2\pi\zeta \quad (5.22)$$

$$\zeta = \frac{\Delta_l}{2\pi} \quad (5.23)$$

### 4.3.3 Control of suction: axis translation technique

Under natural condition pore-air pressure of unsaturated soil is typically atmospheric and, as a consequence, no-zero suction values correspond to negative pore-water pressure values.

$$s = u_a - u_w > 0 \text{ and } u_a = p_{atm} \rightarrow u_w < 0$$

As a consequence, during laboratory tests cavitation could occur, due to negative pore-water pressures developed inside drainage circuits. For this reason different techniques have been developed for controlling suction, by imposing a certain value of the quantity  $(u_a - u_w)$  around the sample to allow for positive pore-water pressure. Different methods are available: axis translation and osmotic techniques, if soil suction is measured through liquid water, or control of environmental moisture technique, if the measurement occur through vapour.

The axis translation technique is the most common method to control matric suction under unsaturated conditions. In order to avoid that negative pore-water pressures  $u_w$  develop, positive values are applied and pore-air pressure  $u_a$  and total stress  $\sigma$  are consequently chosen so that desired levels of net stress tensor  $(\sigma - u_a)$  and matric suction  $(u_a - u_w)$  are reached. In this way cavitation inside drainage circuits could be avoided and pore-water pressure can be measured through conventional transducers, even if natural soil suction is prevented.

The experimental procedure described above requires the application of air-pressure at the top or bottom base of the sample (it depends on the specific layout of the apparatus) and, as a consequence, a partial desaturation of drainage circuits could occur. Since the saturation process is one of the main preliminary processes before testing in order to guarantee continuity between the sample and the measuring system, air passage through drainage circuits could be avoided by placing a particular porous stone between the sample base and bottom circuits. It is a ceramic element with small pores (Hilf, 1956), which remains saturated up to high suction values, from which derives the name High Air Entry Value (HAEV) porous disc. It follows that, once saturated, this porous stone is water but not air permeable.

Each HAEV porous disc is characterised by a specific air-entry value, which limits the maximum level of matric suction that can be applied during a suction-controlled test. Furthermore, to reach high values of net stress and matric suction at the same time, high pressure devices are required as experimental equipment.

#### 4.3.4 Setting up of the new NRFIS suction-controlled RCTS

Suction-controlled RCTS apparatus consists of three main parts: the excitation system, the electro-mechanical system and the measurement system, which are all showed in Figure 4. 10 with specific labels.

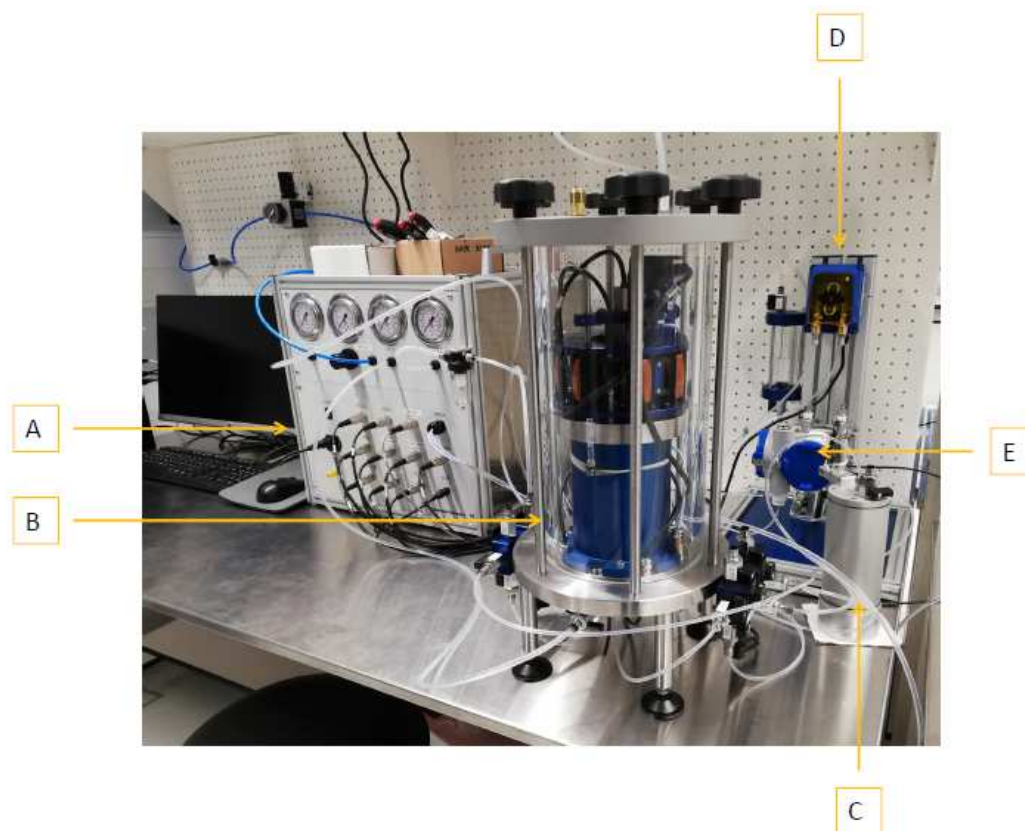


Figure 4. 10 – Suction-controlled RCTS apparatus at NRFIS Geomechanics laboratory (University of Cambridge)

- A. Control box
- B. Pressure cell
- C. Volume gauge
- D. Pump
- E. Differential Pressure Transducer (DPT)

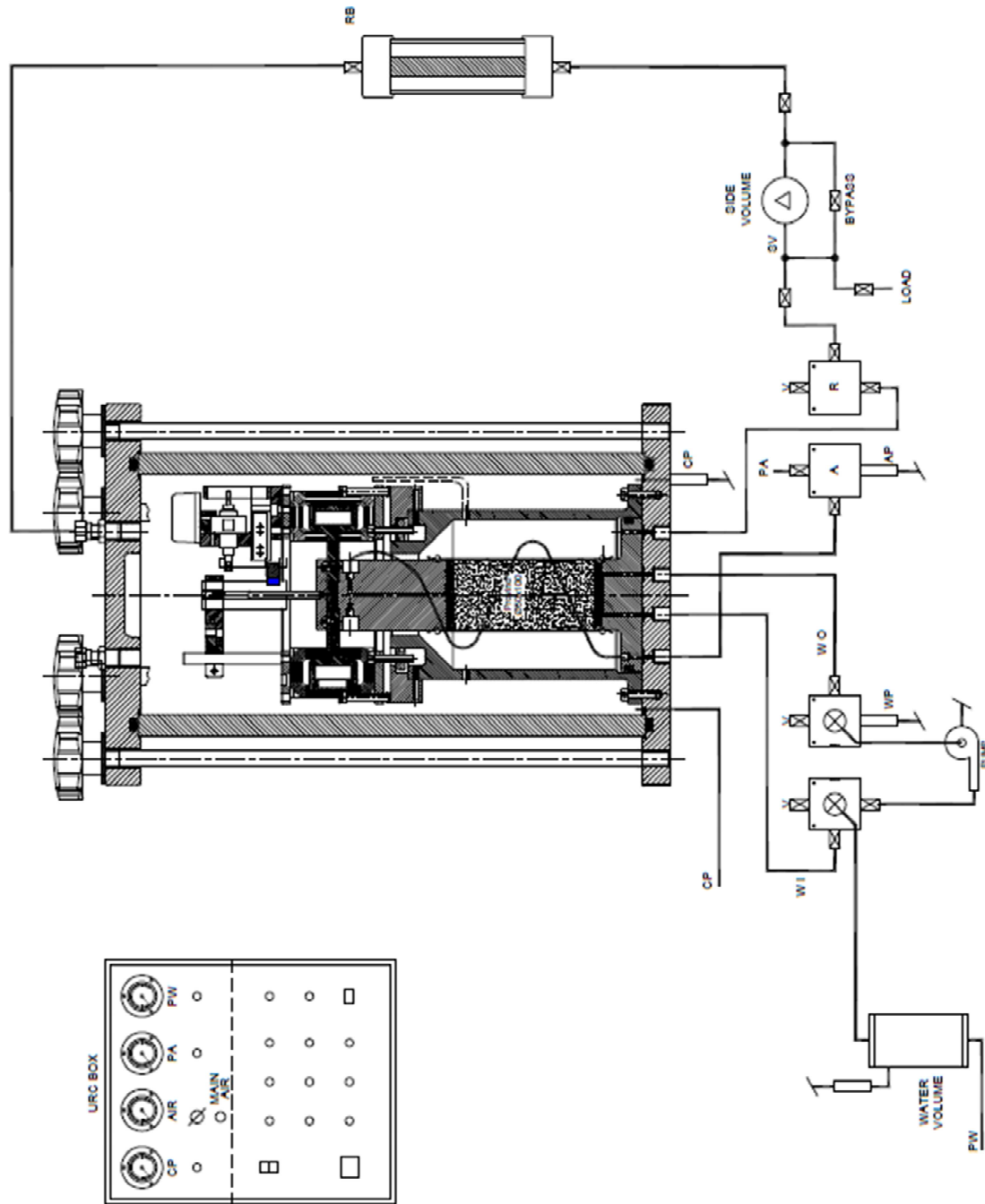


Figure 4.11 – Overall layout of RCTS apparatus at NRFIS Geomechanics laboratory (University of Cambridge)

#### **4.3.4.1 The excitation system**

The excitation system, directly connected to one of oscilloscope channels, consists of:

- Current generator: it generates a sinusoidal control voltage, which corresponds to an output current according to the following relation

$$10 V \rightarrow 2.5 A$$

The effective applied torque is proportional to the output current

$$2.5 A \rightarrow 1.5 Nm$$

- Current amplifier: it amplifies the generated current in order to reduce the dependence on the apparatus head.

#### 4.3.4.2 The electro-mechanical system

The electro-mechanical system is made up of the pressure cell and the torsional oscillator.

The pressure cell (Figure 4. 12-B) consists of a rigid base plate, connected to a steel pedestal, where the sample is placed together with a porous disc and a brass plate, which is characterised by a rough surface to guarantee a solid attachment for the sample. Water pressure is applied through the base pedestal, while air-pressure through the top cap. This specific design choice to separate air and water circuits is a distinctive feature of the present apparatus and it aims to maximize the surface available for water exchanges (or in the same way to minimize the time interval for the equalization stage), to avoid water flow through air circuits and to allow the natural mechanical fluids division (gas to the top). It is important to underline that the thin air circuit surrounding the sample has been designed in order to avoid any additional constrains, so that the required fixed-free test configuration can be guaranteed.

Sample is surrounded by an impermeable membrane fixed to the top and bottom bases by means of O-rings. Sample top base is in contact with a brass plate without a porous disc, since water circuits are concentrated on the bottom side.

The upper plate is made of an aluminium top cap and the torsional oscillator, while the bottom one is crossed by water and air circuits and it allows to fix the internal cylindrical cell (blue in Figure 4. 10), which is filled with water to realize an isotropic confinement for the sample.

The external cylinder is closed by using a steel heavy top cap, which is rigidly connected to the lower plate through steel bar to create an isolated chamber. The external cylinder has been designed to withstand a pressure of 10 bar.

The torsional oscillator consists of a mobile and a fixed part. The mobile part (drive plate) is a metallic plate with four arms, each of them ends with a permanent neodymium magnet, with a rigid connection to the load cell through four screws. The fixed part is made of four couples of coils (Figure 4. 12-D) and each of them is coaxial to the correspondent magnet (Figure 4. 12-E). Each coil is shaped so that the magnet can move as the soil specimen shortens or bends during consolidation.

When a sinusoidal voltage is applied to the coils, it pulls the magnets in one direction and reverses the direction as the sine wave changes from positive to negative. The actual rotational movement of the top cap is determined by the stiffness of the specimen being tested. The present system allows to apply a maximum value of torsional moment equal to 1.5 Nm.

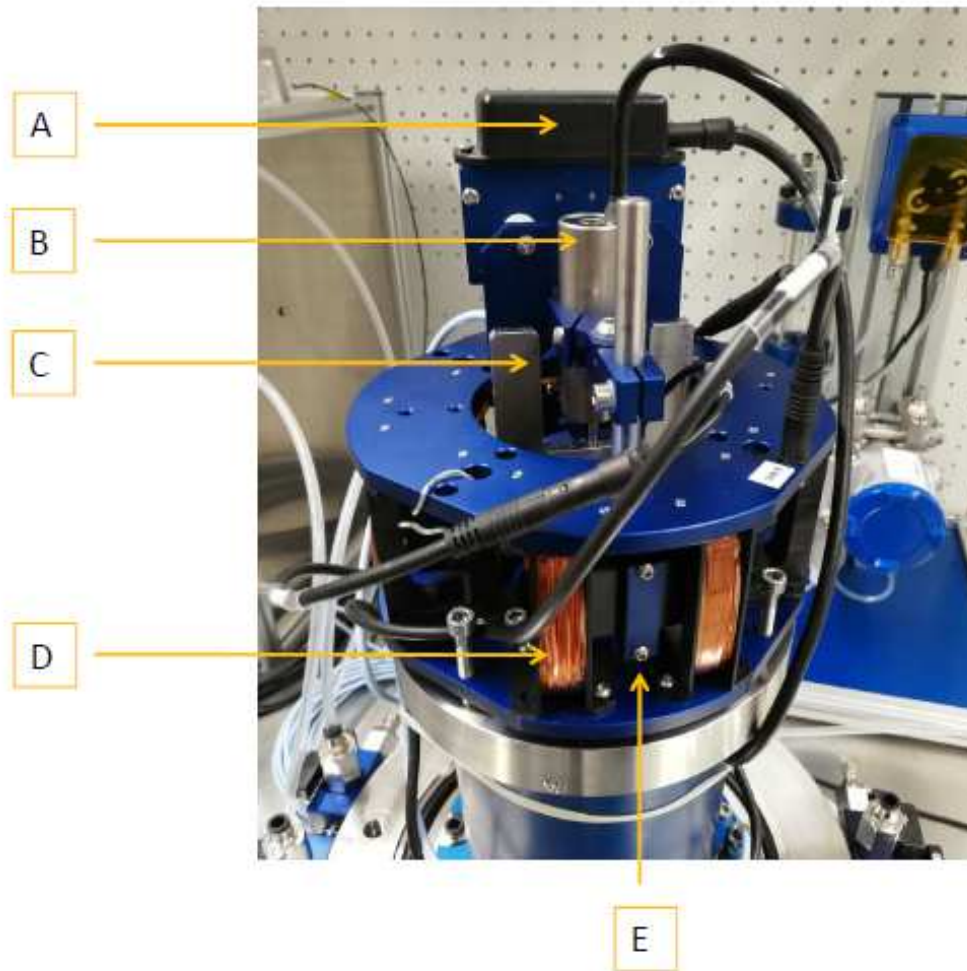


Figure 4. 12 – Electro-mechanical system of RCTS apparatus

A. Accelerometer

B. LVDT

C. Target

D. Coils

E. Magnet

#### 4.3.4.3 The measurement system

The measurement system consists of sensors, which constitute the input of data acquisition and control card and allows to switch from the physical to the electronical world.

A first group of sensors refers to frequencies range between 0.2 and 300 Hz, which are typical of dynamic phenomena during RC and TS tests. Sample is loaded by a torque, applied on the top base and proportional to the current, and it reacts with an angular deformation, variable with the height and measured by using proximity sensors or an accelerometer on the basis of frequency levels.

Sensors related to this process are the following:

- Current sensor: it reads the real value of the applied circulating current;
- Proximity sensors (Figure 4. 13-B): it is a couple of sensors, placed at a relative distance of 5 cm and directed towards an U-shaped metallic target (Figure 4. 13-C). They are non-contact transducers, which measure displacements of the target, in contact with the mobile part of the torsional motor. The target is placed orthogonally with respect to proximity sensors, which use a passive measuring method, through the evaluation of energy dissipation of currents circulating inside metal and without any contacts with target. Two transducers are used to avoid the influence of bending on horizontal displacements.

The result of measurements is a voltage, which represents sample head rotation, which varies with amplitude. As a consequence, measuring small angular deformation is difficult and proximity sensors are used for low frequency values.

- Tangential accelerometer (Figure 4. 13-A): it is a piezoelectric accelerometer rigidly connected to one of the four arms of the drive-plate, at a distance  $r_a$  from the rotation axis. On the opposite arm a cylinder with the same mass is installed to balance masses. During dynamic tests the accelerometer measures an electrical signal proportional to the drive-plate tangential acceleration: this value divided by  $r_a$  represents the sample head angular acceleration. By means of double integration in time domain, head rotation and strain level can be computed.

The accelerometer has a full scale of  $\pm 8 g = \pm 80 \frac{m}{s^2}$  and it is used at high frequency values.

- Vertical accelerometer: it used to control the planarity of oscillation.

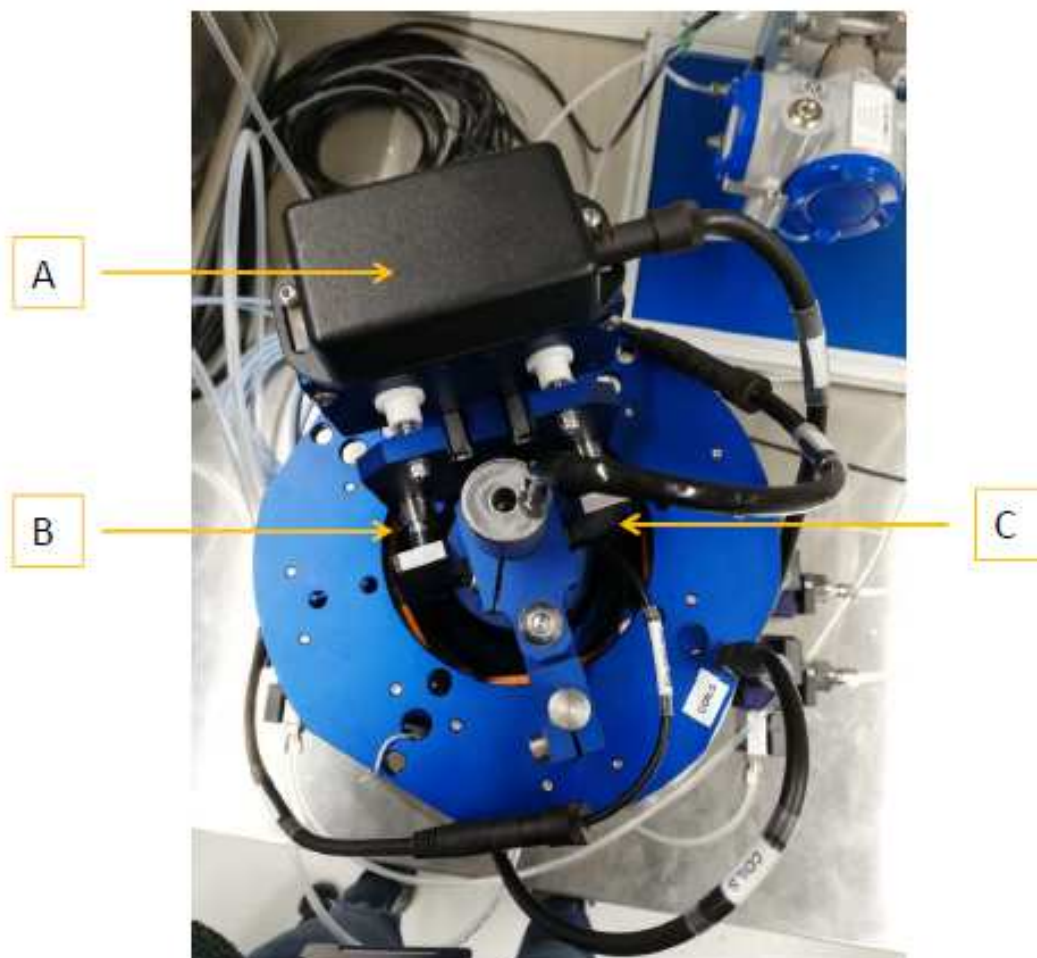


Figure 4. 13 – High frequencies measurement sensors

A. Tangential accelerometer

B. Proximity sensors

C. Target

A second group of sensors refers to frequencies between 0 and 0.2 Hz, typical of geotechnical phenomena. In the following section, sensors belonging to this group are described.

RCTS cell allows for the independent control of cell, pore-water and pore-air pressures, using three electro-pneumatic regulators (Control Box-Figure 4. 10-A). Suction is imposed by means of the axis translation technique and it can reach a maximum of 5 bar, which corresponds to the air pressure value of the chosen HAEV (high air entry value) porous disc. It means that the HAEV porous disc, once saturated, allows the passage of only water until a certain value of air entry pressure (5 bar for this specific case).

Volume changes are evaluated by combining axial and radial measurements. Two main characteristic dimensions are identified: sample diameter (38 or 50 mm) and a reference diameter, which is equal to the width of the cell neck (in the circle – Figure 4. 14).

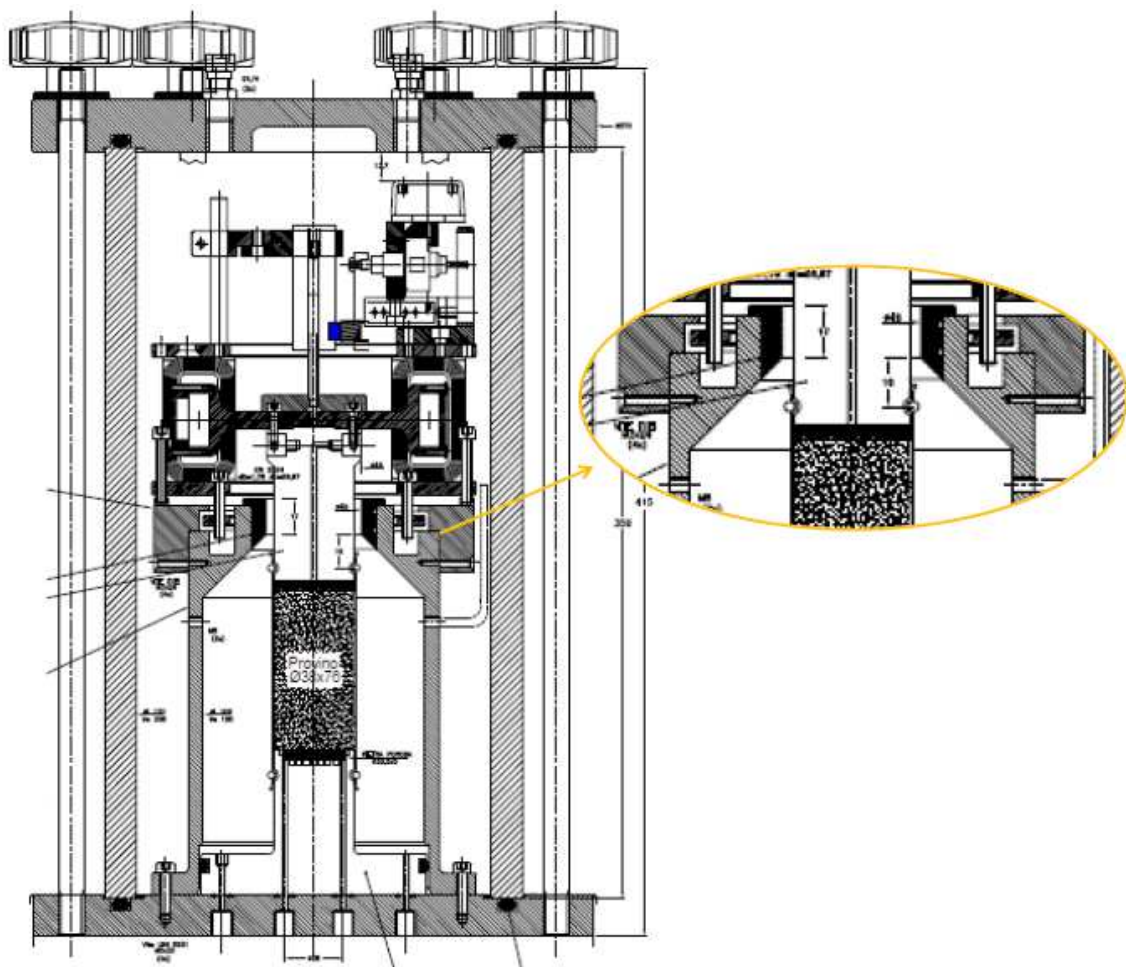


Figure 4. 14 – Details of measurements system of radial volume changes

Each of the two diameters corresponds to a cross section area and the difference between the two cross sections represents an annulus surface  $\Delta S$ , filled with water

during the test (differential surface per mmH<sub>2</sub>O). The differential pressure transducer DPT (Figure 4. 10-E) measures the difference in terms of piezometric height between the reference burette and the cell. This difference initially is equal to zero due to the presence of a by-pass, which allows to equalize internal and external water levels before starting test.

Torque applied to the sample head leads to volume deformation, which is described by means of two strain components:

- Reduction of sample height  $\Delta h$ , measured by means of a LVDT (Figure 4. 12-E) coaxial to the specimen;
- Increment of the water level inside the cell  $\Delta q$ , measured by the DPT.

Sample volume changes are computed by applying the following equation:

$$\Delta V = \Delta q \cdot \Delta S - \Delta h \cdot S \quad (5.24)$$

where S is the sample cross section and  $\Delta S$  is the annulus surface.

Water level changes are related to DPT readings through the following relation

$$1 \text{ mbar} = 0.1 \text{ kPa} \rightarrow 1 \text{ cm}_{H_2O}$$

Water content changes are measured through an external volume gauge (Figure 4. 10-C) connected to the cell by means of water circuits. The volume gauge has a maximum capacity equal to 50 cc.

The output of the data acquisition and control card are actuators, which allow translation from the electrical to the physical world. They are listed in the following:

- Cell, pore water and pore pressure actuators, which are electro-pneumatic converters (Watson-Smith). Given a certain feedback pressure, an electro-pneumatic converter generates an electrical signal and converts it in an out-pressure;
- Pump (Figure 4. 10-D), which is used to saturate circuits;
- Power current amplifier;
- Motion system, to zero proximity sensors.

#### 4.3.4.4 Calibration process

Each sensor requires a calibration process, which is based on the identification of a physical-electrical transfer function, interpolated by a straight line with small errors. The most relevant step of calibration process of the present apparatus regards the inertia of the head  $J_o$ , achieved through both geometrical and experimental computations. The former is based on specific weights of each component and relative distances, while the latter follows the conventional procedure of calibration (Isenhower 1979). A calibration rod with given inertia and stiffness is subjected to a series of RC tests and the resonance frequency is measured by referring to two different test configurations, with and without a calibration mass of known polar inertia. Since the calibration rod has a high deformability and a negligible inertia, the mass-rod system can be schematized by considering a SDOF, with the mass concentrated on the motor and the deformability on the calibration rod.

According to this scheme, the resonance frequency of the system is equal to

$$f_R = \frac{1}{2\pi} \sqrt{\frac{K}{I}} \quad (5.25)$$

where K is the torsional stiffness of the calibration rod and I is the inertia of the rigid mass placed on the top.

The presence of the calibration mass reduces the resonance frequency  $f'_R$  of the mass-rod system with respect to the initial value  $f_R$  (single rod)

$$f'_R < f_R$$

Once computed the resonance frequency of both configurations, a system of two equations with two unknowns (head inertia and rod stiffness) can be written and solved.

By analysing results of the adjustment process, the main limit of this apparatus is the sensibility in terms of volume changes (equal to 1.2 %).

### 4.3.4.5 RCTS software

The developed software shows different control windows.

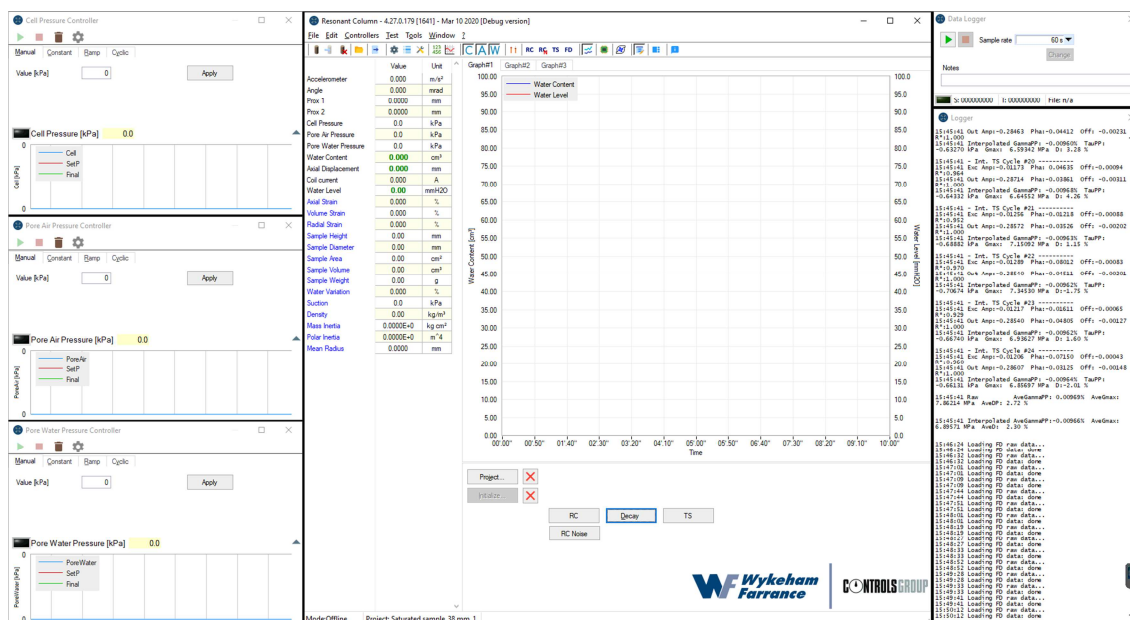


Figure 4. 15 – Software control windows

Three of them regard cell, pore water, pore air pressures (on the left in Figure 4. 15) and they allow to apply or change pressure levels by means of four different methods:

- Manual method, which allows for a direct control by specifying the final SetPoint value;
- Constant method, which generates a control in loop through actuators. In this way the chosen SetPoint is reached in a longer time interval and then it remains constant;
- Rump method, which requires to specify both the SetPoint and the rise rate;
- Cyclic method, which is characterised by a minimum and a maximum pressures, rise and fall rates, time duration and the number of cycles.

The main window (in the centre of Figure 4. 15) shows on the left a list of all measured (black) and computed (blue) variables with the actual values reached during the test, while in the central area it shows a graph plotting the time

variation of two chosen variables, specified in the legend. In the same central windows are placed command buttons to start testing.

A conventional unsaturated RCTS test is characterised by four stages: equalization, isotropic consolidation, Resonant Frequency and Torsional Shear test.

The first stage represents an additional step with respect to the standard saturated procedure, since the present apparatus is suction-controlled and it is possible to perform test both in saturated and unsaturated conditions. The equalization stage is required to bring soil specimens to target values of matric suction and it involves imposing a chosen suction level through the axis-translation technique and waiting for the pore-water pressure to equalize.

The following stage is the isotropic consolidation, which aims to restore in situ effective stress by imposing an isotropic compression through compressed air, in order to avoid a direct contact between water and electrical wires.

As regards the last step, **four different test methods** can be distinguished:

- RC (standard): frequency is gradually increased in discrete steps with a defined sequence. The resonant frequency is the one with the maximum response amplitude. This test usually consists of two steps, the first with a wide frequencies range and the second one characterized by a smaller range around the resonance;
- RC chirp: in order to minimize the effects of the number of cycles and the time interval, standard RC test is no longer used and it has been replaced by **RC chirp test**, characterised by a Chirp linear frequency modulation. The Chirp is a continuous modulation where the frequency varies within limits set by the user;
- TS: a torque is applied by means of the electro-magnetic motor and it is proportional to the electrical signal, characterised by a constant frequency (main difference with respect to RS test) and an increasing amplitude. The system records torsional stress and strain values for each amplitude and displays hysteresis cycle, from which G and D are determined.
- Free-Decay: it allows to apply a torque with a frequency equal to the resonance one (which needs to be already known) and a time duration, following by a free-decay stage, from which the decay factor is derived.

Data logger window (on the right in Figure 4. 15) allows for data acquisition with a frequency variable between 1Hz and 60 seconds.

### 4.3.5 Saturation of the HAEV porous disc under pressure and permeability test

Each test requires the saturation of all water circuits, water pressure transducers and the HAEV porous disc, by using demineralized and de-aired water.

The procedure followed to saturate HAEV porous disc differs from the conventional one, which requires to boil the porous stone to let air bubbles going out from internal pores. This procedure cannot be applied in the present apparatus, since HAEV porous disc is rigidly fixed to the base (Figure 4. 16(b)). For this reason, firstly a filtration motion is induced through the plate by imposing a gradient between cell and pore-water pressures, set to 600 kPa and 18 kPa respectively. The applied value of the cell pressure is chosen in order to overcome the porous disc AEV, equal to 5 bar (Figure 4. 17), while the pore-water pressure corresponds to the offset value (minimum). By setting pressure values as described, a gradient of 570 kPa results between the two sides of the porous disc and a filtration motion starts from the upper towards the lower base. At the beginning, the porous stone is dry and it absorbs all flowing water, which gradually increases its degree of saturation and, as a consequence, water volumes start flowing out the stone. Filtrated water volumes flow through bottom circuits (Figure 4. 16(a)), ending in the volume gauge.

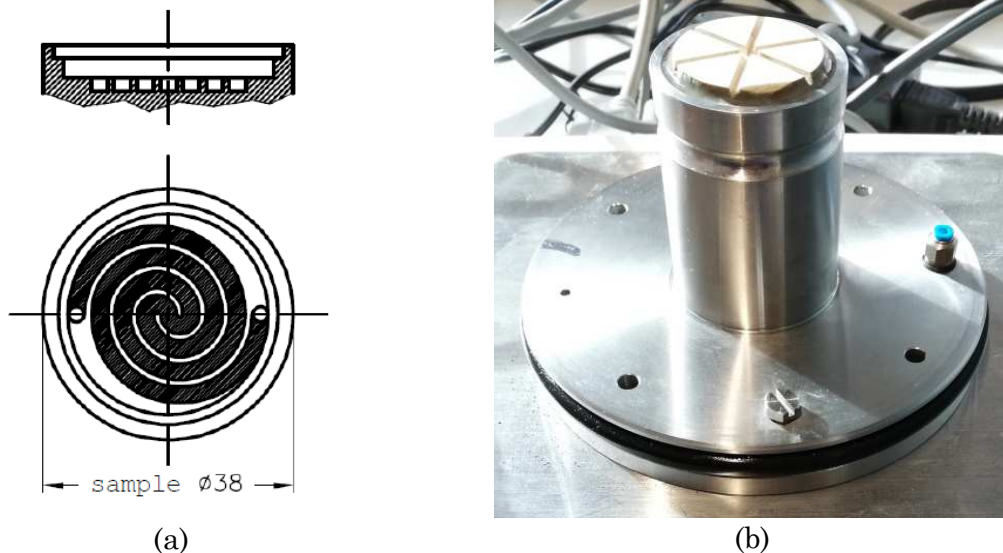


Figure 4. 16 – (a) Schematic representation of the bottom drainage circuit and cross section of 38 mm HAEV porous stone and (b) picture showing the 38 mm porous stone rigidly fixed to the base

The volume gauge allows to measure the amount of water [cm<sup>3</sup>], which flows out from the cell during a certain time interval. By combining water content changes and the porous disc geometry, the flow rate [cm/s] can be monitored.

In Table 4. 1 are listed all theoretical properties of the specific porous stone in terms of theoretical flow rate, computed by applying Darcy's law once known the saturated hydraulic conductivity from catalogue (1.21E-7 cm/s) (Figure 4. 17) and the applied hydraulic gradient  $i$ .

AIR ENTRY VALUE	BUBBLING PRESSURE (PSI)	APPROXIMATE POROSITY (% vol.)	SATURATED HYDRAULIC CONDUCTIVITY (cm/sec)	MAXIMUM PORE SIZE ( $\mu$ m)	FLOW THROUGH 1/4-INCH PLATE (ml/hr/cm <sup>2</sup> /14.7 psi)
5 BAR (-B05M1)* STANDARD FLOW	80	31%	1.21 x 10 <sup>-7</sup>	.5	.7

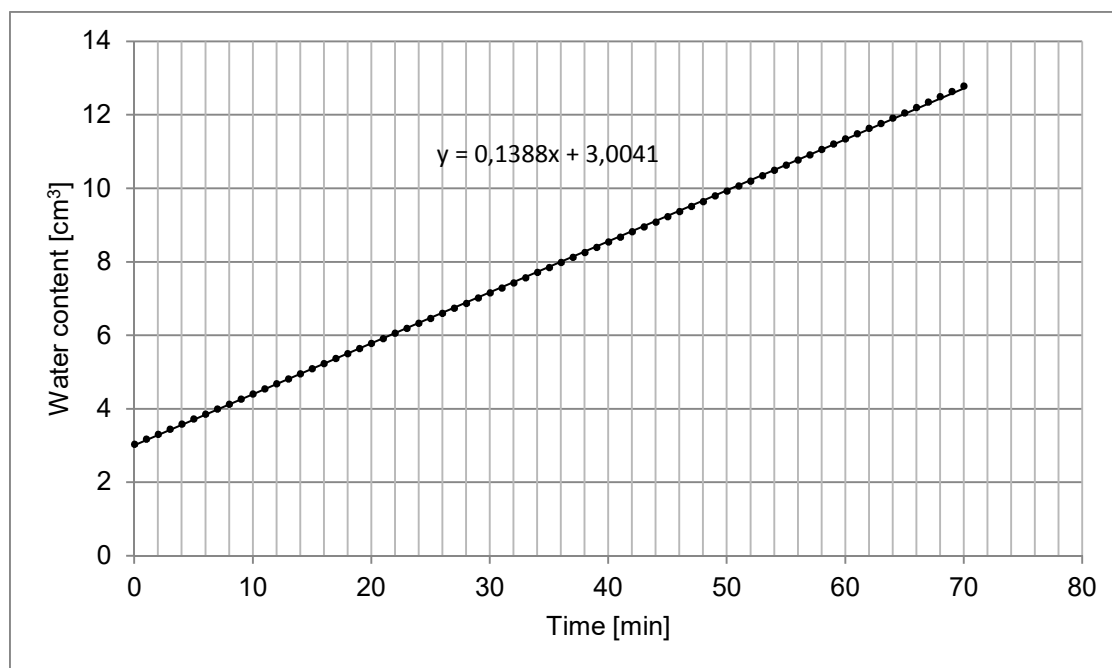
Figure 4. 17 – Main specifications of the 5 bar standard flow porous stone (SOILMOISTURE EQUIPMENT CORP. CERAMICS CATALOG)

Table 4. 1- Summary of theoretical hydraulic and geometrical properties

Theoretical permeability $k_{teor}$ [cm/s]	1,21E-07
Diameter [cm]	2,86
$A_{cross}$ [cm <sup>2</sup> ]	6,42
Height [cm]	0,75
Top pressure [kPa]	570
Bottom pressure [kPa]	18
Hydraulic gradient $i$ [-]	7504
<b>Theoretical flow rate <math>v</math> [cm/s]</b>	<b>0,0009</b>

Once computed the theoretical flow rate  $v$ , a permeability test can be performed to compare theoretical and effective porous disc permeability.

Graph 4. 1 shows the amount of water flowing out from porous stone during the induced filtration motion. The slope of the line in the water content-time plane corresponds to the effective flow rate through the disc and it results approximately equal to 0,14 cm<sup>3</sup>/min.



Graph 4. 1 – Effective flow rate computation in the water content-time plane

By applying Darcy's law the effective permeability  $k_{real}$  corresponding to measured flow rate can be computed, once known the imposed hydraulic gradient  $i$ :

$$k_{real} = 4,8E - 8 \text{ cm/s}$$

The comparison between theoretical  $k_{teor}$  (Table 4. 1) and effective hydraulic conductivity  $k_{real}$  shows that the measured one results one order of magnitude lower than the expected value.

Since the measured flow rate (Graph 4. 1) follows a constant linear path under the applied hydraulic gradient during a time interval longer than 24 hours, permeability test reaches stationary conditions. It follows that the hydraulic conductivity declared by the producer can be assumed as modified. It can be justified by considering surface finishing carried out on porous stone to make it enough rough to guarantee the proper adhesion with specimen bottom base (Figure 4. 16(b)).

It follows that the HAEV porous disc saturation process can be assumed as completed.

#### 4.3.6 Saturation of the HAEV porous disc under vacuum

An alternative saturation technique is useful to allow release of air bubbles still trapped inside stone pores, since probably the previous application of high pressure (6 bar) on de-aired water surrounding the porous stone inside the cell determined air dissolution in the liquid, even inside stone pores.

Since the porous disc is installed in the bottom base, typical saturation technique, such as boiling, are not applicable. Therefore, in order to induce a free motion of air bubbles out from pores, both 38 and 50 mm porous discs are immersed into a cylindrical reservoir filled with water and put under vacuum by means of a vacuum pump.

In the following figures are showed the setting up of the saturation process (a) and two detailed photos, focusing on the 50 mm porous disc (b), which was completely dry at the beginning of the process and on 38 mm stone already saturated under pressure (c). The presence of micro-bubbles going out from the smaller porous disc shows the effectiveness of this procedure in allowing a full saturation process.

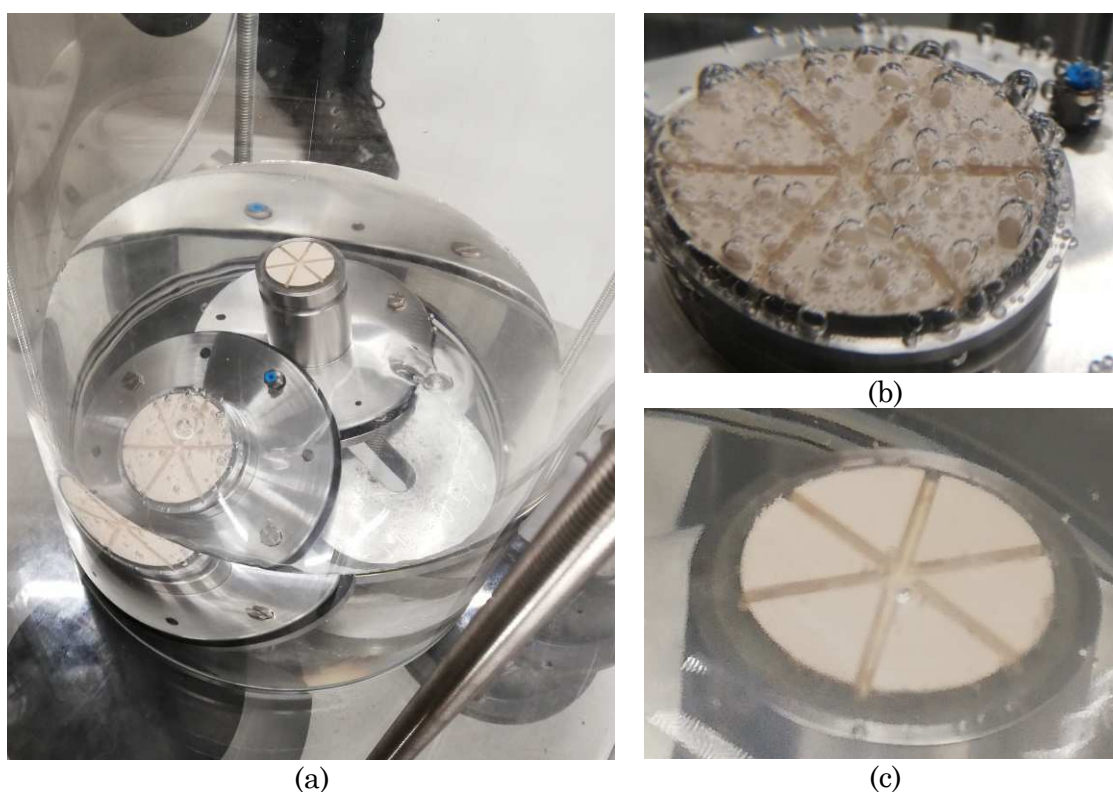


Figure 4. 18 – (a) Equipment for the saturation process of the HAEV porous disc under vacuum and detailed pictures of (b) 50 mm and (c) 38 mm porous discs

### 4.3.7 Preparation of reconstituted samples

To investigate small and medium strains behaviour of tested material, reconstituted samples are prepared from a slurry, as proposed by Burland (1990). Slurry is obtained by adding distilled water to dry soil in order to reach a water content between 1.25 and 1.5 times the measured Liquid Limit (LL) (Chapter 3.4.2). In Table 4. 2 initial properties of the Black Cotton Clay slurry are listed:

Table 4. 2- Initial properties of Black Cotton clay slurry

LL [%]	87	$S_r$ [%]	100
$w_0$ [%]	121	$G_s$ [-]	2,54
$w_0/LL$ [-]	1,39	$e_0$ [-]	3,071

According to the conventional procedure, once mixed, slurry is sealed for at least 24h to reach an homogeneous water content and, then, it is poured in a 100 mm consolidometer, (Figure 4. 19) in order to get three samples with a diameter equal to 38 mm.



(a)



(b)

Figure 4. 19 – (a) Initial conditions of slurry in the 100 mm consolidometer after pouring process and (b) 100 mm reconstituted Black Cotton clay sample

The consolidation process evolves according to a loading sequence equal to 0,51/ 4,7/ 12,5/ 25/ 50/ 100 kPa, obtaining the following consolidation curves (Figure 4. 20 and Figure 4. 21):

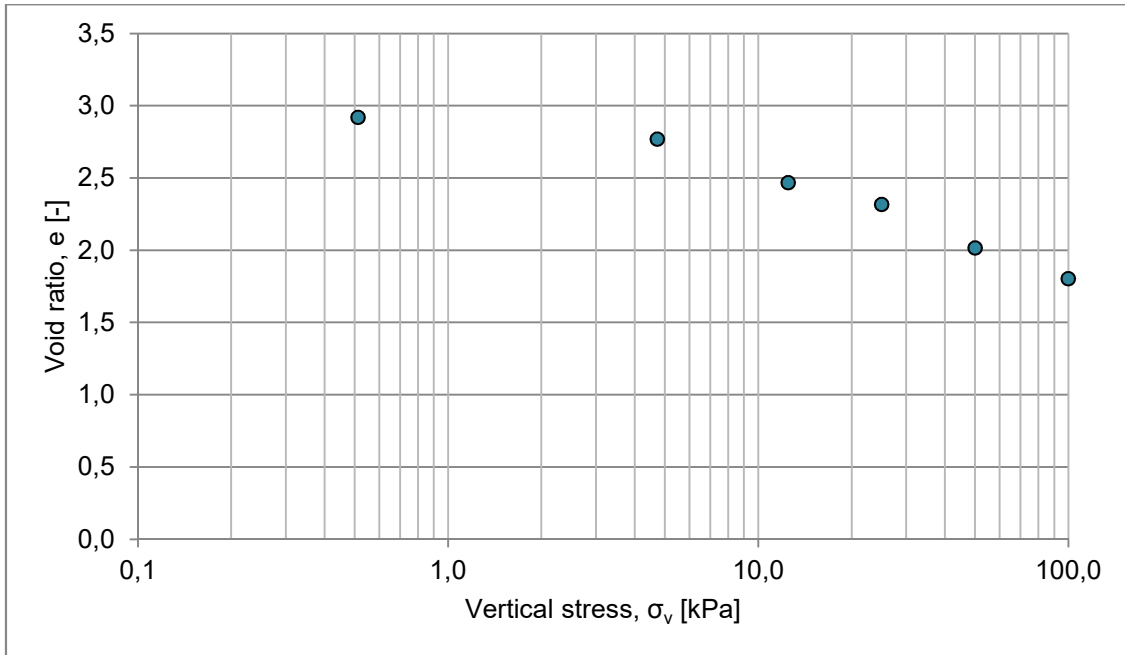


Figure 4. 20 - Consolidation curve plotted in the void ratio-vertical stress plane

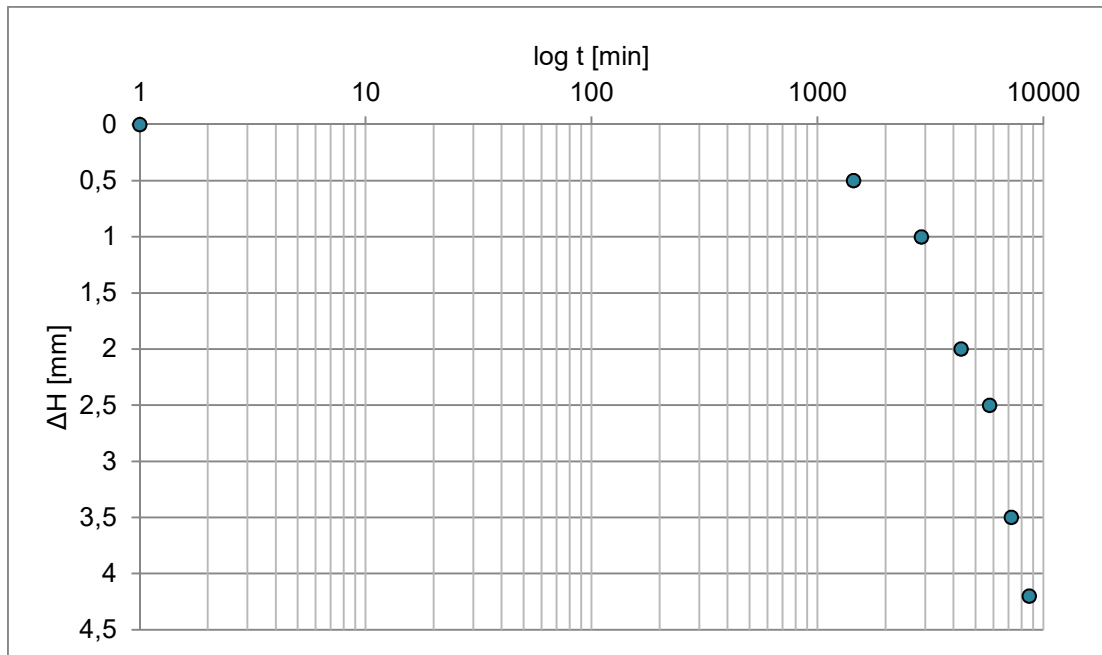


Figure 4. 21 – Consolidation curve plotted in the semi-logarithmic vertical settlement-time plane

## 5. Results

### 5.1 Introduction

In the following chapter results of both experimental works are illustrated. Soil suction measurements, carried out through WP4C device, are showed in terms of Soil-Water retention curves, plotted as a relation between the logarithm of suction and either degree of saturation  $S_r$ , void ratio  $e$  or gravimetric water content,  $w$ . Differences between Atta Clay and Black Cotton Clay are highlighted and justified by referring to material properties, as resulting from the characterisation process. As regards RCTS tests, setting up of the saturated test, consolidation phase and cyclic loading phase are illustrated and each step is fully described by attaching photos of testing apparatus and samples and screenshots of the main software windows.

### 5.2 SWRCs

Soil-Water Retention Curves (SWRCs) represent soil response during drying and wetting process. They are often expressed in the total suction (logarithmic scale) - degree of saturation plane, but alternative representations involve other variables as y-axis, like void ratio or gravimetric water content.

The two following sections illustrate the Primary Drying Curve (PDC) of SWRCs for both tested high-plasticity tropical clays, Black Cotton and Atta Clay respectively. Total suction is measured on four reconstituted sample disc for each material, using the dewpoint device technique, as described in chapter 4.2.

In both cases red points represent results of the present research work, while black ones are taken as reference from a previous hydraulic characterisation, made on the same tropical clays (Abdalla *et al.* 2019), in order to confirm unsaturated behaviour of tested soils.

#### 5.1.1 Black Cotton clay SWRCs and comparison with previous results

Four reconstituted Black Cotton Clay discs are prepared and left to dry under laboratory conditions in order to measure, approximately once a day, total suction through the dewpoint device technique and diameter and height changes by using a caliper. Consequently, volume changes, degree of saturation and gravimetric

water content can be computed for each daily step. As described in chapter 4.2, the chosen suction technique has an upper measuring limit equal to -300 MPa, which does not allow to investigate the full drying curve for the tested material, since it corresponds to a degree of saturation  $S_r=39\%$ , as shown in Figure 5. 1.

In Table 5. 1 average soil characteristics at the beginning of the drying process are listed, in terms of gravimetric water content, degree of saturation and void ratio.

Table 5. 1 – Initial hydraulic conditions of Black Cotton clay samples

$S_r$ [%]	100
$w$ [%]	79
$e$ [-]	2,2

In Figure 5. 1, Figure 5. 2, Figure 5. 3, Figure 5. 4, Figure 5. 5 resulting PDC of Black Cotton Clay SWRCs are plotted in terms of gravimetric water content, total suction, degree of saturation and void ratio.

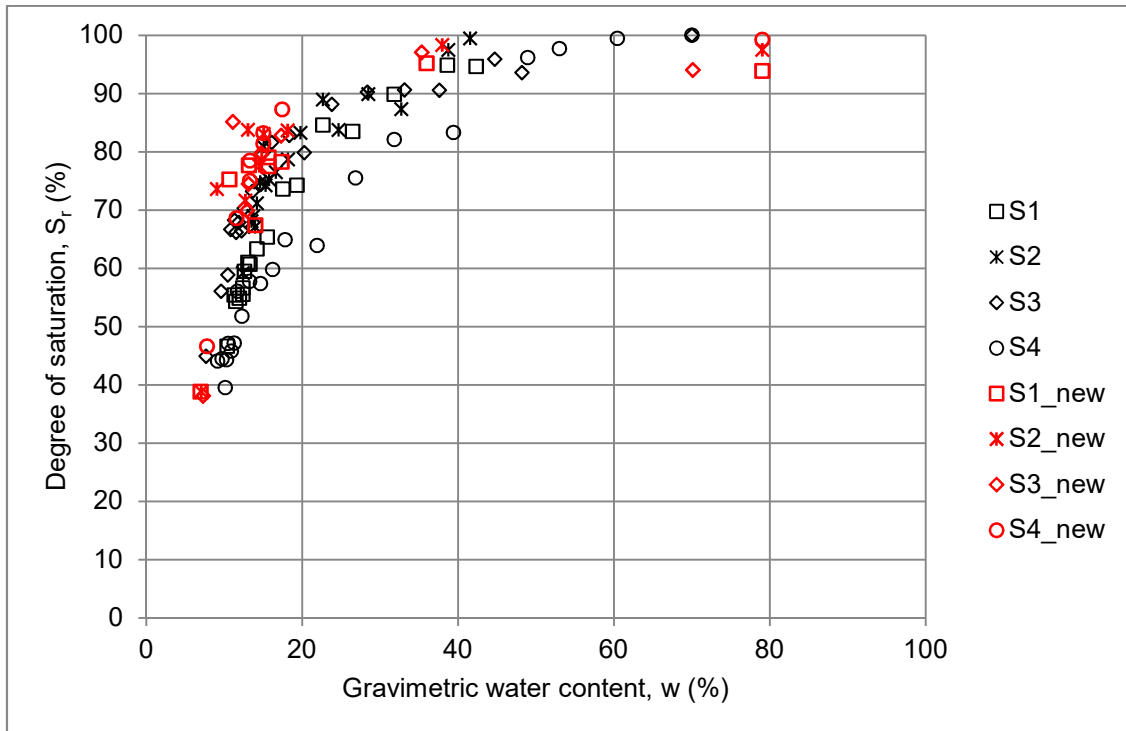


Figure 5.1 – Black Cotton clay SWRCs and comparison with previous results (after Abdalla *et al.*, 2019) in the degree of saturation-gravimetric water content plane

In Figure 5.2 PDC of SWRC is plotted in the total suction – degree of saturation plane and it shows that samples remained almost saturated ( $S_r=91\%$ ) up to suction levels of about 2 MPa., even if the four tested discs show a wide spread of results, so an average trend has been considered in order to get a global evaluation of clay behaviour. In addition, a rapid decrease of the degree of saturation at constant suction (about 100 MPa) is observed.

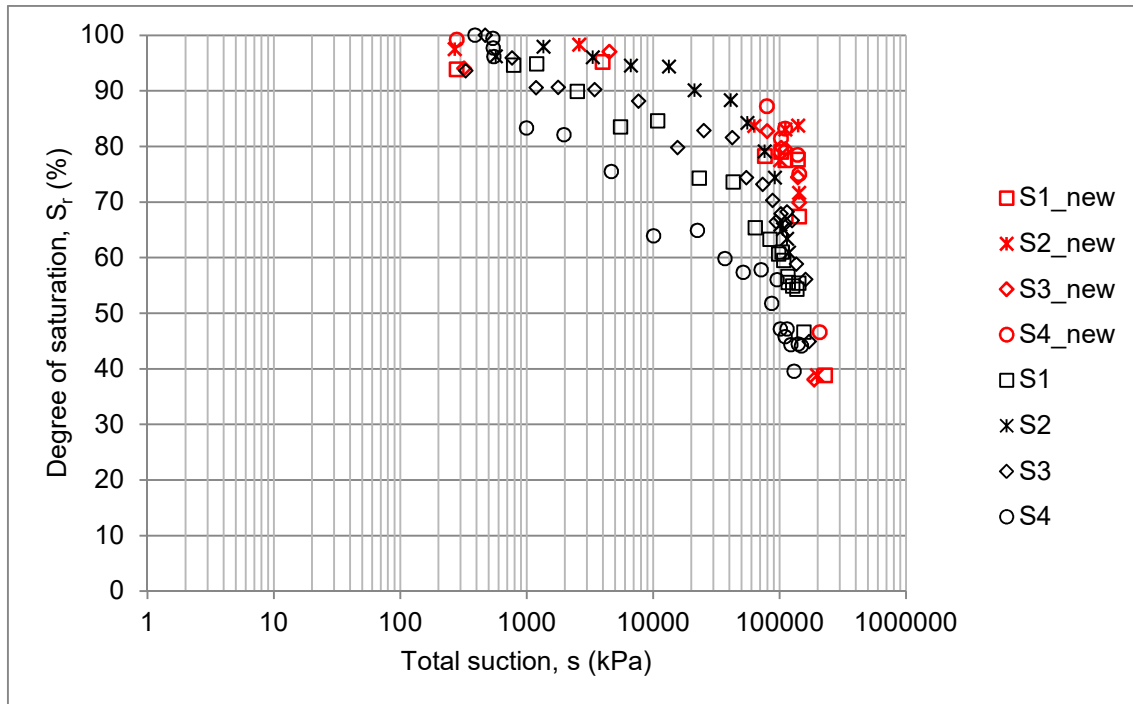


Figure 5.2 – Black Cotton clay SWRCs and comparison with previous results (after Abdalla *et al.*, 2019) in the degree of saturation-total suction plane

Figure 5.3 illustrates first drying process results in terms of volume change, expressed by void ratio, as a function of gravimetric water content and often referred as a shrinkage curve.

During drying process three stages can be distinguished (Abdalla *et al.*, 2019):

- saturated stage, which means that any loss of water volume is equal to the same reduction in total volume;
- transition stage, when the loss of water volume is greater than the reduction in overall volume and the sample becomes unsaturated;
- shrinkage stage, when sample stops shrinking and the overall volume remains constant, since any loss of water volume is reflected by an equal change of air volume.

In Figure 5.3 the saturation line ( $S_r=100\%$ ) is plotted by considering the known relationship between void ratio and gravimetric water content, corresponding to the proper value of soil specific gravity  $G_s=2.54$ . It results that Black Cotton Clay shrinkage line follows the saturation line (saturated stage) up to a gravimetric water content of 38%, below which the transition stage develops until the shrinkage limit. This limit is identified as that point where gravimetric water content continues to decrease while void ratio (overall volume) remains constant,

which means that water volume changes correspond to air volume ones. Shrinkage stage starts at  $w=18\%$  and  $e=0.4$ .

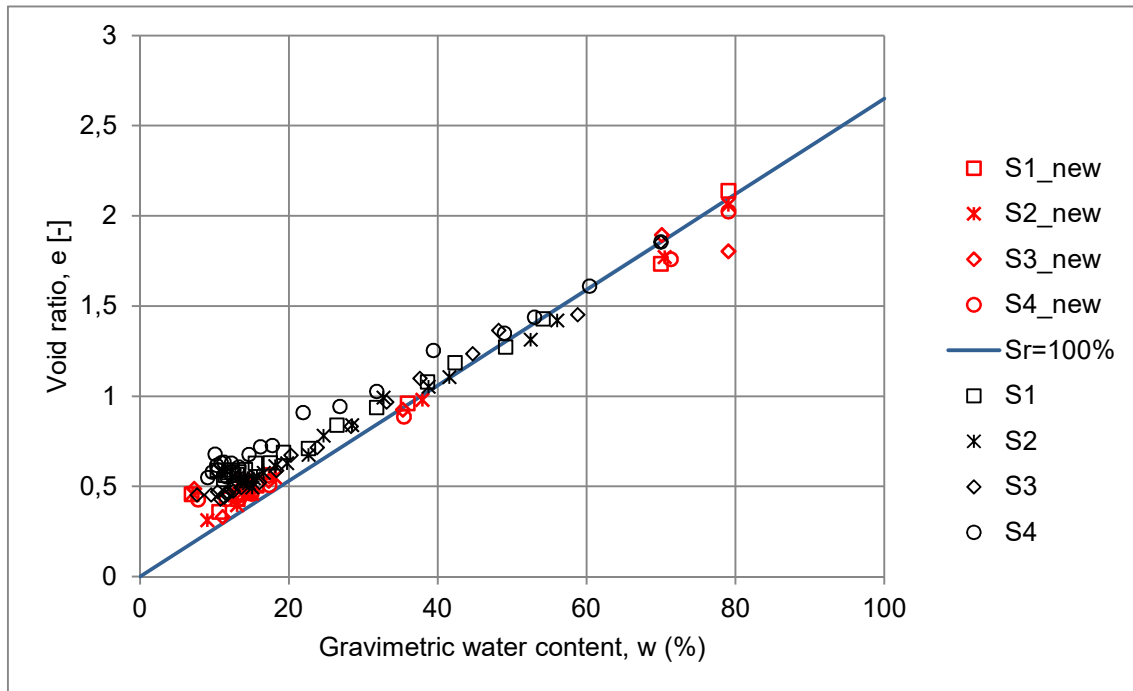


Figure 5.3 – Black Cotton clay shrinkage line and comparison with previous results (after Abdalla *et al.*, 2019) in the void ratio-gravimetric water content plane

In Figure 5.4 PDC of SWRC is plotted in terms of void ratio and total suction (logarithmic scale). During drying process suction progressively increases and soil behaviour is governed by shrinkage, which leads to a negative volume change (compression) due to hydraulic effects rather than applied total stress. As a consequence, curve plotted in Figure 5.4 is similar to compression curves obtained by performing oedometer tests.

Compression trend changes at suction level of about 1 MPa up to the dewpoint device technique limit of 300 MPa, where the void ratio becomes constant (Abdalla *et al.*, 2019), since this point corresponds to the shrinkage limit ( $e=0.5$ ).

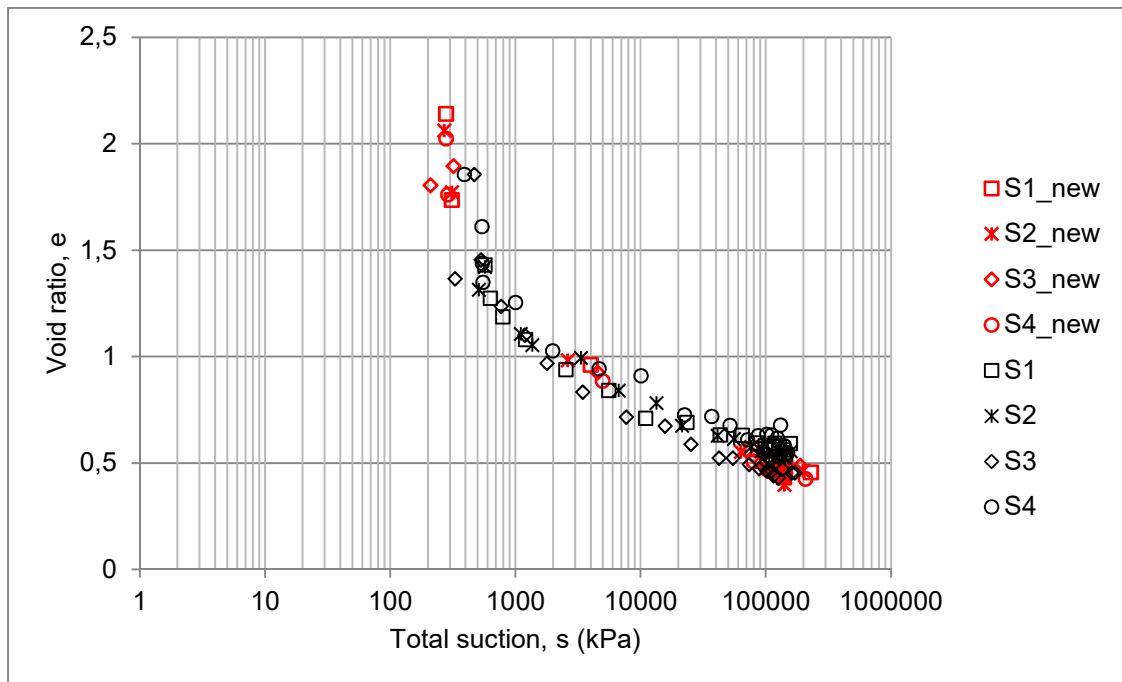


Figure 5. 4 – Black Cotton clay SWRCs and comparison with previous results (after Abdalla *et al.*, 2019) in the void ratio-total suction plane

Up to suction value of 2 MPa (saturation limit) gravimetric water content reduces from 79% to 40% without any relevant increases in total suction. From this point decreases in gravimetric water volume rapidly develop up to the end of PDC, where the limit of the dewpoint suction measurements is reached at  $w=7.8\%$  (Figure 5. 5).

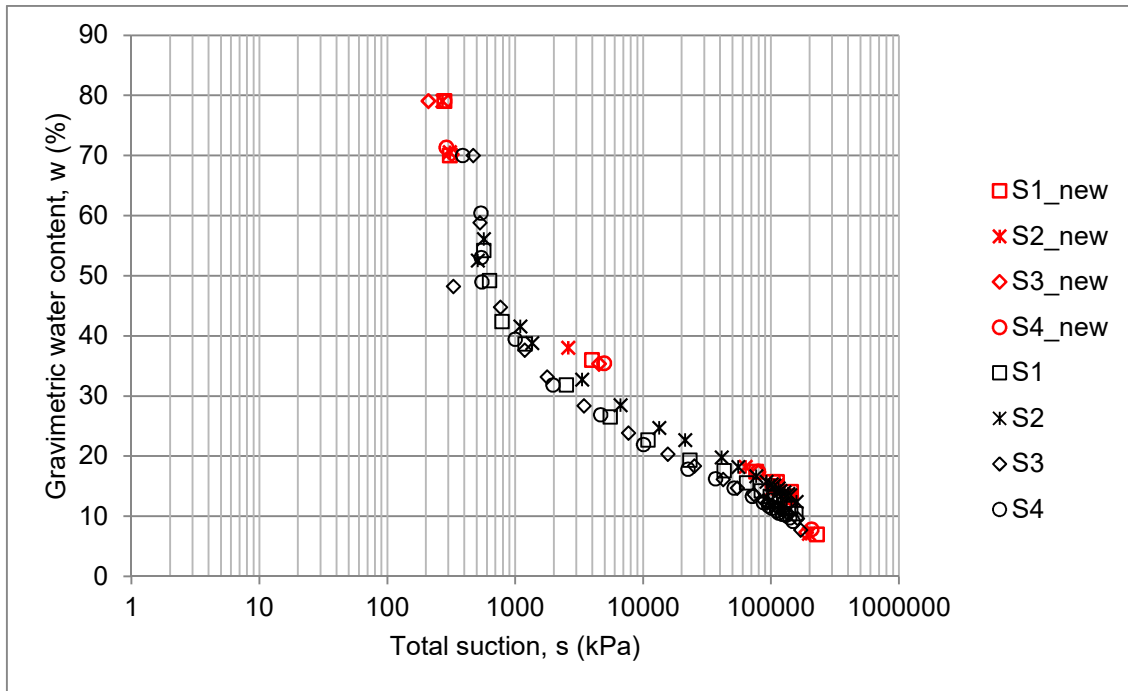


Figure 5. 5 – Black Cotton clay SWRCs and comparison with previous results (after Abdalla *et al.*, 2019) in the gravimetric water content-total suction plane

### 5.1.2 Atta Clay SWRCs and comparison with previous results

Similarly to Black Cotton Clay, four reconstituted discs are prepared and left to dry under laboratory conditions and SWRC variables are measured and computed as described in chapter 4.2.

Average initial soil characteristics, in terms of gravimetric water content, degree of saturation and void ratio, are listed in Table 5. 2:

Table 5. 2- Initial hydraulic conditions of Atta clay samples

$S_r$ [%]	100
$w$ [%]	63
$e$ [-]	3.03

As shown in Figure 5. 6, Atta Clay gravimetric water content changes between 114% and 3.42%, which is reached at the limiting suction of 300 MPa.

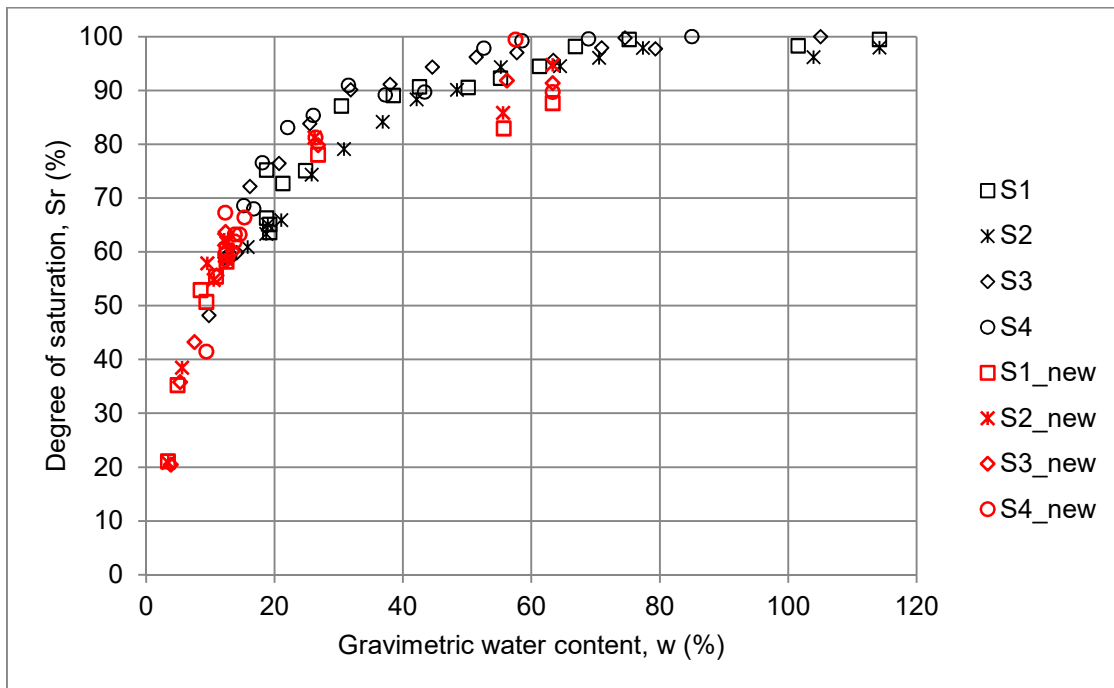


Figure 5. 6 – Atta clay SWRCs and comparison with previous results (after Abdalla *et al.*, 2019) in the degree of saturation-gravimetric water content plane

One of the main differences with respect to previous data regards the saturation level at the limit of dewpoint method, which results lower ( $S_r=20\%$ ) than Black Cotton Clay ( $S_r=40\%$ ), since Sudanese soil is more plastic with high fine content, so

greater suctions are generated at comparable stages (Abdalla *et al.*, 2019), as illustrated in Figure 5. 7.

Figure 5. 7 shows also that Atta Clay differs from Sudanese one also referring to the average initial degree of saturation, which results equal to about 90%. Samples start to de-saturate at lower value of suctions with respect to Black Cotton Clay.

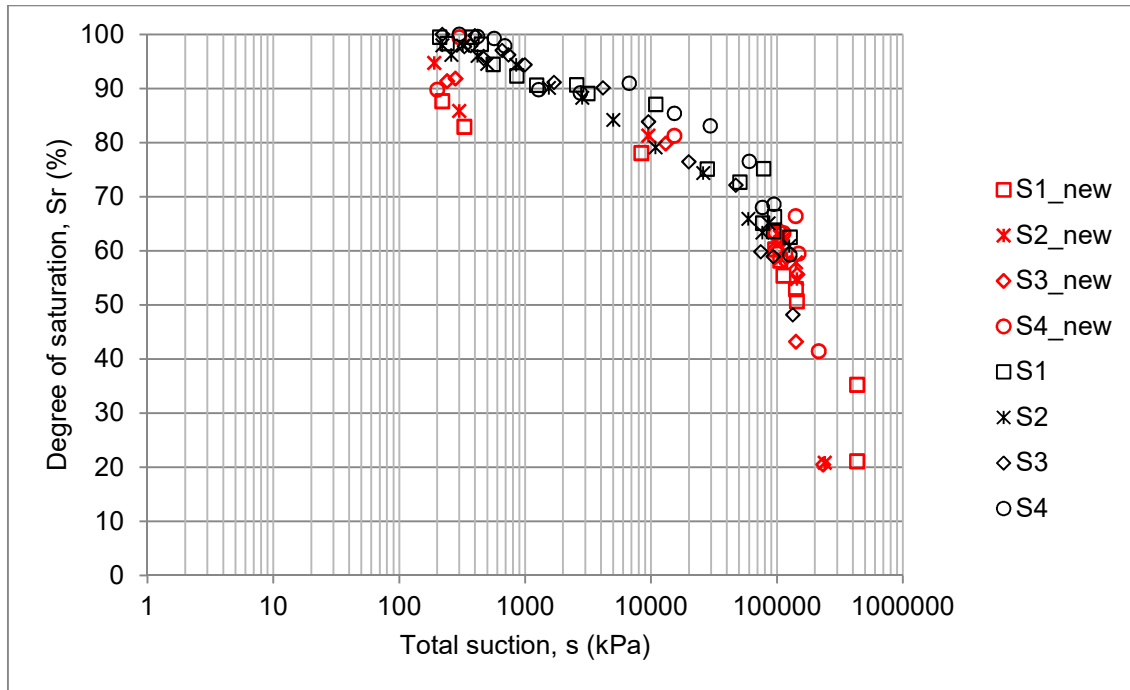


Figure 5. 7 – Atta clay SWRCs and comparison with previous results (after Abdalla *et al.*, 2019) in the degree of saturation-total suction plane

As regards volume changes (void ratio) as a function of gravimetric water content (Figure 5. 8), the saturation stage results smaller than Black Cotton Clay one, since shrinkage line follows the saturation line approximately up to  $w=60\%$  (rather than 38%). The overall volume change during saturation stage is equal to  $\Delta e = 3.05 - 1.6 = 1.45$ , while Sudanese one is  $\Delta e = 2.1 - 0.8 = 1.3$ . This result is directly linked to clay content (Bronswijk 1988), since soils with high clay content remain saturated over a wide range of water contents during desiccation (Abdalla *et al.*, 2019).

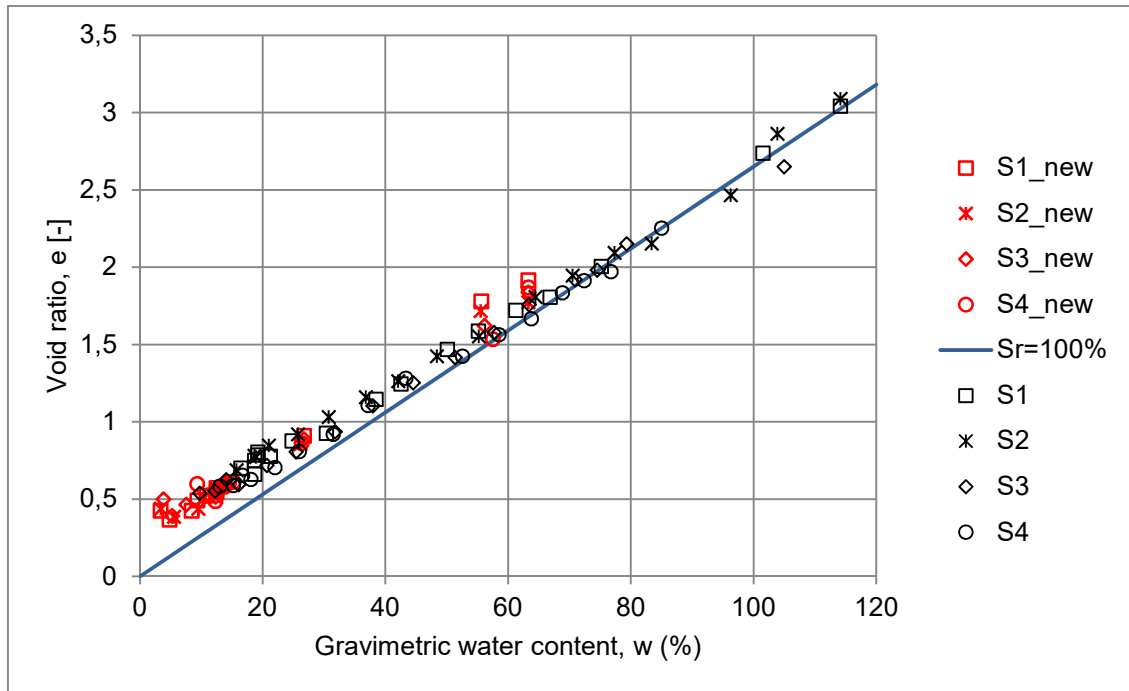


Figure 5. 8 – Atta clay shrinkage line and comparison with previous results (after Abdalla *et al.*, 2019) in the void ratio-gravimetric water content plane

In Figure 5. 9 PDC of SWRC is plotted in terms of void ratio- total suction. Atta clay shows an initial void ratio ( $e=3.05$ ) higher than Sudanese one ( $e=2.14$ ) and it decreases up to  $e=0.46$  (shrinkage limit) at the limit drying measurements. The same limit point is described in Figure 5. 10 by a value of gravimetric water content  $w=3.42\%$ .

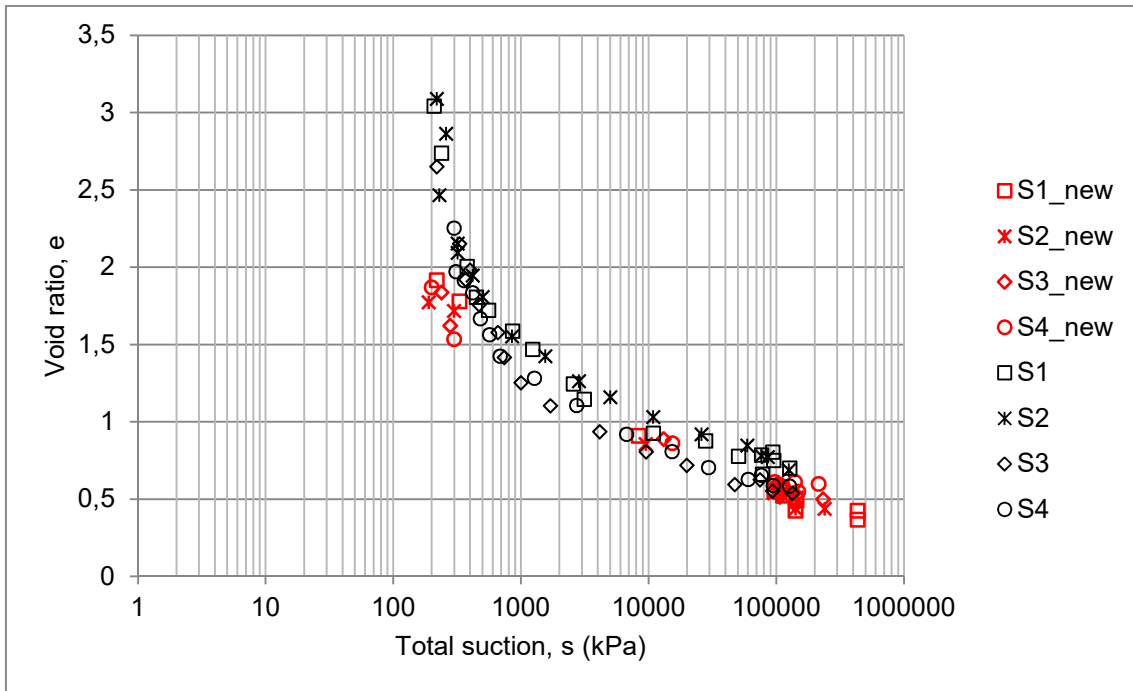


Figure 5.9 – Atta clay SWRCs and comparison with previous results (after Abdalla *et al.*, 2019) in the void ratio-total suction plane

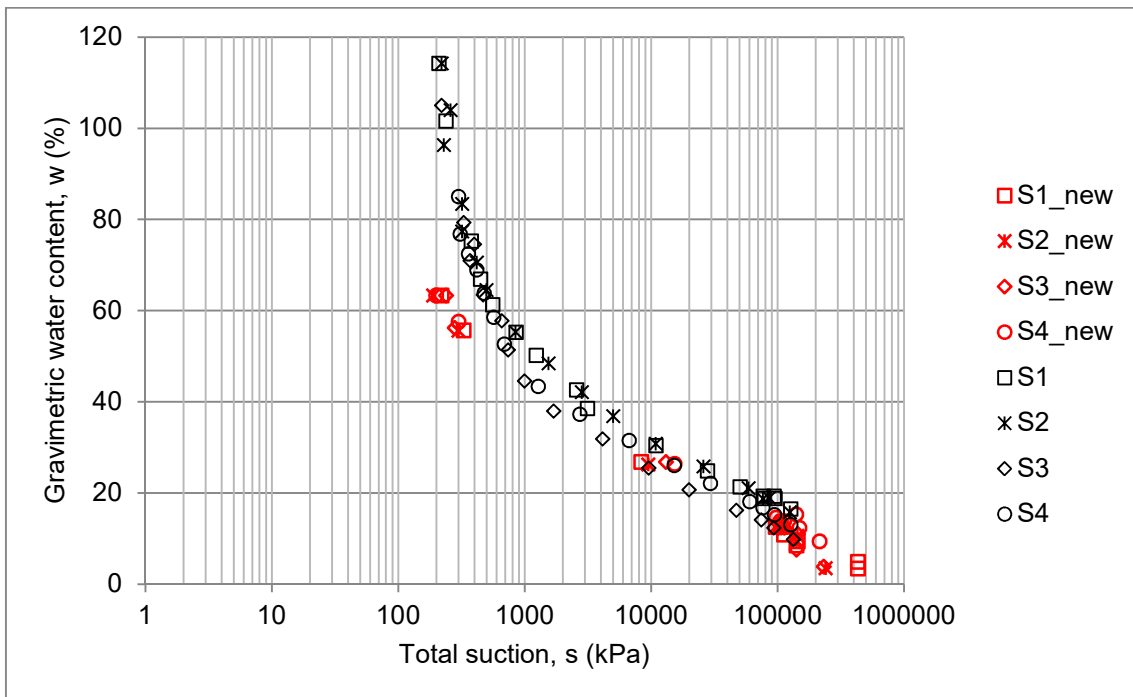


Figure 5.10 – Atta clay SWRCs and comparison with previous results (after Abdalla *et al.*, 2019) in the gravimetric water content-total suction plane

### 5.1.3 Best fitting Van Genuchten's retention curve

In the following section, Van Genuchten's curve of best fitting of experimental SWRCs is derived by applying the least squares method, in order to minimize the error between experimental and analytical points.

As described in section 2.6.2.1, parameters  $\alpha$  and  $n$  are estimated by using a numerical solver (Excel), on the basis of already measured retention curves (section 5.1.1 and 5.1.2) and existing analytical relationships between volumetric water content and suction.

First saturated volumetric water content  $\theta_s$  are derived for each sample as the maximum measured value, while residual ones  $\theta_r$  cannot be reached through common measuring systems, so it can be reasonably assumed equal to  $0.1 \cdot \theta_s$ . As a consequence,  $\theta_p$  can be computed according to equation (2.13), as listed in the following tables:

Table 5. 3 – Saturated, residual and average volumetric water contents of Black cotton and Atta clay samples

	Atta Clay			Black Cotton Clay		
	$\theta_s$ [%]	$\theta_r$ [%]	$\theta_p$ [%]	$\theta_s$ [%]	$\theta_r$ [%]	$\theta_p$ [%]
Sample 1	74,88	7,49	41,18	63,97	6,40	35,18
Sample 2	74,01	7,40	40,71	65,61	6,56	36,09
Sample 3	74,88	7,49	41,18	74,88	7,49	41,18
Sample 4	64,54	6,45	35,50	66,41	6,64	36,52

The slope of measured retention curves on a semi-logarithmic plane  $\frac{d\theta}{d(\log s)}$  is estimated through a linear regression of experimental points ( $\log(s); \theta$ ), separately for each sample. Once known the slope, four values  $S_p$  are computed according to equation (2.12) and four suction values  $s$  corresponding to  $\theta_p$  along the measured retention curve. Then, a numerical solver (Excel) allows to estimate  $m$  and  $\alpha$  parameters as shown in equations (2.11) and (2.14) respectively, by considering average values of computed slope  $S_p$  and suction  $s_p$ , in order to derive an unique fitting curve representing all four sample.

In Table 5. 4 parameters obtained for each SWRCs are listed together with average values of saturated and residual volumetric water content:

Table 5. 4 – Van Genuchten’s parameters of the best fitting retention curves in the volumetric water content-suction plane

	Atta Clay	Black Cotton Clay
m	0,230	0,250
n	1,299	1,333
$\alpha$ [kPa <sup>-1</sup> ]	0,00184	0,0016
$\theta_s$ [%]	74,88	74,88
$\theta_r$ [%]	6,45	6,40

Finally, Van Genuchten’s retention curves are plotted and compared with experimental results for both Atta Clay and Black Cotton clay SWRCs in a semi-logarithmic plane suction  $s$  [kPa]- volumetric water content  $\theta$  [%], as shown in Figure 5. 11 and Figure 5. 12.

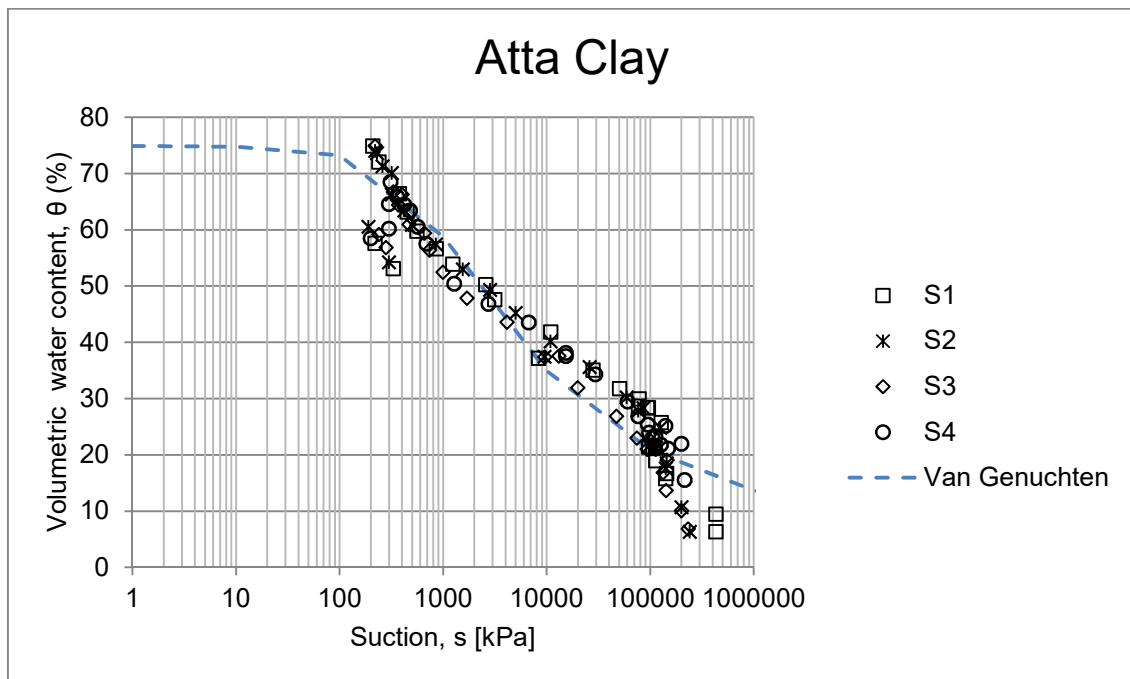


Figure 5. 11 – Van Genuchten’s retention curve and comparison with Atta Clay SWRC in the volumetric water content-suction plane

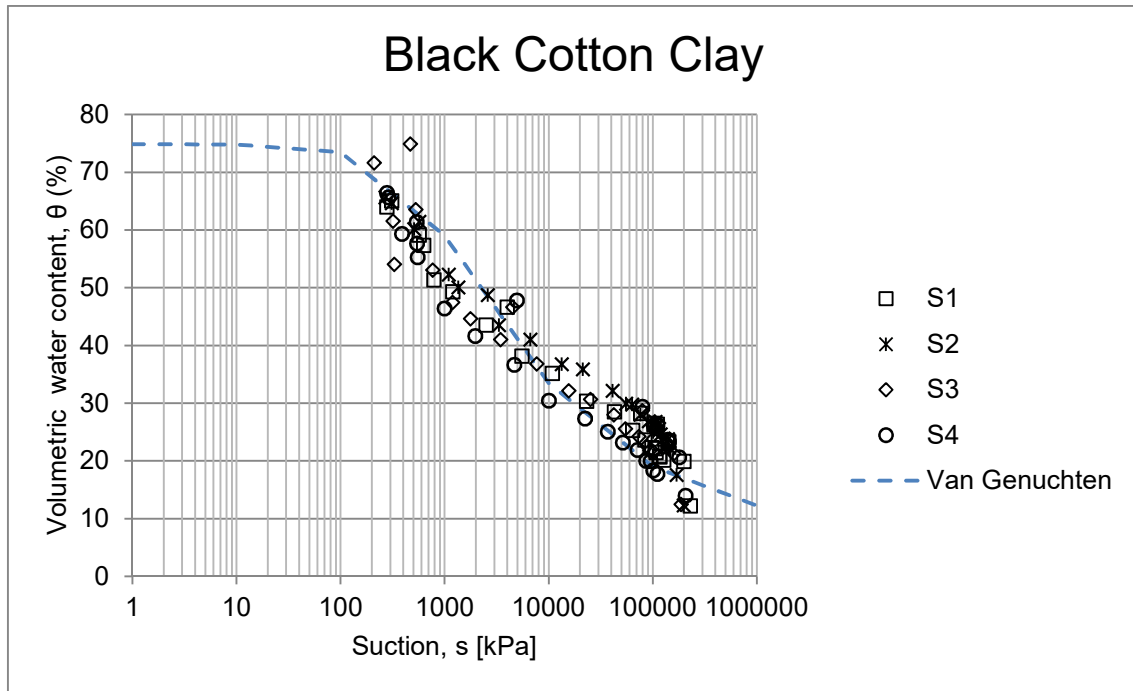


Figure 5.12 – Van Genuchten's retention curve and comparison with Black Cotton Clay SWRC in the volumetric water content-suction plane

In both cases plotted Van Genuchten's retention curve provides a good fitting of experimental points, so it follows that estimated parameters effectively represent the behaviour of tested materials in terms of soil-water retention curves.

Usually SWRCs are plotted in  $(S_r; s)$  plane, in order to graphically evaluate two main variables: air-entry value (AEV), which is directly correlated to  $\alpha$  parameter, and the residual degree of saturation ( $S_r$ ), corresponding to the minimum value of suction that can be reached through WP4C device ( $s = -300 \text{ MPa}$ ). Results are listed in Table 5.5.

Table 5.5 – Van Genuchten's parameters of the best fitting retention curves in the degree of saturation-suction plane

	Atta Clay	Black Cotton Clay
m	0,750	0,350
n	1,000	1,400
$\alpha$ [ $\text{kPa}^{-1}$ ]	0,00003	0,0001
AEV [kPa]	6000	5000
$S_{\text{residual}}$ [%]	20,47	38,07

Van Genuchten's retention curves are plotted and compared with experimental results for both Atta Clay and Black Cotton clay SWRCs in a semi-logarithmic plane suction  $s$  [kPa]- Degree of saturation  $S_r$  [%] (Figure 5. 13 and Figure 5. 14).

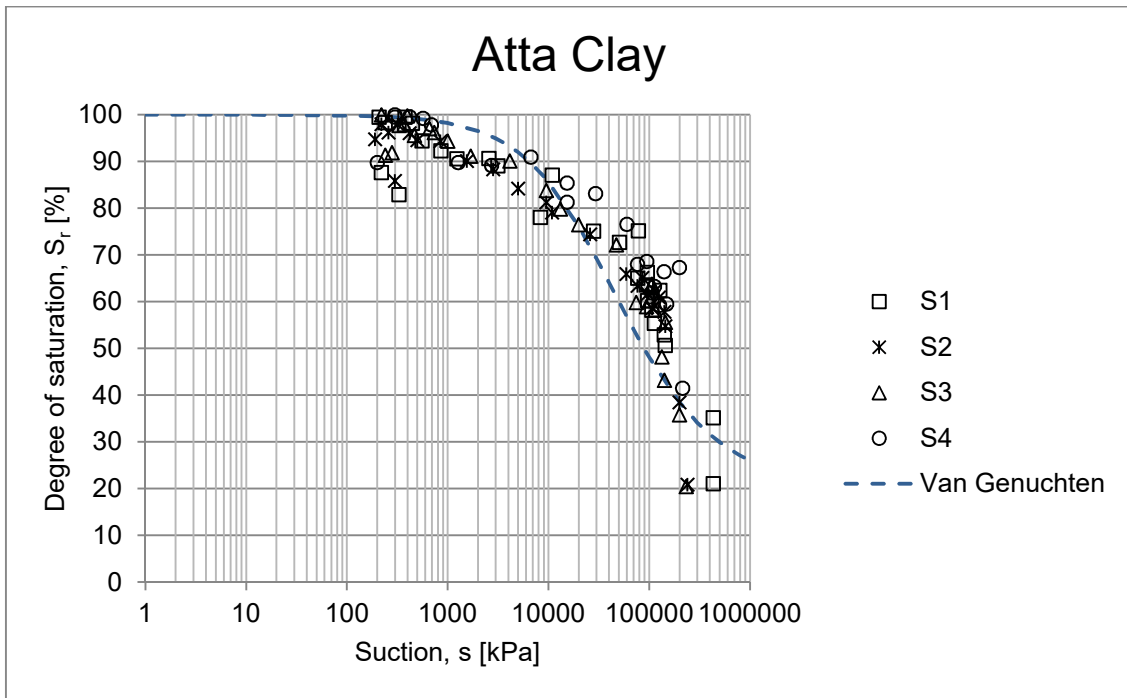


Figure 5. 13 – Van Genuchten's retention curve and comparison with Atta Clay SWRC in the degree of saturation-suction plane

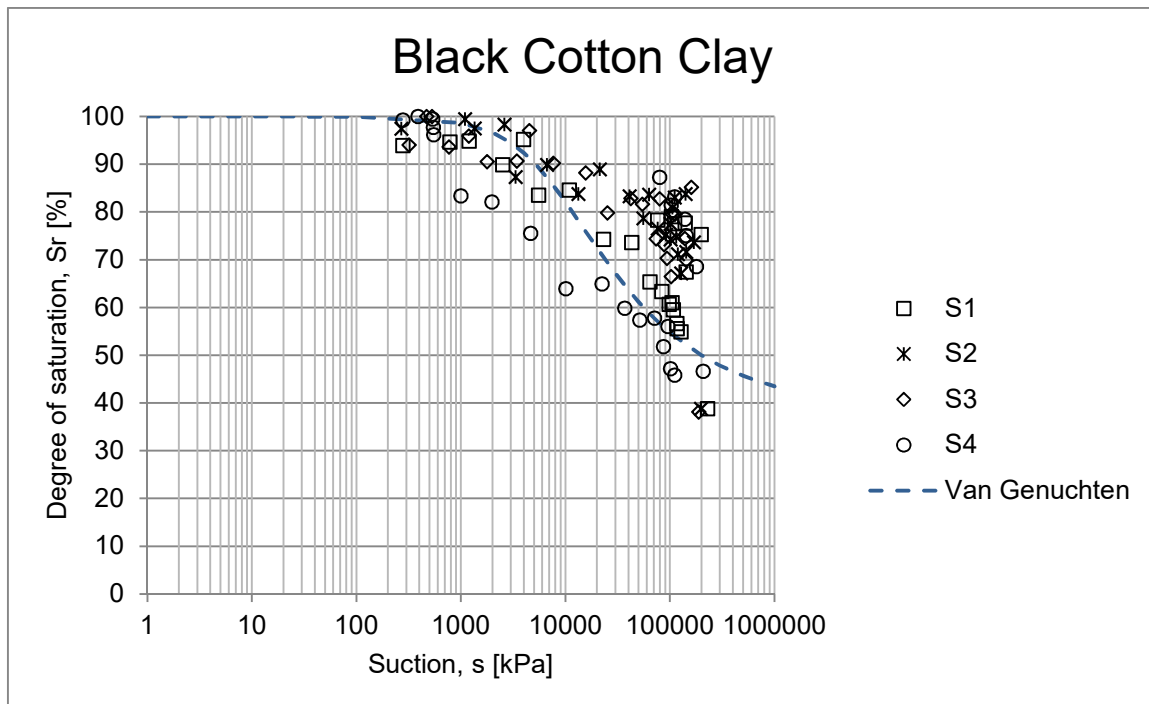


Figure 5. 14 – Van Genuchten’s retention curve and comparison with Black Cotton Clay SWRC in the degree of saturation-suction plane

### 5.3 RCTS apparatus

#### 5.2.1 Set-up of the saturated test

Once obtained a reconstituted 100 mm sample as showed in Figure 4. 19, the 38 mm sample is derived by means of a sample cutter with the same diameter. Then, the sample is placed on the porous disc, which is directly installed on the bottom base, and a membrane is placed through a membrane stretcher. O-rings allow to fix membrane to both bottom and top cap, as shown in Figure 5. 15(a).

Once ensured the adhesion between sample, membrane and bases, the pressure cell, the drive system and the measuring system are installed, obtaining the final test configuration shown in Figure 5. 15(b).

Pressure cell is then filled with de-aired water, whose level is equalized with respect to the reference burette one, to allow for volume change measurements through the DPT system.

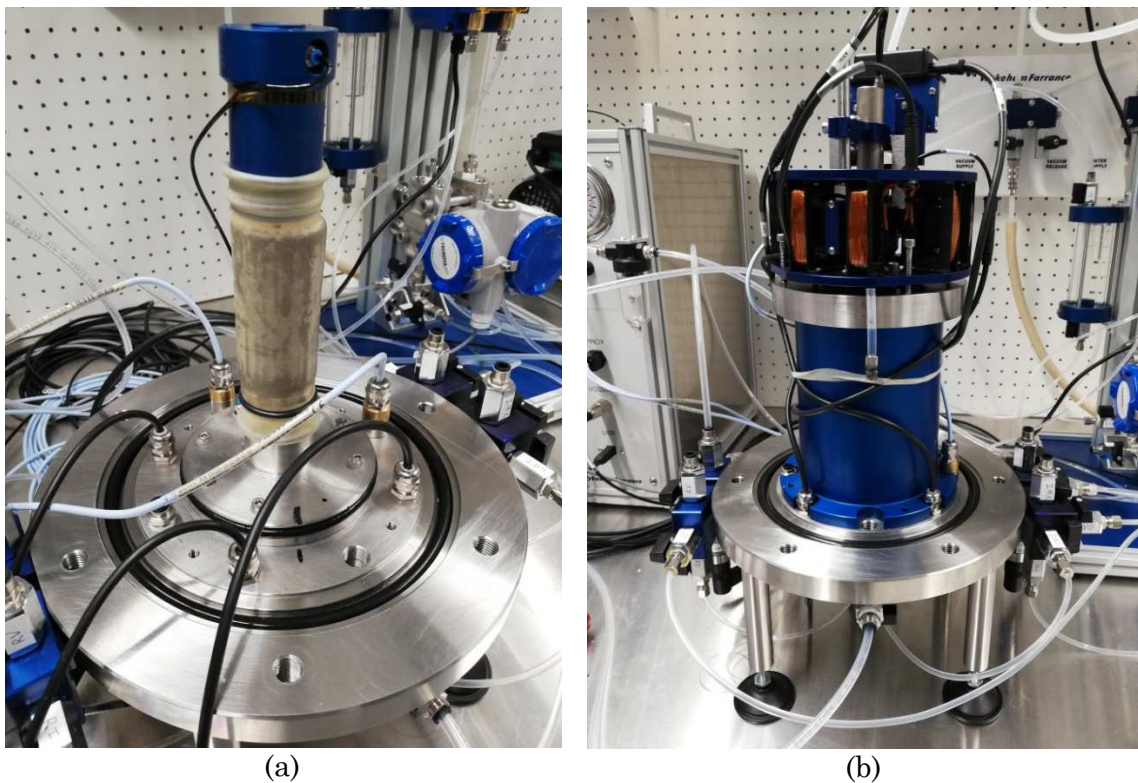


Figure 5. 15 –Placement of (a) sample, membrane and O-rings and (b) pressure cell, drive system and measurement sensors

Test results are strongly influenced by:

- a correct and solid fixing between pressure cell and base support, in order to guarantee the hypothesis of fixed-free configuration;
- a proper alignment of opposite pair of coils and magnets centrality with respect to each pair of coils, which is required by the specific loading condition;
- a full saturation of all water circuits and HAEV porous stone.

Finally, external cylinder is placed and steel bars are properly fixed to allow for compressed air supplying.

Once opened the compressed air supply system, cell pressure is increased up to 100 kPa, without applying any backpressure, in order to check the saturation of the sample by means of a B-test. According to Skempton's theory, B value is defined as

$$B = \frac{\Delta u}{\Delta p} \quad (5.1)$$

and the sample can be assumed as saturated if B results close to 1, which means that each increment in cell pressure corresponds to the same increment in terms of pore-water pressure.

From the test B-values equal to 0.96 to 0.98 are obtained, which allows for assuming saturated condition.

### 5.2.2 Saturated test ( $p' = 50$ kPa) – Consolidation phase

The following step involves the creation of a new project, by specifying the project name, comments and specimen height, diameter and weight, in the “Loaded project” window, showed in the Figure 5. 16. In Table 5. 6 initial geometric and physical properties of tested specimen are listed:

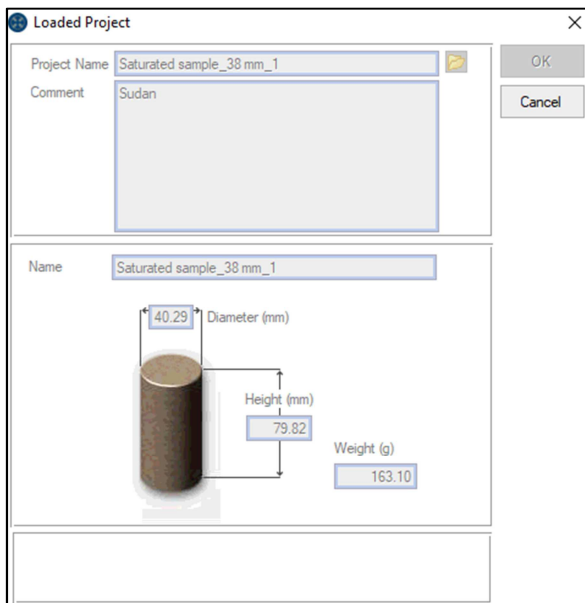


Table 5. 6 – Initial geometric and physical properties of tested sample

Diameter [cm]	4,03
Height [cm]	7,98
Weight [g]	163,1
$w_0$ [%]	70
$e$ [-]	1,80
$G_s$ [-]	2,54
$S_r$ [%]	98,6

Figure 5. 16 – Loaded project window

The saturated sample, reconstituted in a consolidometer at a nominal stress level equal to 100 kPa, is isotropically consolidated at an effective stress of 50 kPa, obtained by applying a cell pressure equal to 150 kPa and a backpressure equal to 100 kPa.

In order to estimate the time required to reach the 95% of the consolidation process, Terzaghi's 1D consolidation theory can be used. Proper values of consolidation parameters (permeability coefficient  $k$ , vertical consolidation coefficient  $c_v$  and volume compressibility coefficient  $m_v$ ) can be selected as a function of vertical effective stress from Figure 5. 17, derived by a previous study on Black Cotton clay (Al Haj, K., 2014).

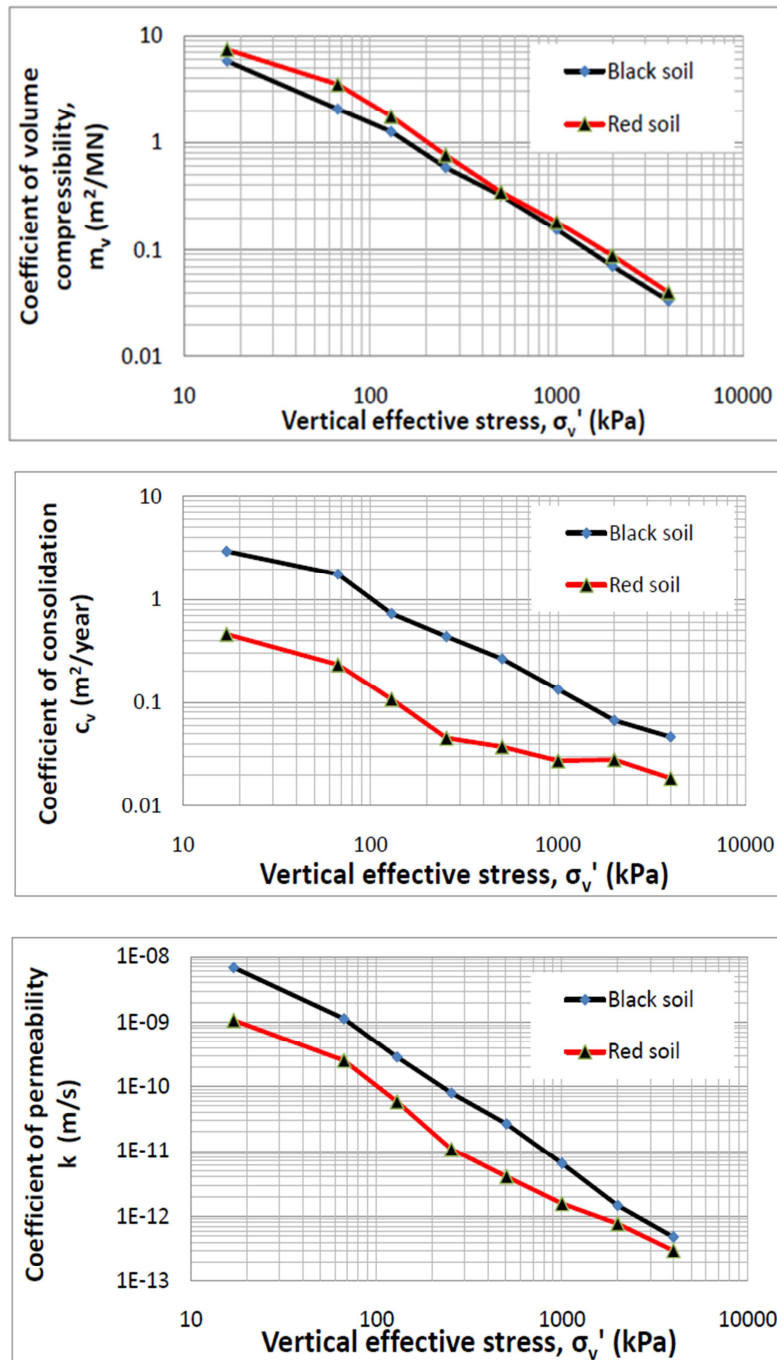


Figure 5. 17 – Consolidation parameters curves as a function of vertical stress from a previous study on two tropical clays (after Al Haj, K., 2014).

In Table 5. 7 consolidation parameters corresponding to a vertical effective stress of 50 kPa are listed:

Table 5. 7 – Consolidation parameters of Black Cotton clay reconstituted samples

$m_v$ [m <sup>2</sup> /MN]	2,5
$c_v$ [m <sup>2</sup> /year]	2
$k$ [m/s]	2,00E-09

By applying Terzaghi's 1D consolidation theory to the saturated specimen with a height  $H = 7,982 \text{ cm}$ , a vertical consolidation coefficient  $c_v = 6,34E - 4 \frac{\text{cm}^2}{\text{s}}$ , the time required to reach a percentage of the overall consolidation equal to 95% can be estimated as follow:

$$t_{95} [\text{s}] = \frac{H^2 \cdot T_{95}}{c_v} = 1 \text{ day} \quad (5.2)$$

where  $T_{95}$  is the time factor corresponding to an average consolidation degree of 95%.

Once known the coefficient of volume compressibility  $m_v$  (Table 5. 7), the overall volume strain during the consolidation process can be computed according to the equation:

$$\frac{\Delta V}{V} = \Delta \sigma'_v \cdot m_v = 0,075 \quad (5.3)$$

By considering initial volume  $V$  and porosity  $n$  under saturated condition, the estimated total amount of water flowing out during consolidation phase results equal to

$$\Delta V_{\text{water}} = 4,84 \text{ cm}^3 \quad (5.4)$$

On the other hand, the effective amount of water flowing out from the porous stone is measured through the volume gauge (water content) and it is plotted against time in logarithmic scale. The resulting consolidation curve is showed in Figure 5. 18.

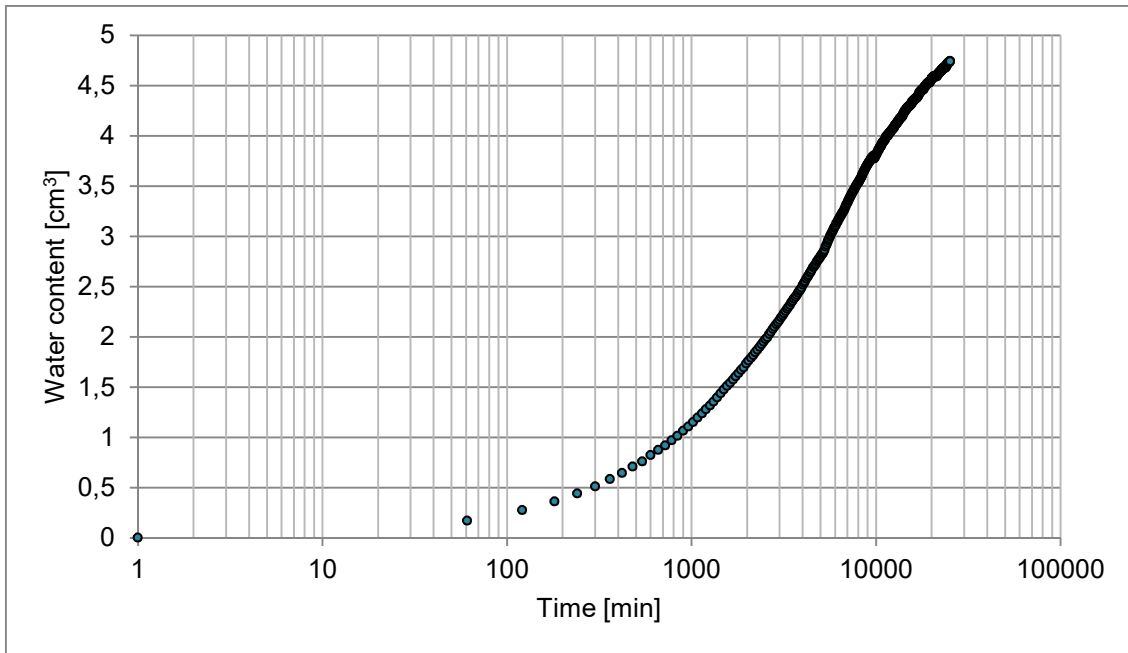


Figure 5. 18 – Consolidation curve of tested reconstituted sample

By comparing the estimated consolidation time and the corresponding volume changes with measured quantities, it results that the prediction related to the amount of water is roughly correct, but the effective consolidation time is significantly higher

In order to estimate consolidation time required to reach a consolidation degree equal to 90%, Taylor's consolidation theory is graphically applied. It requires to plot on y-axis specimen height variation while on x-axis the square root of time, as showed in Figure 5. 19. Up to an average consolidation degree approximately equal to 60% the curve follows a linear path, which can be linearly interpolated. The slope of resulting interpolation line is then increased by 15% in order to get the dotted red line, which intersects the curve in the point  $(\sqrt{t_{90}}; H_{90})$ .

Time required to get 90% of consolidation process results  $t_{90} \approx 12 \text{ days}$ , which is significantly higher than estimated one (1 day).

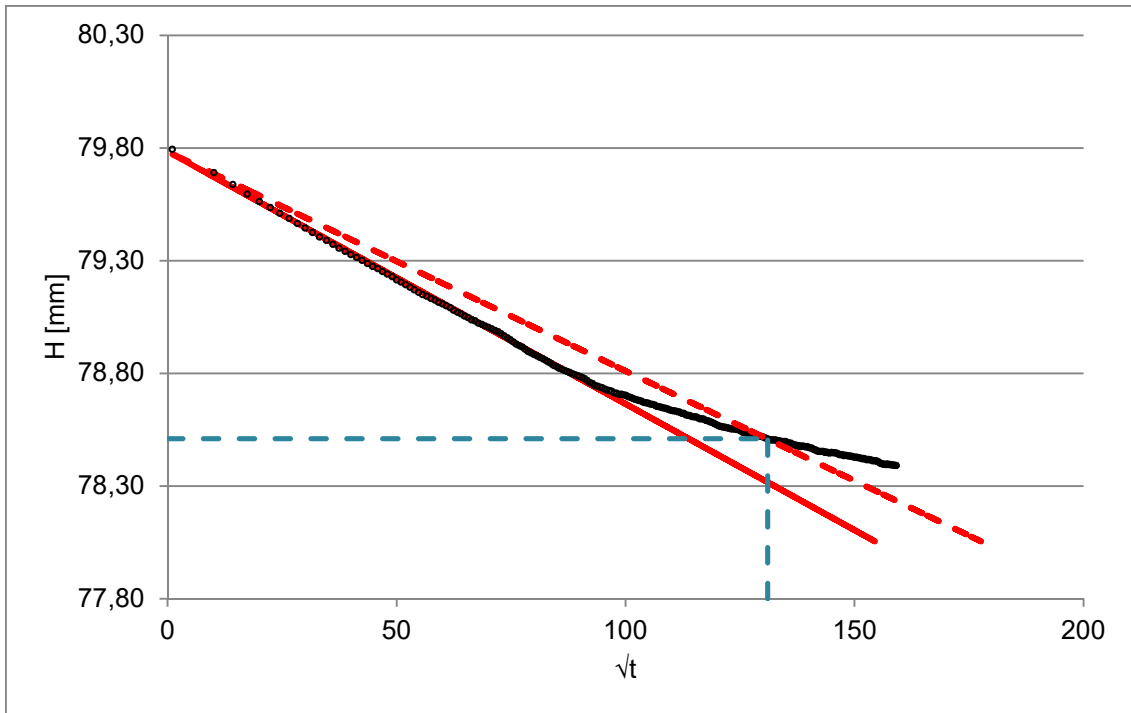


Figure 5. 19 – Graphical evaluation of consolidation time according to Taylor's consolidation theory

On the basis of previous results, in Figure 5. 20 the same consolidation curve showed in Figure 5. 18 is plotted in terms of the average degree of dissipation against time, in order to compare it with curves obtained by a previous study (Al Haj, K., 2014) on samples 76 mm thickness with different values of coefficient of consolidation (Figure 5. 21).

It follows that the effective value of  $c_v$  might belong to the range  $\left[0,01 \div 0,1 \frac{m^2}{year}\right]$ .

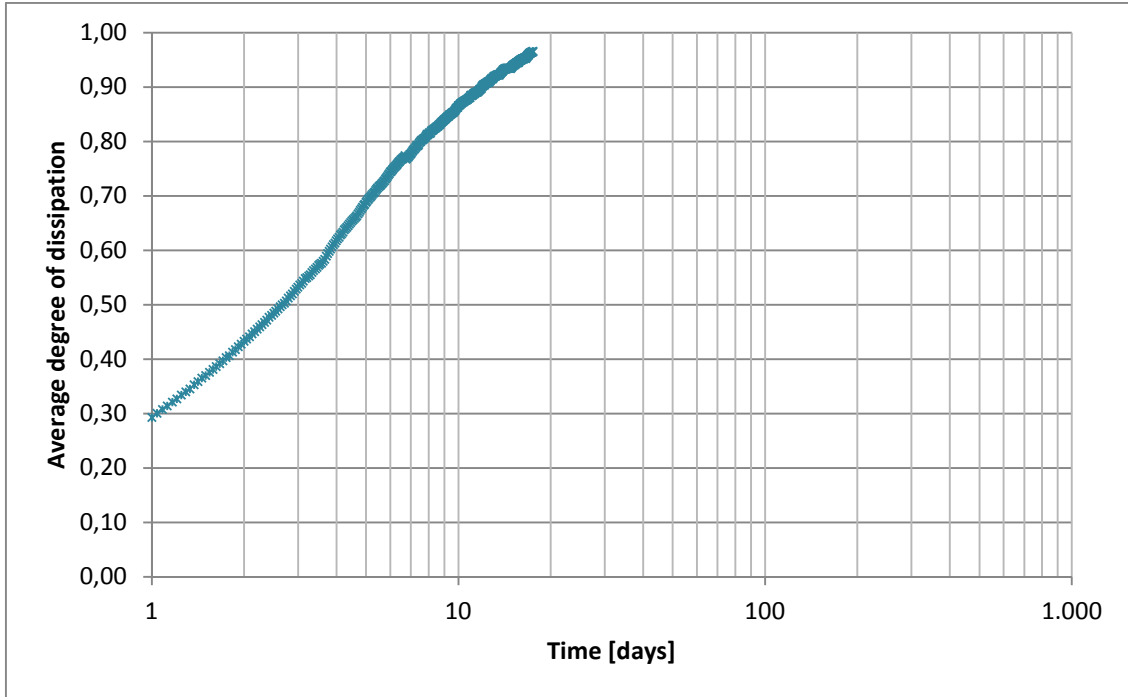


Figure 5. 20 – Consolidation curve plotted in the average degree of dissipation-time plane

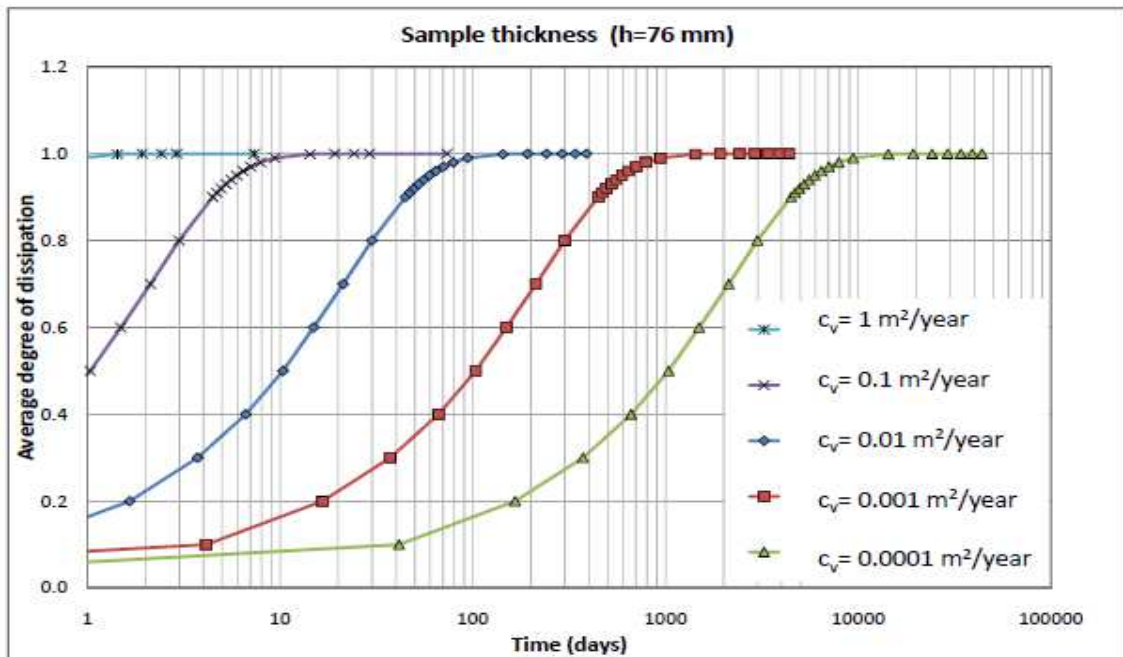


Figure 5. 21 – Influence of the coefficient of consolidation on the average degree of dissipation-time curve for a sample thickness equal to 76 mm (after Al Haj, K., 2014)

In order to identify reasons of the difference between estimated and measured consolidation time, an evaluation of the effective material permeability is obtained through a back analysis process, by requiring that an average consolidation degree of 90% is reached in 12 days, as measured.

Once known  $t_{90}$  [s] through Taylor's theory, the corresponding coefficient of consolidation is computed by applying Terzaghi's 1D consolidation theory as follow:

$$c_v = \frac{H^2 \cdot T_{90}}{t_{90}} = 4,51E - 4 \frac{cm^2}{s} \quad (5.5)$$

In the same way the final water content variation ( $\Delta w = 4,438 \text{ cm}^3$ ), measured through the volume gauge, allows to compute the effective coefficient of volume compressibility:

$$m_V = \frac{\Delta V_W}{V_{w0} \cdot \Delta \sigma'_v} = 2,26E - 3 \frac{m^2}{kN} \quad (5.6)$$

By equalizing the equation (5.5) with the definition of  $c_v = \frac{k}{m_V \cdot \gamma_w}$  as a function of the effective coefficient of permeability  $k$ , it results

$$k_{eff} = 1.15E - 10 \frac{m}{s} \quad (5.7)$$

Effective coefficient of permeability  $k_{eff}$  is one order of magnitude lower than the theoretical one (Table 5. 7). A comparison between  $k_{eff}$  and results of permeability test performed on the porous disc (Chapter 4.3.5) shows a correspondence of the two values, which leads to identify the reason of such long consolidation time in a lack of full saturation of the porous stone.

By considering these results it follows the decision of performing RC and TS tests at a degree of consolidation equal to 90% and, then, proceeding with a second saturation phase of the porous disc through a different technique with respect to the one described in the chapter 4.3.5. In order to allow residual air bubbles going out from inner pores, the porous disc is immersed in a reservoir filled with demineralized water and then put under vacuum. Flow rate through porous stone and the corresponding hydraulic conductivity are evaluated by applying a filtration motion, as described in the chapter 4.3.6.

### 5.2.3 Saturated test ( $p' = 50$ kPa) – Cyclic loading phase

In order to investigate a proper frequency range in RC test, a theoretical resonance frequency can be estimated by referring to empirical correlations, provided in literature.

Among different theoretical models listed in chapter 2.8.1, the one proposed by Viggiani and Atkinson (1995) can be used to get an estimation of the maximum shear modulus  $G_0$ , according to the following equation:

$$\frac{G_0}{p_{ref}} = A \left( \frac{p'}{p_{ref}} \right)^n OCR^m \quad (5.8)$$

where  $p'$  is the applied mean effective stress, OCR is the over consolidation ratio and  $A$ ,  $m$  and  $n$  are material parameters related to the plasticity index PI and evaluated through specific graphs.

In Table 5. 8 input parameters of tested sample are listed:

Table 5. 8 – Initial sample properties and input parameters

$p'$ [kPa]	50
$p_{ref}$ [kPa]	1
OCR [-]	2
PI=50	
A	250
m	0,26
n	0,83

By substituting listed values in the equation (5.8), the maximum shear modulus results equal to

$$G_0 = 7697,56 \text{ kPa} \approx 7,70 \text{ MPa} \quad (5.9)$$

Through the common relationship  $G = \rho V_s^2$  the shear wave propagation velocity  $V_s$  can be derived, once known the value of soil density as directly computed by the software ( $\rho = 1437 \frac{kg}{m^3}$ ):

$$V_s = 73,19 \text{ m/s} \quad (5.10)$$

If the drive system was massless ( $I_0 = 0$ ), the implicit equation used to interpret RC results (5.6) would degrade to

$$V_s = \frac{2\omega_n H}{\pi} = 4f_n H \rightarrow f_{res} = \frac{V_s}{4H} \quad (5.11)$$

which is commonly used to evaluate the fundamental frequency under linear elastic soil behaviour. In this case the rotations would follow a quarter-sine-wave pattern over the height of the specimen at the fundamental frequency.

Adding the mass of the drive system results in a more linear variation of rotation and, as a consequence, more uniform strain conditions over the height of the specimen. Hence, the shear-wave velocity  $V_s$  can be evaluated by solving the implicit equation (5.6) under the following conditions (Table 5. 9), in terms of sample and drive system inertia (after consolidation):

Table 5. 9 – Sample and drive system mass polar moment of inertia

Drive system mass polar moment of inertia	$I_t [kgm^2]$	1,52E-03
Specimen mass polar moment of inertia	$I_p [kgm^2]$	3,31E-05
Specimen height	$H [mm]$	79,82

Among the infinite values of  $\beta$ , the one which satisfied the implicit equation is equal to

$$\beta = 0,147 \quad (5.12)$$

which corresponds to a resonance frequency

$$f_{res} = \frac{\beta V_s}{2\pi H} = 21,91 \text{ Hz} \quad (5.13)$$

As a consequence, a range of [10 ÷ 30 Hz] has been chosen for the RC frequency sweep.

RCTS tests and the following analysis of results has been carried out through a software developed by the same designer of RCTS apparatus. All types of test require the definition of input parameters to specify specimen initial geometrical characteristics and loading technique.

Once the consolidation phase is completed, all drainage circuits are closed and cyclic loading phase starts.

### Resonant Column Test

In Figure 5. 22 software window referred to RC test is showed. On the left side, all input parameters describing the frequency sweep are listed, in terms of initial and final frequency, duration and amplitude. As previously specified, frequency range has been chosen as  $[10 \div 30 \text{ Hz}]$ , on the basis of empirical correlations, while the amplitude of input motion is chosen small enough to investigate small strains behaviour in terms of initial shear modulus  $G_0$  and initial damping ratio  $D_0$ . The accelerometer appears the proper acquisition channel for RC test due to high frequency investigated range.

RC test results are given numerically on the left lower side, in terms of amplitude of fundamental frequency  $f_r[\text{Hz}]$ , shear modulus  $G [\text{MPa}]$ , shear strain  $\gamma [\%]$ , bandwidth amplitude frequencies  $f_1 \div f_2 [\text{Hz}]$  (green line), damping  $D [\%]$  and decay factor  $\zeta [-]$ , and graphically. Especially two different output graphs are plotted: the upper one shows the accelerometer response as a function of time, related to head sample rotation expressed in terms of angle [mrad]. The lower graph illustrates Fast Fourier Transform (FFT) of the amplitude response signal as a function of frequency and it allows for the identification of resonance frequency, which is that value corresponding to the maximum amplitude response (blue line).

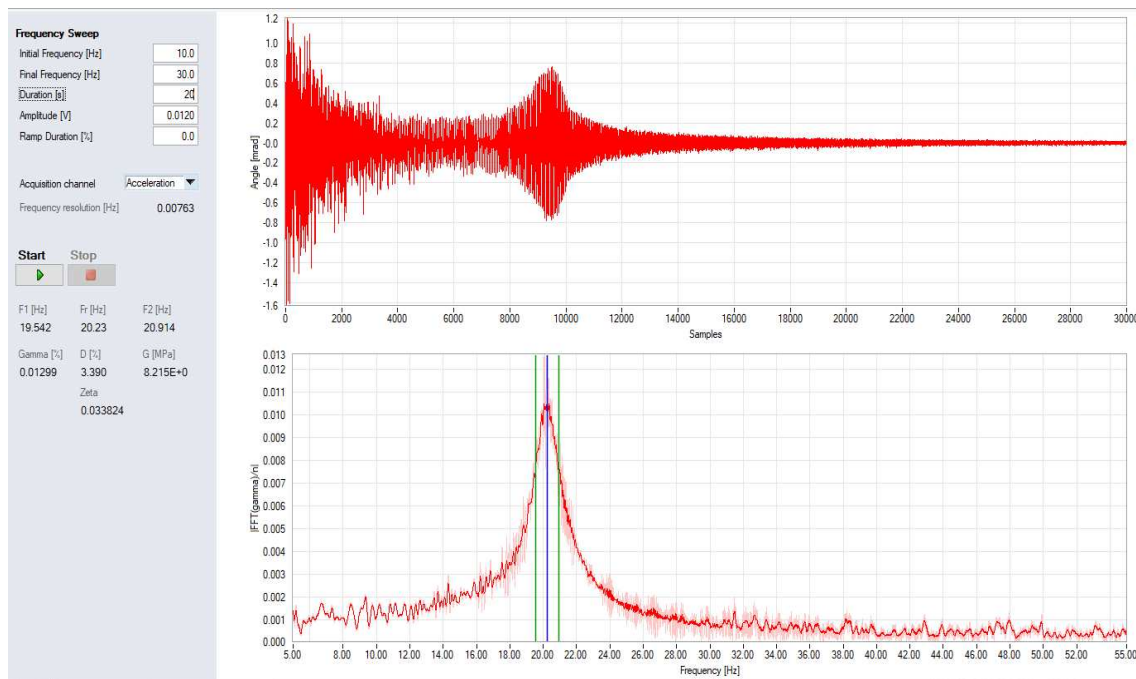


Figure 5. 22 – RC test control window: input parameters, accelerometer response and FFT of the amplitude response signal

### Torsional Shear Test

In order to get both shear modulus and damping degradation curves, TS tests are carried out by using the same RCTS apparatus. Torque is applied on sample head with the same technique of RC test, except for the input motion frequency, which remains constant at the set value, while the amplitude progressively increases. For each applied loading amplitude it is possible to define the relative hysteretic cycle in the plane  $\gamma - \tau$ , by means of measurements of sample head rotations through two proximity sensors (low frequency range).

In the same way as RC test, TS test setting up involves the definition of sampling parameters and waveform applied on the specimen. According to previous considerations, frequency is fixed equal to 2 Hz, significantly lower than the fundamental one, the number of cycles equal to 9, while amplitude increases in the range of  $[0,012 \div 3] V$ , which corresponds to a shear strains range of  $[9,40E - 3 \div 1,36] \%$ , as shown in Table 5. 9.

Table 5. 10 – Amplitude and corresponding shear strain level for each TS test

	A [V]	$\gamma$ [%]
1	0,012	2,51E-05
2	0,05	1,25E-05
3	0,08	2,51E-05
4	0,09	1,00E-04
5	0,1	5,27E-04
6	0,2	6,52E-04
7	0,3	1,40E-03
8	0,4	1,91E-03
9	0,5	2,03E-03
10	0,6	5,17E-03
11	0,7	5,54E-03
12	0,8	6,17E-03
13	0,9	1,09E-02
14	1	5,27E-02
15	2	3,98E-01
16	3	5,24E-01

In Figure 5. 23 results of one of the 16 carried out TS tests are illustrated, in terms of excitation-time (Green) and response-time (red) curves and 9 hysteresis cycles in the plane  $\gamma - \tau$ . Besides, in the table are listed the total shear strain  $\gamma_{pp}[\%]$ , resulting shear modulus  $G_{max} [MPa]$  and damping  $D$  [%] for each cycle and as average final quantities.

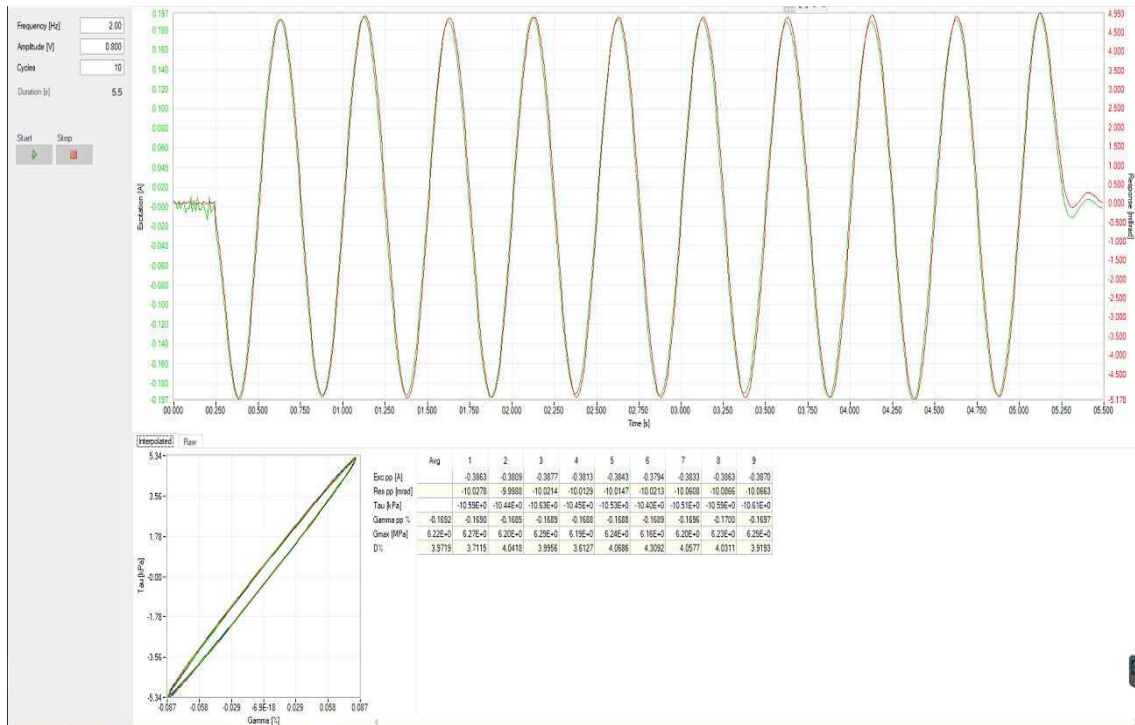


Figure 5.23 – TS test control window: input parameters, excitation-time and response-time curves and hysteresis cycles

## Decay Test

Finally, one decay Test has been carried out to estimate material damping through the 'logarithmic decay' method. In this case input parameters are divided into two main groups: stimulus and free decay, as listed in the left side of the following window. As regards the first category, they refer to the initial phase of torsional loading and involve excitation frequency and amplitude, assumed equal to RC test values, and number of loading cycles (15). Free decay parameters are duration of acquisition (3 seconds) and number of peaks for the decay factor calculation (10 peaks), on which the decay exponential curve is traced.

In Figure 5.24 two graphs are showed, the upper one represents amplitude response [mrad] with respect to the number of samples, while the bottom one illustrates a linear interpolation of the natural logarithmic of the 10 peak amplitudes, according to the procedure described in chapter 4.3.2.2.

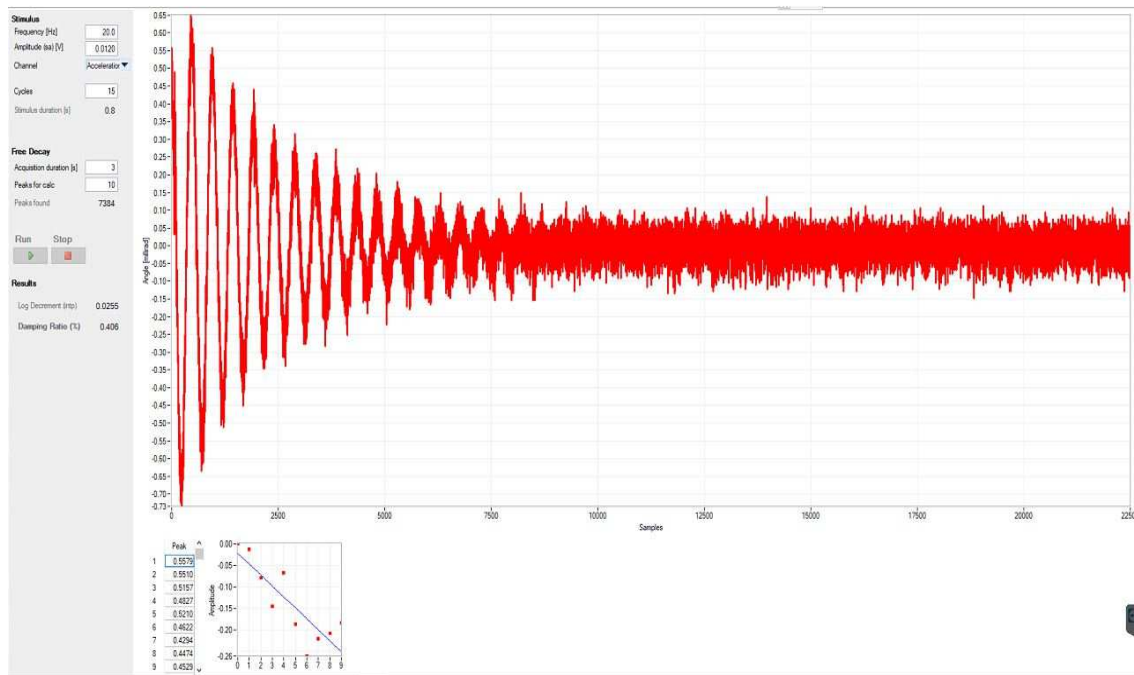


Figure 5. 24 – DECAF test control window: input parameters, free-decay amplitude response and logarithmic amplitude method for the evaluation of damping ratio

Specimen final geometrical and physical characteristics are listed in Table 5. 11 and showed in Figure 5. 25:



Figure 5. 25 – Sample condition after RCTS tests

Table 5. 11- Final geometric and physical properties of tested sample

Diameter [cm]	4,03
Height [cm]	7,92
Weight [g]	158,36
$w_r$ [%]	64,46
$e$ [-]	1,80
$G_s$ [-]	2,54
$S_r$ [%]	90,76

## 6. Interpretation of results

In the following section results of TS tests are showed, in terms of normalized shear modulus ( $\frac{G}{G_0}$ ) and damping ratio (D) degradation curves with respect to strain level, which varies in the range  $[2,51E - 05 \div 5,24E - 01]$  % (Figure 6. 1 and Figure 6. 2).

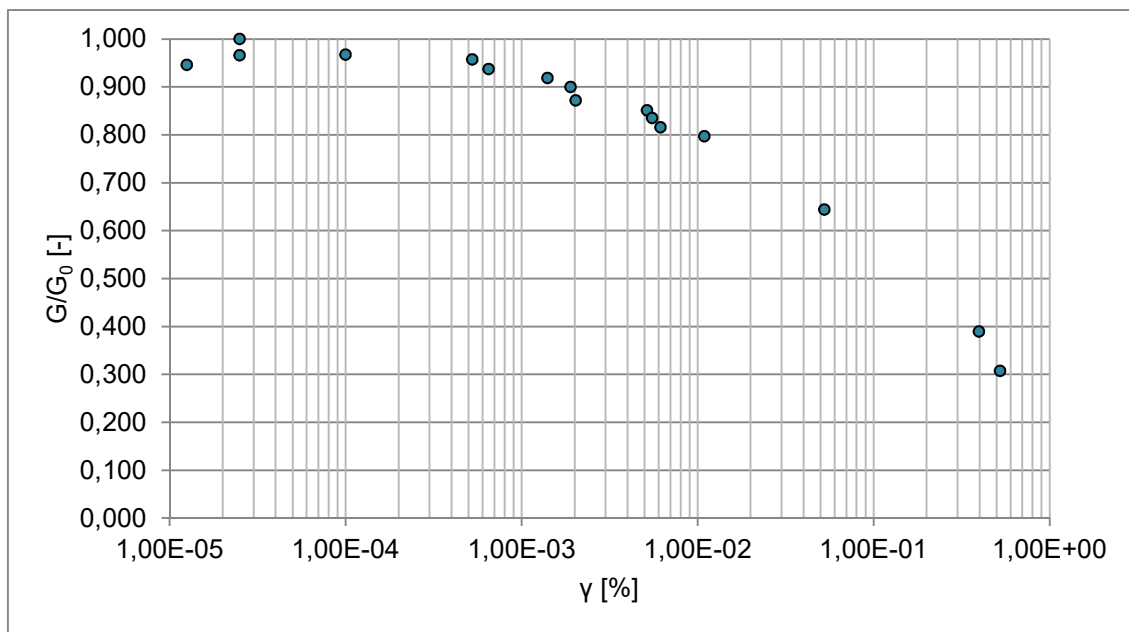


Figure 6. 1 – Normalized shear modulus degradation curve as strain level increases

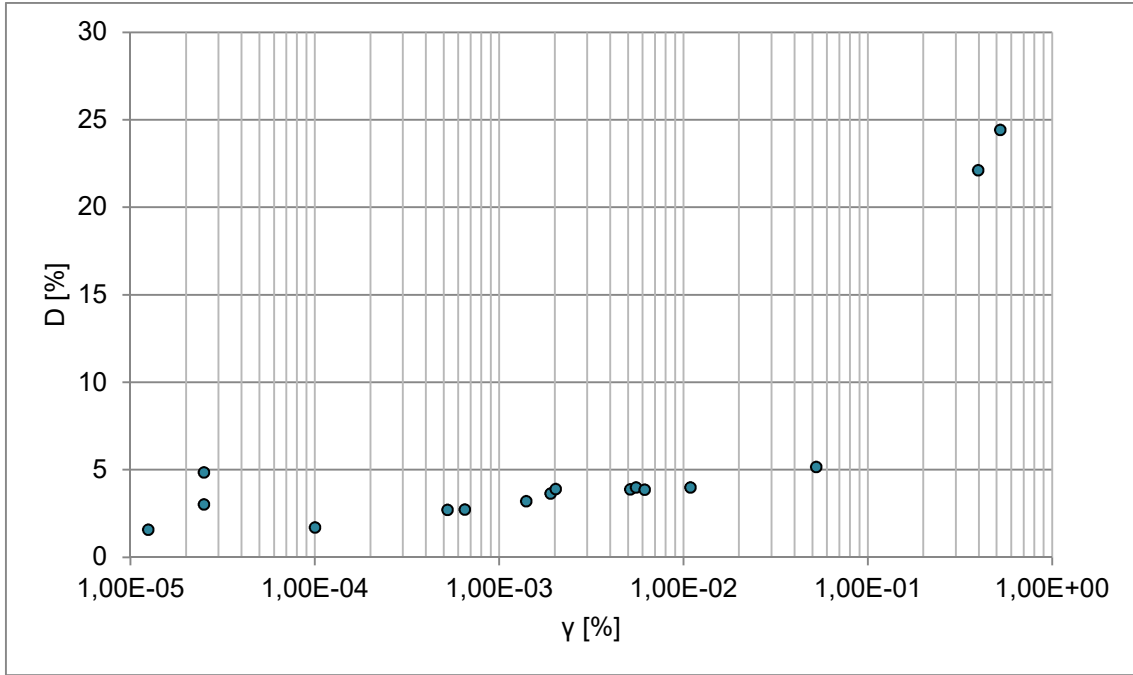


Figure 6. 2 – Damping ratio trend as strain level increases

According to degradation curves, tested Black Cotton Clay (PI=57) has a linear elastic threshold equal to  $\gamma_L \sim 1,00E - 3$  %, above which soil still behaves as an viscous-elastic material, but non-linearity appears. This value is in agreement with empirical correlations (Darendeli, 2001) between trends of degradation curves and plasticity index (Figure 6. 3).

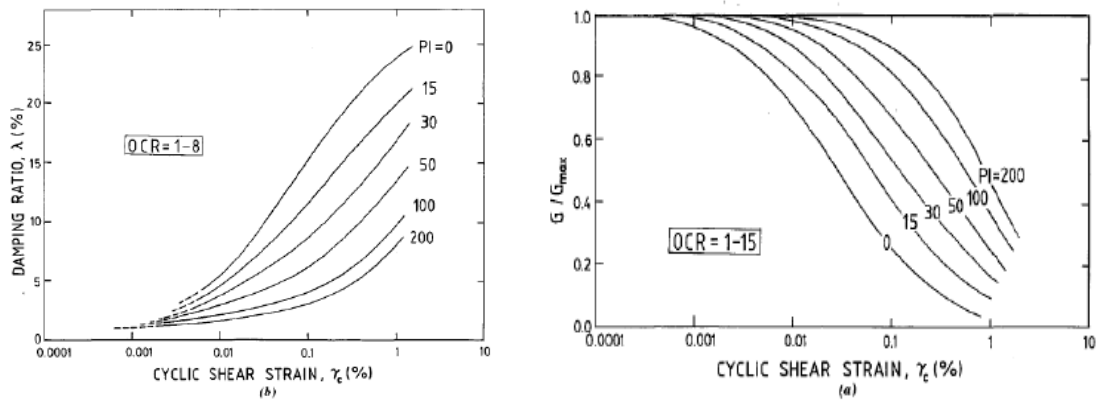


Figure 6. 3 – Influence of OCR and plasticity index on normalized shear modulus and damping ratio degradation curves (after Darendeli, 2001)

Figure 6. 4 and Figure 6. 5 illustrates shear modulus and damping ratio trends with respect to the number of cycles during TS tests. Damping ratio shows a decreasing pattern from low to high loading cycles, while shear modulus presents an approximately constant trend.

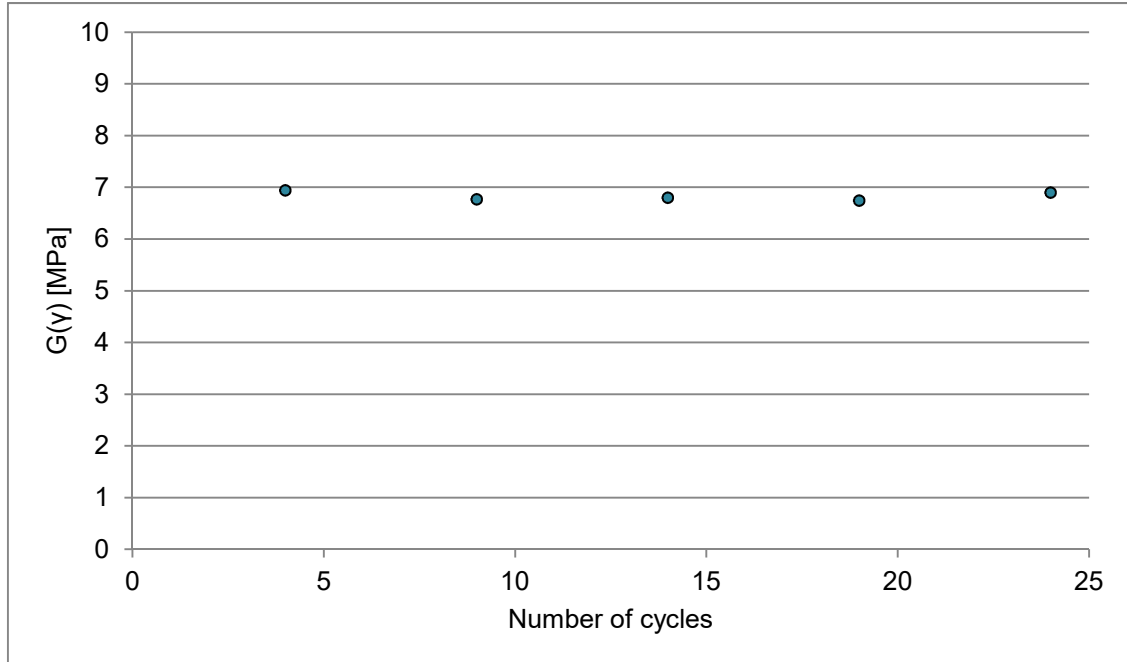


Figure 6. 4 – Influence of the number of cycles on shear modulus during TS tests

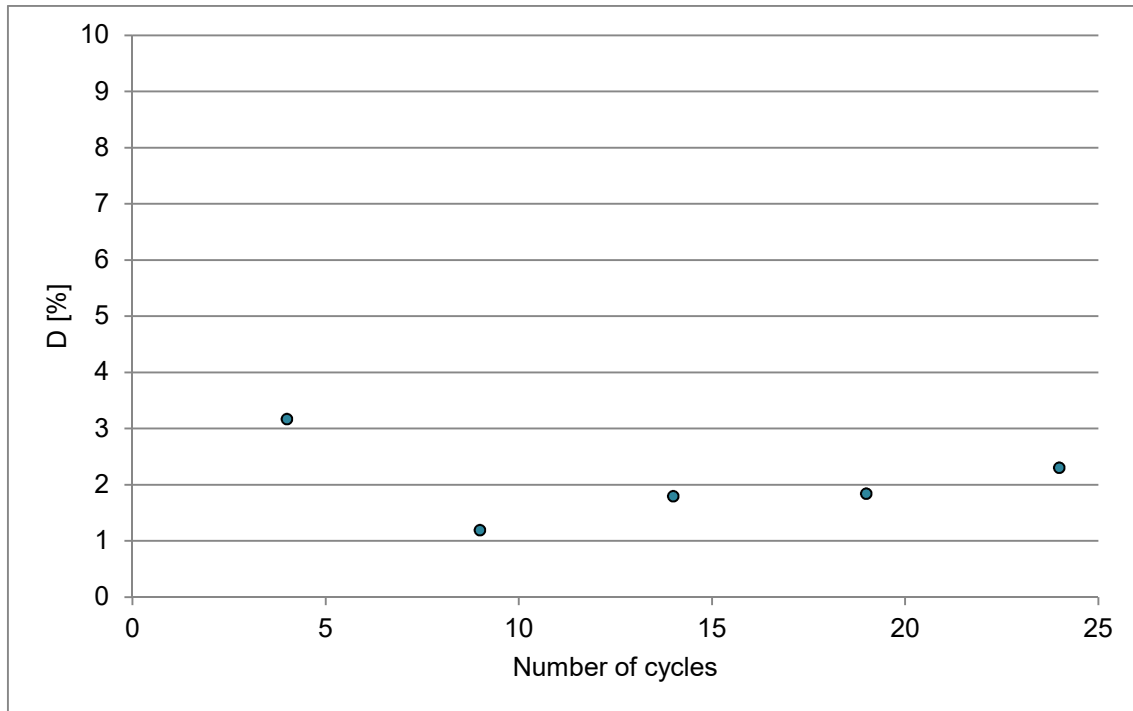


Figure 6. 5 – Influence of number of cycles on damping ratio during TS tests

Figure 6. 6 shows a comparison between RC and TS tests in terms of shear modulus with respect to strain levels. It results that RC test slightly overestimates soil shear stiffness with respect to Torsional Shear values. As a consequence, TS test provides a safer mechanical characterisation and it also refers to a wider strain range.

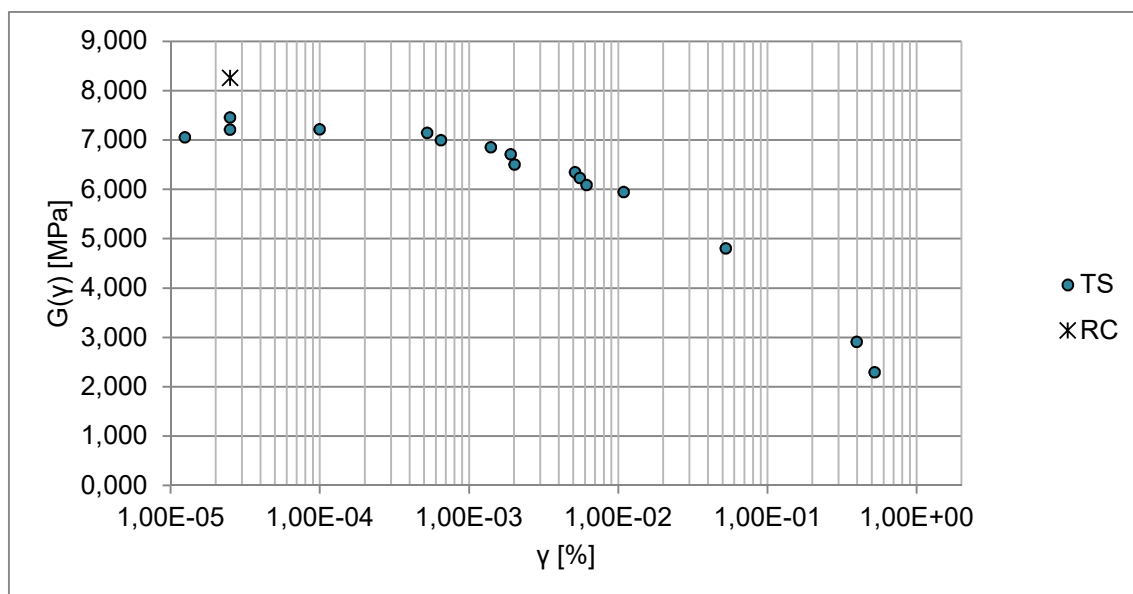


Figure 6.6 – Comparison between RC and TS test results in terms of shear modulus with respect to strain levels

As regards damping ratio, Figure 6.7 illustrates a comparison between RC, TS and DECAY tests. By referring to the strain level investigated by all three methods, “Free-decay” method results in the lowest damping ratio ( $D=0.406\%$ ), while “Half-power bandwidth method” provides the highest one ( $D=3.43\%$ ).

The direct evaluation through torsional shear test is the most reliable, since each value of damping ratio and shear modulus are determined on the basis of each hysteretic cycle. Since small strains damping ratio is a function of loading frequency, this dynamic property should be defined by considering loading frequencies typical of earthquakes, i.e.  $[0.1 \div 10 \text{ Hz}]$ . Usually TS tests are carried out in a frequency range of  $[0.1 \div 1 \text{ Hz}]$ , so it is more appropriate for evaluating small strains damping ratio, rather than RC test.

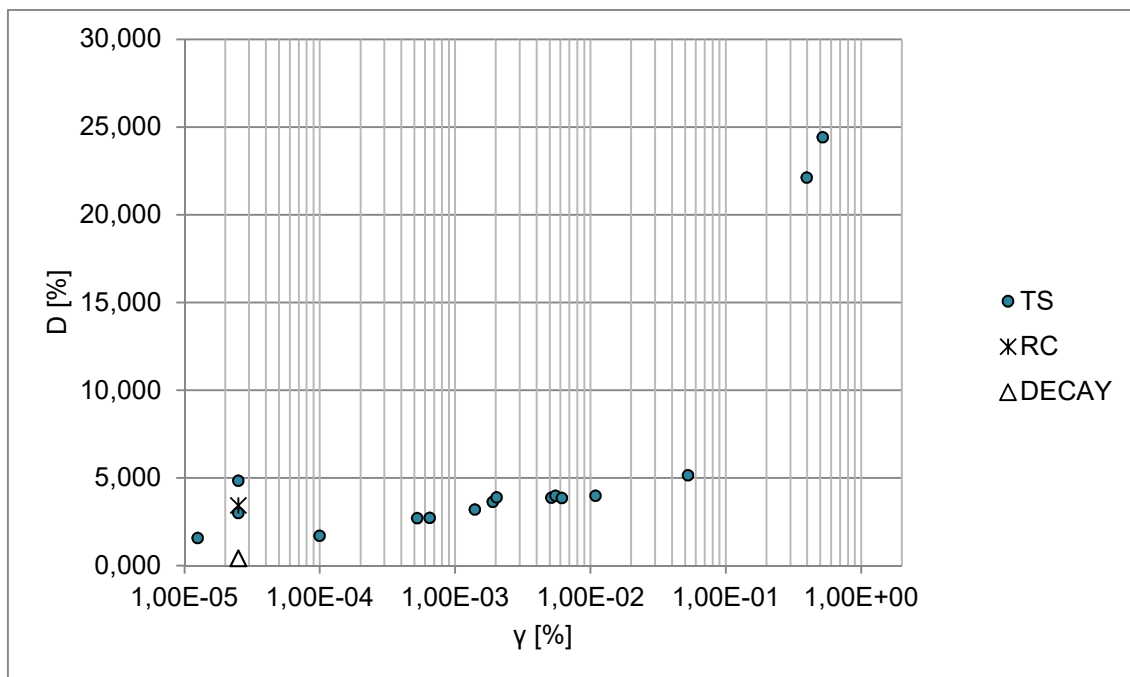


Figure 6. 7 – Comparison between RC, TS and DECAY test results in terms of damping ratio with respect to strain levels

## 6.1 Comparison of TS experimental results with Darendeli's model

Darendeli's model (2001) developed shear modulus and damping ratio degradation curves on the basis of a soil hyperbolic model previously proposed by Hardin and Drnevich (1972). The initial stress-strain relationship has been modified to guarantee a better fitting of experimental results. Damping ratio trend is described by means of an equation, which depends on the normalized shear modulus degradation curve, by assuming Masing's criteria (1926) as valid and by combining them with two correction parameters.

Darendeli (2001) presented graphical and tabulated normalized modulus and material damping curves to show both the effect of PI at a given mean effective stress and the effect of mean effective stress on a soil with given plasticity. In Figure 6. 8 and Figure 6. 9 two examples are showed and they correspond to values of mean effective stress and plasticity index close to real ones ( $\sigma'_0 = 1 \text{ atm} \sim 0,5 \text{ atm}$  and  $PI = 50 \sim 57$ ).

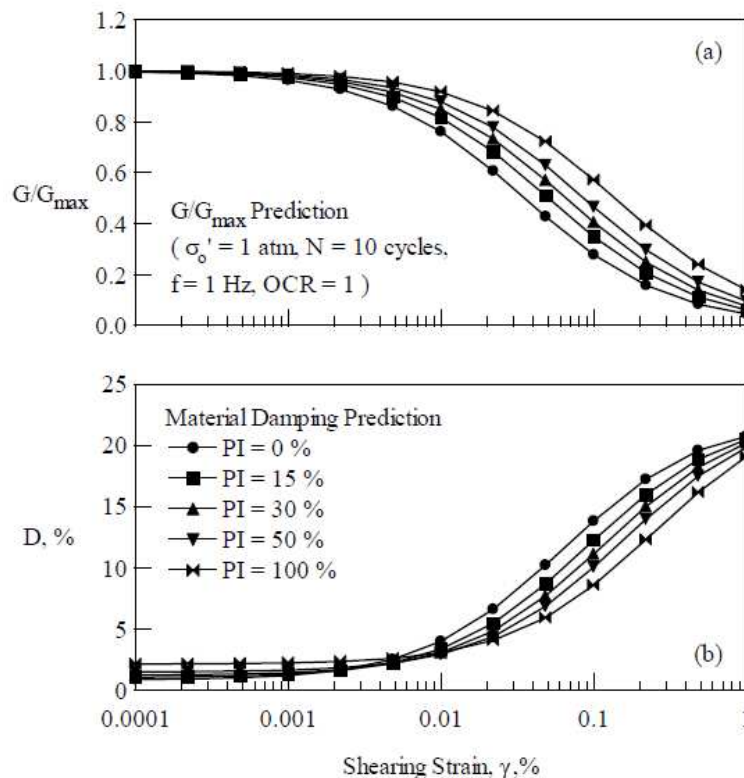


Figure 6. 8 – Effect of plasticity index on (a) normalized shear modulus and (b) damping ratio degradation curves (after Darendeli, 2001)

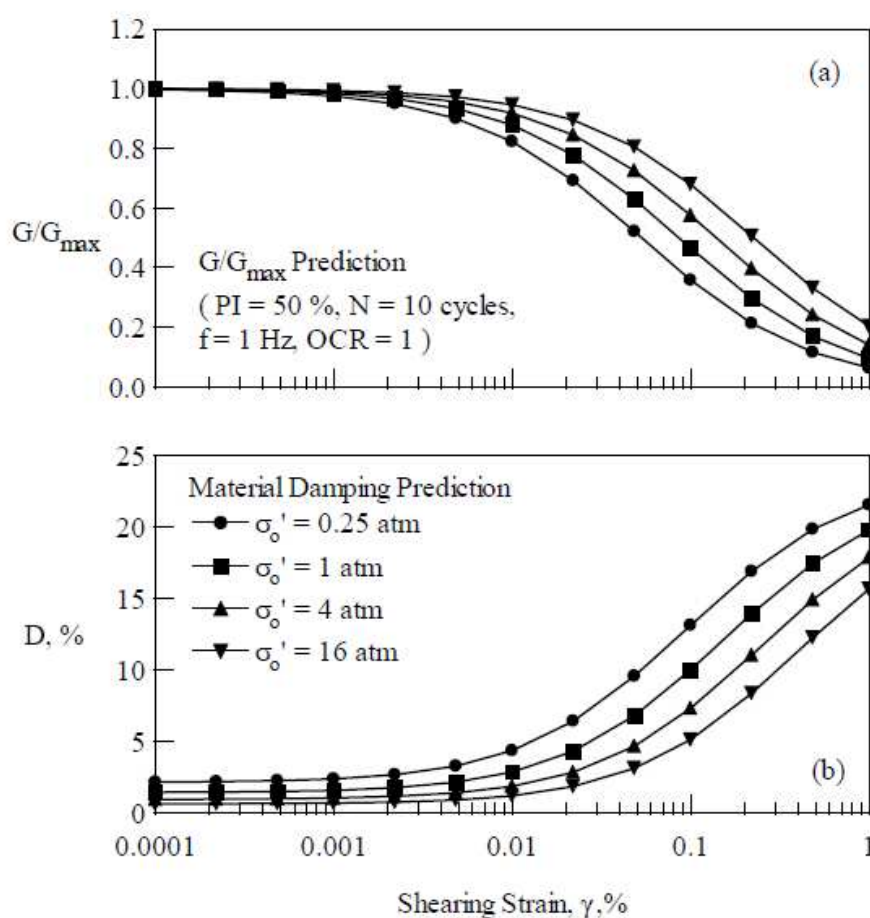


Figure 6. 9 – Effect of confinement pressure on (a) normalized shear modulus and (b) damping ratio degradation curves (after Darendeli, 2001)

In order to get a more specific comparison with the present work, normalized modulus and damping ratio curves are carried out numerically by means of the following equations proposed by the author.

According to the mentioned hyperbolic model, normalized shear modulus  $\frac{G}{G_{max}}$  is defined through the following equation

$$\frac{G}{G_{max}} = \frac{1}{1 + \frac{\gamma}{\gamma_r}} \tag{6.1}$$

where  $\gamma_r$  is called reference shear strain and it is the strain level corresponding to a half of the maximum shear modulus.

In order to get a better fitting of experimental results in terms of tangential stress-strain relationship, Darendeli introduced a curvature coefficient  $a$  in the previous equation:

$$\frac{G}{G_{max}} = \frac{1}{1 + \left(\frac{\gamma}{\gamma_r}\right)^a} \quad (6.2)$$

As regards the evaluation of damping ratio curve, Darendeli identified two main factors of influence. The first factor depends on energy lost due to friction at particle contacts and it is expressed through an equivalent damping ratio  $D_{eq}$ , while the second one regards soil non-linear behaviour, starting by shear modulus degradation curve and Masing's criteria.

Equivalent viscous damping ratio  $D_{eq}$  is expressed by the following equation:

$$D_{eq} = \frac{A_L}{4\pi A_T} \quad (6.3)$$

where:

- $A_L$  is the energy dissipation, given by the integration of stress-strain curve referred to one loading cycle;
- $A_T$  is the maximum stored elastic energy.

Stress-strain curve derives from shear modulus degradation curve through the well-known relationship  $\tau = G \cdot \gamma$ , where  $G$  is given by previous equation (6.2)

By combining equations (6.2) and (6.3), Masing's damping ratio, corresponding to a curvature coefficient  $a=1.0$ , results equal to:

$$D_{Masing,a=1.0}(\%) = \frac{100}{\pi} \cdot \left[ a \cdot \frac{\gamma - \gamma_r \left(\frac{\gamma + \gamma_r}{\gamma_r}\right)}{\frac{\gamma^2}{\gamma + \gamma_r}} - 2 \right] \quad (6.4)$$

Since the equation defining Masing's damping ratio  $D_{Masing}$  cannot be solved for curvature coefficients different from 1, a numerical approach is applied through 3 correction coefficients:

$$D_{Masing} = c_1 D_{Masing,a=1.0} + C D_{Masing,a=1.0}^2 + c_3 D_{Masing,a=1.0}^3 \quad (6.5)$$

where:

$$c_1 = -1.114a^2 + 1.8618a + 0.2523$$

$$c_2 = 0.0805a^2 - 0.0710a - 0.0095$$

$$c_3 = -0.0005a^2 + 0.0002a + 0.0003$$

However, at high strain levels, equation (6.5) provides damping values higher than the empirical correlation ones and, as a consequence, a correction function is defined as follow

$$F = b \cdot \left( \frac{G}{G_{max}} \right)^p \quad (6.6)$$

where b is a scale coefficient, which varies with the number of cycles, and p is a constant value equal to 0.1, as resulting from experimental results.

As previously described, at low strain levels a second factor takes part to the definition of the damping ratio curve and it is indicated as  $D_{min}$ . It varies according to soil types (plasticity index PI, over-consolidation ratio OCR and effective confinement stress  $\sigma'_o$ ) and to the loading frequency  $f_{load}$ .

The final damping ratio is expressed as follow:

$$D = b \cdot \left( \frac{G}{G_{max}} \right)^{0.1} \cdot D_{Masing} + D_{min} \quad (6.7)$$

which is an equation with four unknown parameters: reference strain level  $\gamma_r$ , curvature coefficient a, scale coefficient b and damping ratio at low strain levels  $D_{min}$ . According to Darendeli's model, each parameter is a function of coefficients  $\varphi_i$ , calibrated on experimental results.

In table Table 6. 1 and Table 6. 2 input parameters (soil type and loading frequency) and the four parameters of Darendeli's model are listed.

Table 6. 1 - Sample properties and input parameters of TS tests

PI [%]	57
$\sigma'_o$ [atm]	0,5
$f_{load}$ [Hz]	2
N	9
OCR	2

Table 6. 2 - Parameters of Darendeli's model

$\gamma_r$ [%]	0,08
a	9,19E-01
$D_{\min}$ [%]	2,18E+00
b	0,62

Degradation curves described by equations (6.8) and (6.9) are mean curves, which means that experimental results are distributed into a dispersion band surrounding estimated curves. Standard deviations for both shear modulus degradation and damping ratio are computed respectively as

$$\sigma_{NG} = \exp(\varphi_{13}) + \sqrt{\frac{0.25}{\exp(\varphi_{14})} - \frac{\left(\frac{G}{G_{max}} - 0.5\right)^2}{\exp(\varphi_{14})}} \quad (6.8)$$

$$\sigma_D = \exp(\varphi_{15}) + \exp(\varphi_{16}) \cdot \sqrt{D} \quad (6.9)$$

Figure 6. 10 and Figure 6. 11 illustrates comparisons between TS test results and Darendeli's curve both in terms of normalized shear modulus degradation curve and damping ratio curve, by plotting mean values and standard deviations.

In both cases experimental results from TS tests follow Darendeli's hyperbolic curves with a good accuracy. Especially, the main part of normalized shear modulus points fall within the identified uncertainty range.

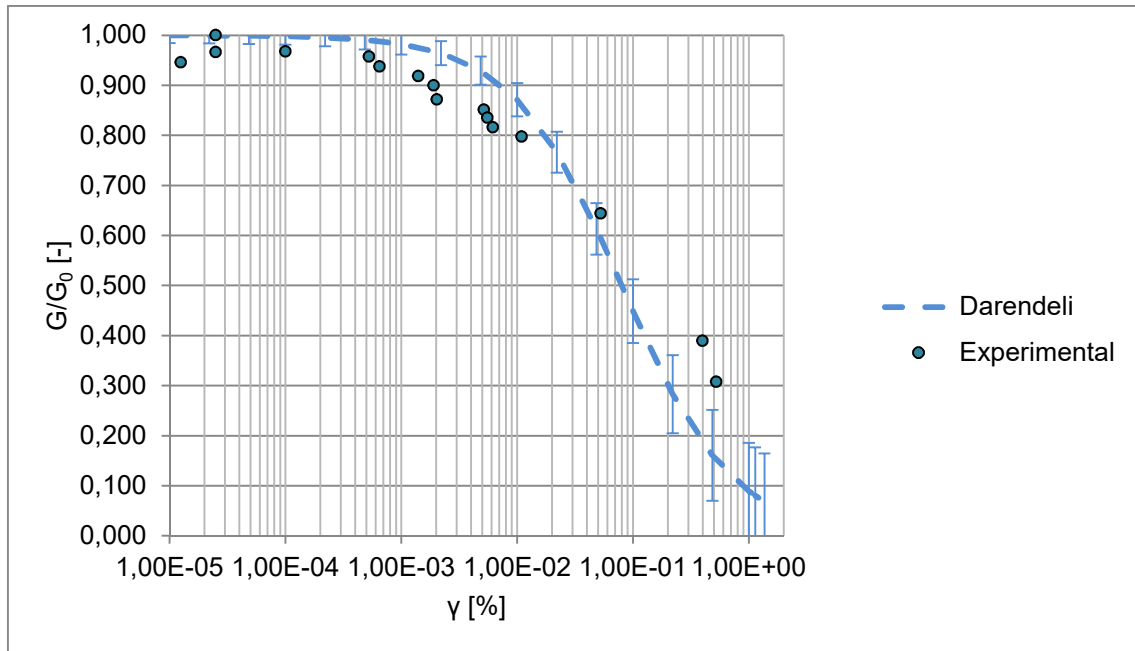


Figure 6. 10 – Comparison between experimental results (TS test) and Darendeli’s model in terms of normalized shear modulus degradation curve as shear strain increases

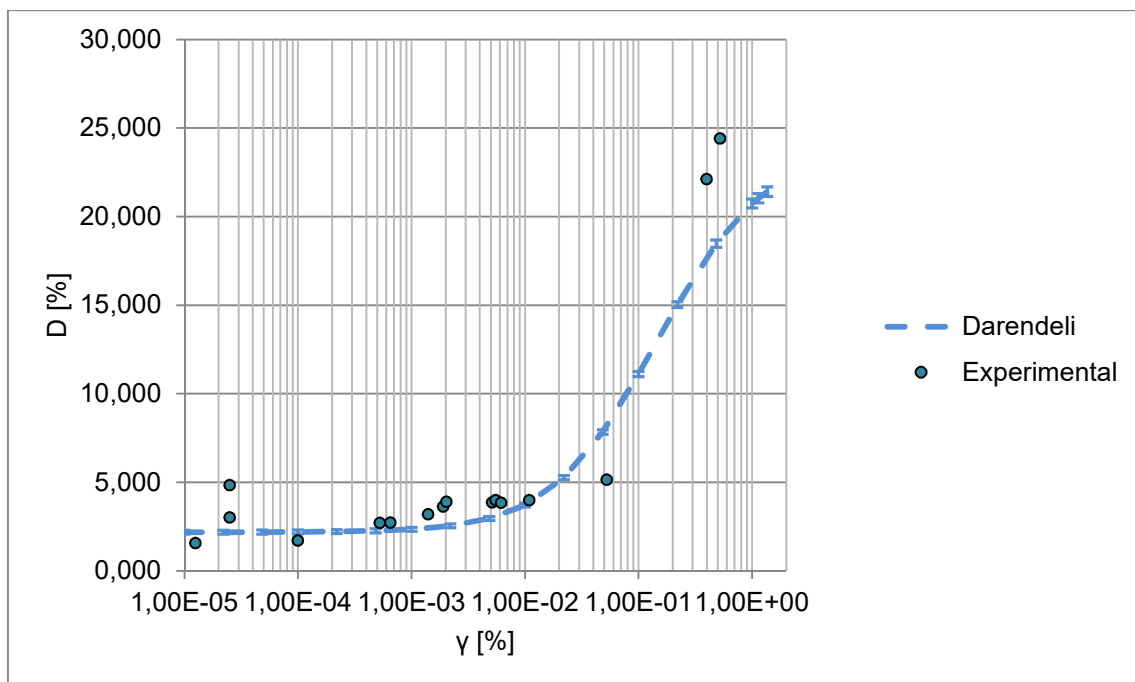


Figure 6. 11 – Comparison between experimental results (TS test) and Darendeli’s model in terms of damping ratio evolution curve as shear strain increases

## 6.2 Comparison of TS experimental results with Vucetic&Dobry's model (1991)

Empirical correlations proposed by Vucetic and Dobry (1991), in terms of both shear modulus degradation and damping ratio curves, vary as a function of the plasticity index. Especially, trends for PI values equal to 0%- 15%- 30%- 50%- 100%- 200% are fully provided by authors.

The best fitting with experimental data can be verified by choosing the Vucetic&Dobry's curve corresponding to tested soil PI.

In Figure 6. 12 and Figure 6. 13 is showed a comparison between TS test results and empirical curves corresponding to PI=50 and PI=100, since soil plasticity index is approximately equal to 57.

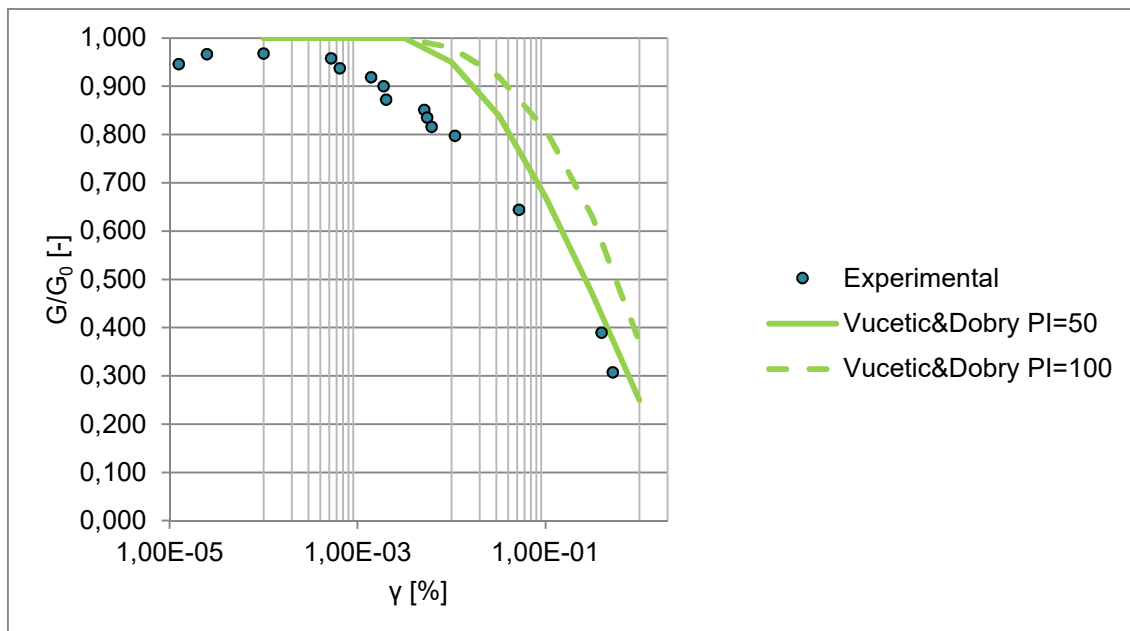


Figure 6. 12 –Comparison between experimental results (TS test) and Vucetic&Dobry's model in terms of normalized shear modulus degradation curve as shear strain increases

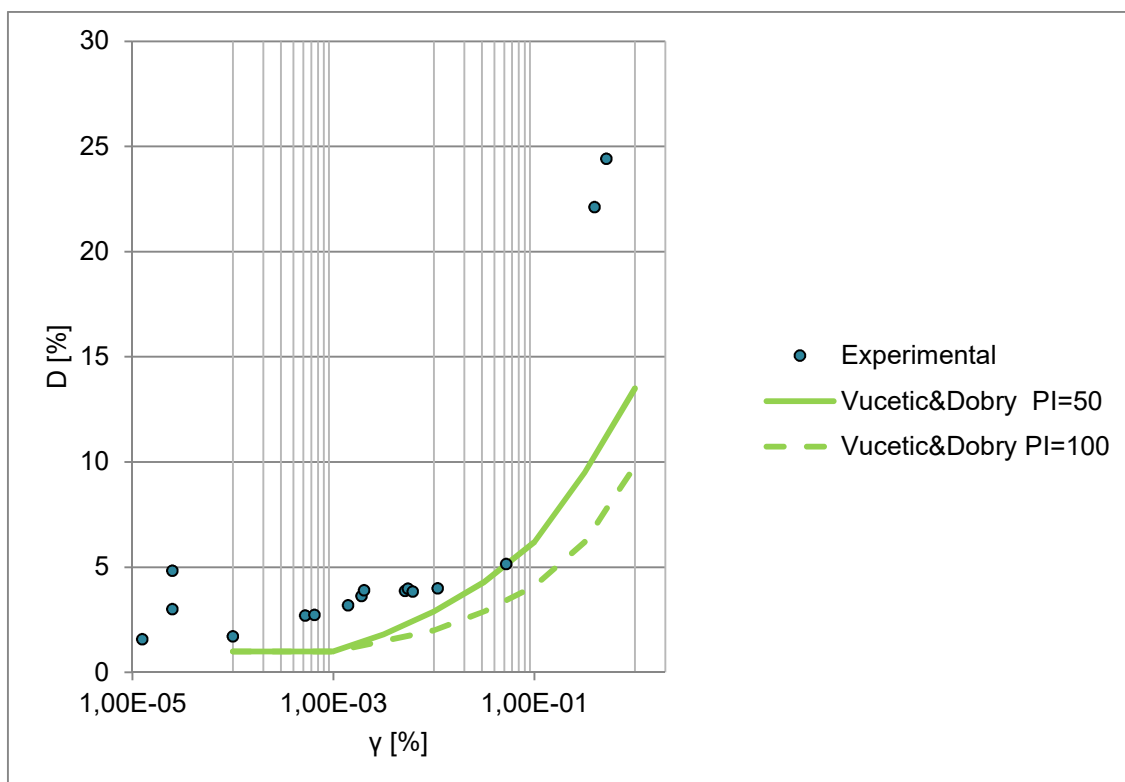


Figure 6. 13 – Comparison between experimental results and Vucetic&Dobry's model in terms of damping ratio evolution curve as shear strain increases

It results that experimental data follow a trend similar to the one proposed by Vucetic&Dobry (1991), but TS test provides lower values of normalized shear modulus and higher values of damping ratio with respect to empirical correlation. Such a difference between carried out TS results and curves proposed by Vucetic&Dobry (1991) can be justified by considering effects of confinement pressure and OCR on dynamic behaviour of tested materials, in addition to plasticity index.

On the basis of plotted comparisons, the dynamic behaviour of Black Cotton clays is more properly reproduced by Darendeli's model rather than Vucetic&Dobry's one, which is not able to describe all aspects and peculiarities of the dynamic response of tested clay.

### **6.3 Comparison of experimental results with Italian case studies**

In the following section results of Black Cotton soil RCTS tests are compared with results of three different survey campaigns, aimed to the geotechnical characterisation of the following sites:

- foundation soil of Torre Ghirlandina (Modena, Italy);
- soil constituting the body and the right bank of the Po river;
- area of central Italy hit by the earthquake in 2016-2017.

Resonant column and Torsional shear tests were carried out at the geotechnical laboratory of the Department of Structural, Geotechnical and Building Engineering (DISEG, Politecnico di Torino).

The first research convention involves the characterisation of soils coming from geotechnical surveys carried out at Modena (Piazza Grande) and both classification and mechanical laboratory tests were performed on undisturbed samples. Mechanical characterisation includes resonant column tests with 50 mm diameter samples, a fixed-free apparatus, characterised by an electrical motor made of 4 magnets and 8 coils, with a maximum torque of 1.1 Nm. The motor is controlled by a programmable signal generator, connected to a power amplifier. During the consolidation phase an isotropic stress is applied on samples, while the resonance phase involves undrained condition. Interpretation of RC results is done according to ASTM D4015.

The same apparatus was used for testing Po river soils, both for undisturbed samples with 50 mm diameter and 100 mm height and for reconstituted sand cable samples, characterised by an internal diameter equal to 50 mm, external diameter equal to 70 mm and height of 140 mm. In this case, mechanical characterisation involved both resonant column and torsional shear tests, which were carried out 24h after RC tests, with a constant excitation frequency of 0.1 Hz, a sinusoidal wave shape and 24 loading cycles for each excitation level.

Comparisons with African Black Cotton soil is made by selecting those tests with similar values of liquid limit, plasticity index and clay content. In Table 6. 3 selected tests with a summary of main soil properties are listed, by specifying which site they belong to.

Table 6. 3 – Summary of soil properties and test conditions of each case study

Site	Test	Liquid limit $w_L$ [%]	Plasticity index PI [%]	Clay content [%]	OCR [-]	$\sigma'_c$ [atm]
Torre Ghirlandina (Modena)	RC_109_Mod	79.8	44.8	69.6	1	1.017
	RC_112_Mod	67.2	37.1	51.8	1	1.163
	RC_113_Mod	95.1	62.8	76.9	1	0.894
Po river	RC_125_Aipo	89.4	49	72.1	1	1.5
	TS_125_Aipo					
Montegiorgio	RC	61.7	41.9	47.16	1	2.6
	TS					
Tolentino	RC	67.3	42.4	67	1	2.7
	TS					
Black Cotton Clay	TS	87.0	57.0	62.0	2	0.5

As shown in the section 6, Black Cotton clay RC tests are carried out to investigate small strains behaviour only in terms of initial shear modulus  $G_0$  and initial damping ratio  $D_0$ , so there are not enough points to compare degradation curves with data previously presented.

As a consequence, comparisons are made in terms of shear modulus and damping degradation curves resulting from TS tests, except for soils from Modena (RC\_109/112/113\_Mod) for which only resonant column tests were carried out. Since different methods are adopted to estimate damping ratio in RC and TS test, related to half power bandwidth and area of hysteresis cycle respectively, it follows that the dynamic behaviour of soil samples from Torre della Ghirlandina is reasonably comparable with others only in terms of shear modulus degradation curves.

As regards Po river soils and soils from central Italy (Montegiorgio and Tolentino), they were characterised by performing both resonant column and torsional shear tests, but only TS results are plotted in Figure 6. 14 and Figure 6. 15.

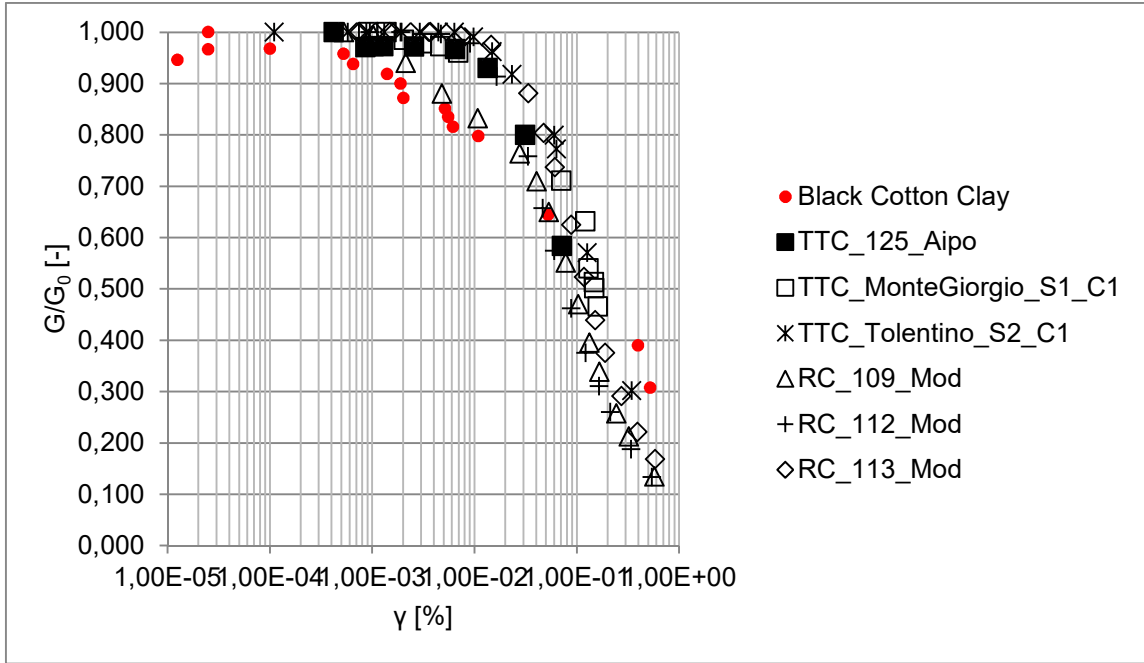


Figure 6. 14 – Comparison between Black Cotton clay and Italian case studies in terms of normalized shear modulus degradation curves as shear strain increases (TS test)

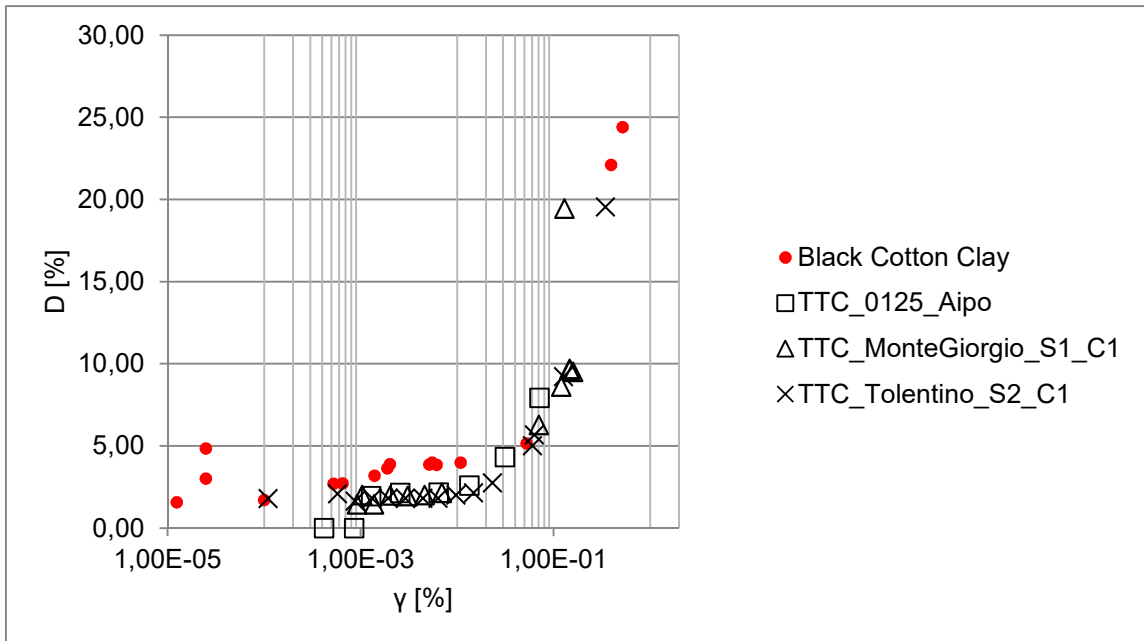


Figure 6. 15 – Comparison between Black Cotton clay and Italian case studies in terms of damping ratio evolution curves as shear strain increases (TS test)

Plotted comparisons highlight the effects of the plasticity index and the confinement pressure on degradation curves, according to Darendeli's model (2001), as summarized in section 6.2. Indeed, all clays follow the same trend both in terms of shear modulus and damping ratio and minor differences can be explained by taking into account the presence of a little range of variation of the plasticity index (PI) and effective confinement pressure ( $\sigma'_c$ ), as shown in Table 6. 3.

In the following section results of TS tests listed in Table 6. 3 are compared with empirical models by Darendeli (2001) and Vucetic&Dobry (1991), both in terms of shear modulus degradation curve and damping ratio curves (Figure 6. 16, Figure 6. 17, Figure 6. 18, Figure 6. 19, Figure 6. 20, Figure 6. 21), in order to highlight similarities regarding dynamic response and effects of confinement pressure on soil behaviour. In Table 6. 4 are listed all parameters proposed by Darendeli's model, computed as a function of plasticity index, effective confinement pressure, OCR, loading frequency and number of loading cycles.

Table 6. 4 – Parameters of Darendeli's model referred to three Italian case studies

	Po river	Montegiorgio	Tolentino
$\gamma_r$ [%]	0,10	0,11	0,15
a	1,10E+00	9,19E-01	1,10E+00
$D_{\min}$ [%]	4,18E-01	8,12E-01	9,97E-01
b	0,62	0,62	0,62

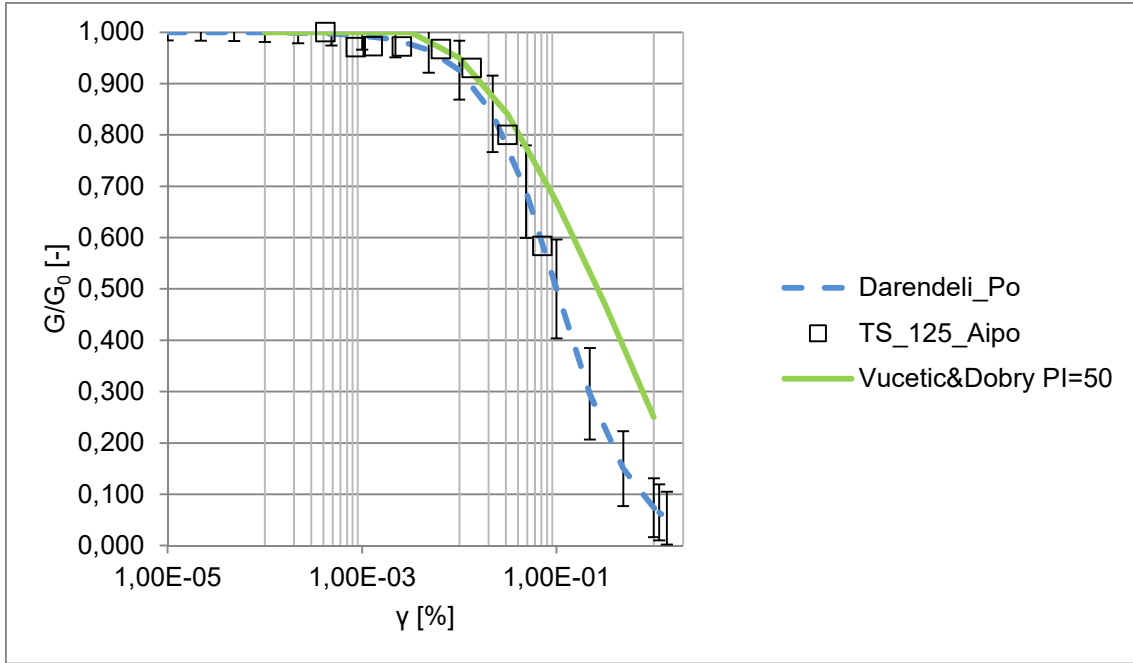


Figure 6. 16 – Comparison between results of TS test on Po river soil, Darendeli's model and Vucetic&Dobry's model in terms of normalized shear modulus degradation curve as shear strain increases

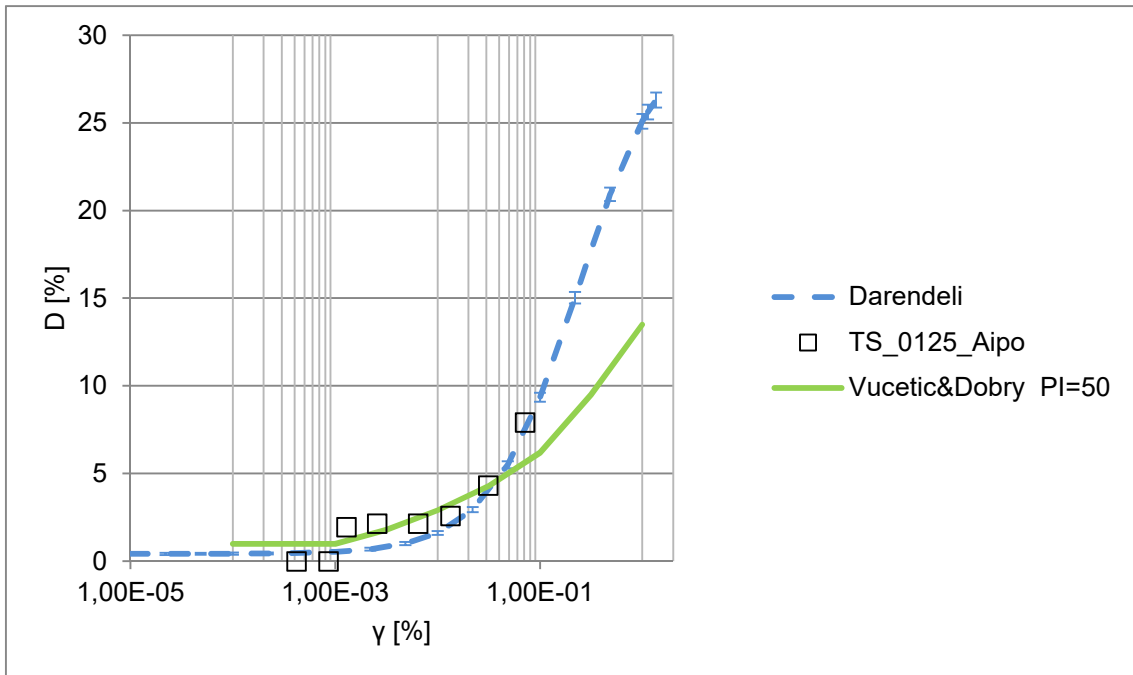


Figure 6. 17– Comparison between results of TS test on Po river soil, Darendeli's model and Vucetic&Dobry's model in terms of damping ratio evolution curve as shear strain increases

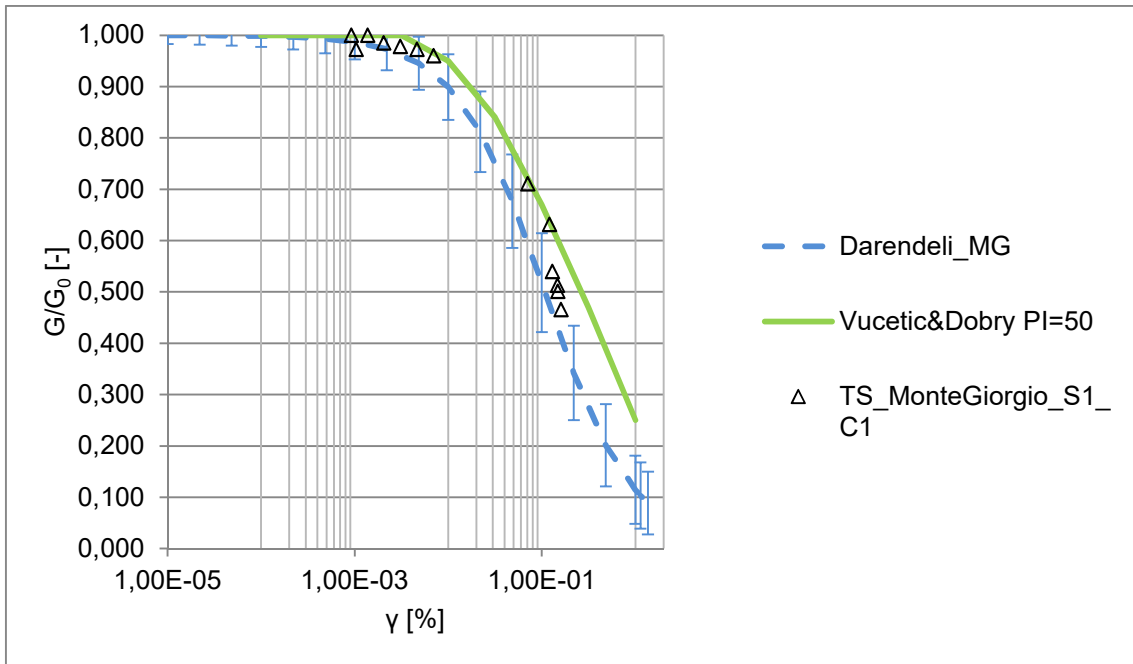


Figure 6.18 – Comparison between results of TS test on Montegiorgio soil, Darendeli’s model and Vucetic&Dobry’s model in terms of normalized shear modulus degradation curve as shear strain increases

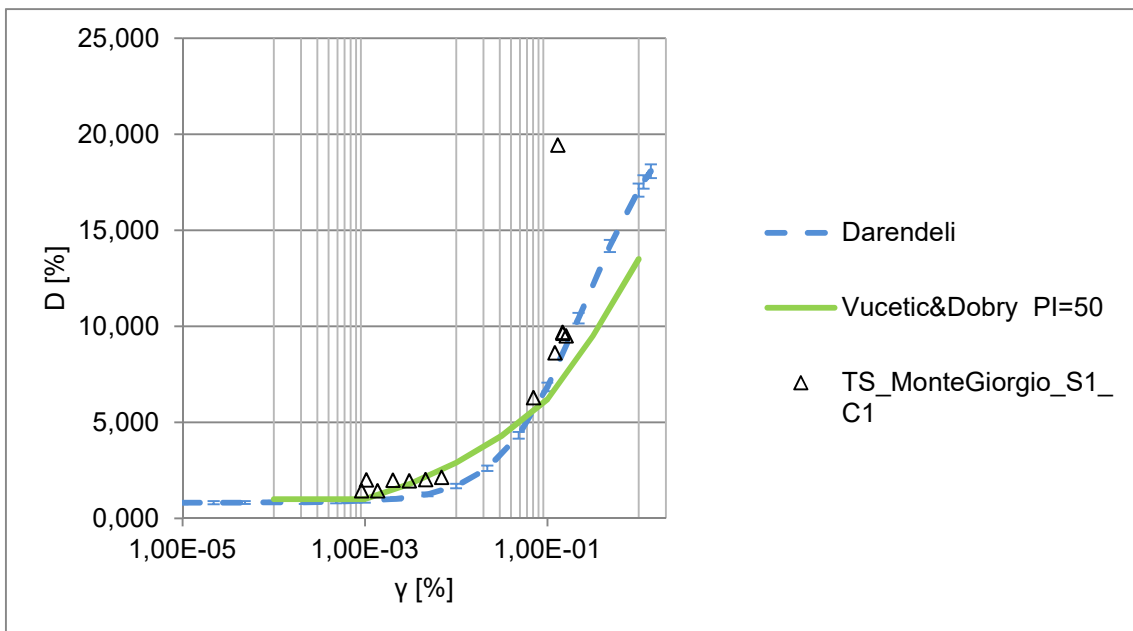


Figure 6.19 – Comparison between results of TS test on Montegiorgio soil, Darendeli’s model and Vucetic&Dobry’s model in terms of damping ratio evolution curve as shear strain increases

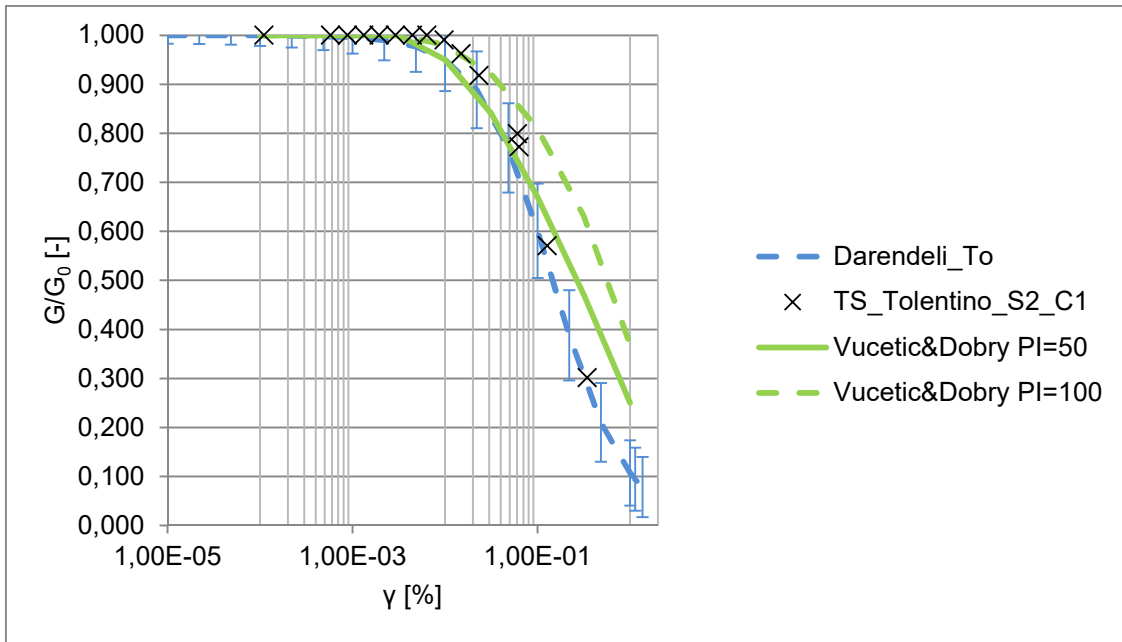


Figure 6. 20 – Comparison between results of TS test on Tolentino soil, Darendeli's model and Vucetic&Dobry's model in terms of normalized shear modulus degradation curve as shear strain increases

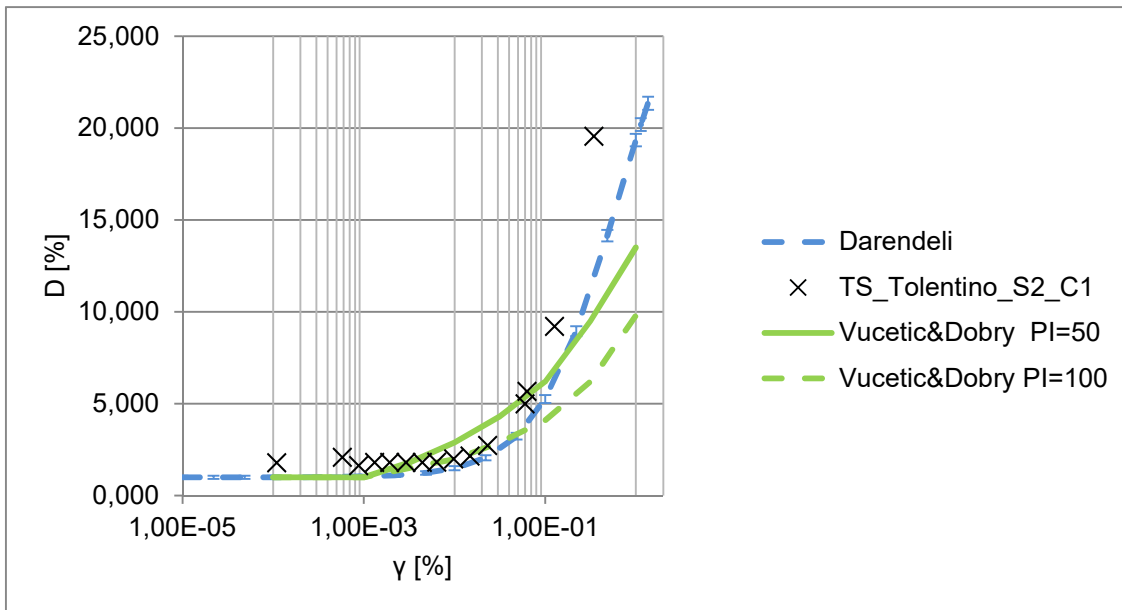


Figure 6. 21 – Comparison between results of TS test on Tolentino soil, Darendeli's model and Vucetic&Dobry's model in terms of damping ratio evolution curve as shear strain increases

Plotted comparisons confirm that the behaviour of analysed clays is principally governed by the plasticity index, but other factors such as confinement pressure, OCR, loading frequency and number of loading cycle influences the overall trend of dynamic response. It follows that Darendeli's model allows to reproduce more properly not only African clay behaviour but also all other results from Italian case studies.

Finally, shear modulus degradation curves resulting from carried out best fitting procedure according to Darendeli's model are plotted in Figure 6. 23, in order to highlight that the influence of effective confinement pressure on the dynamic response is higher for low plasticity-clays rather than for high-plasticity tested ones (Ishibashi, 1992), see Figure 6. 22.

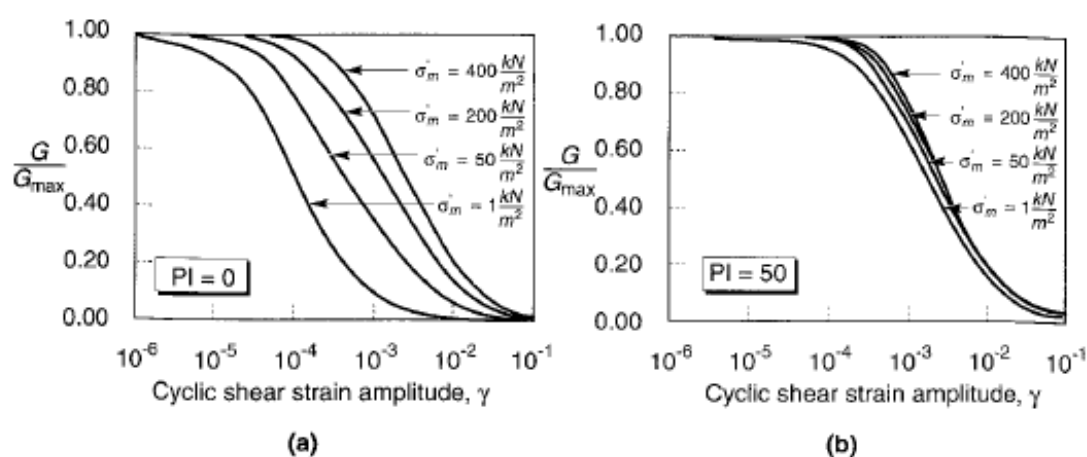


Figure 6. 22 – Influence of mean effective confining pressure on modulus degradation curves for (a) non plastic (PI=0) soil and (b) plastic (PI=50) soil (After Ishibashi, 1992)

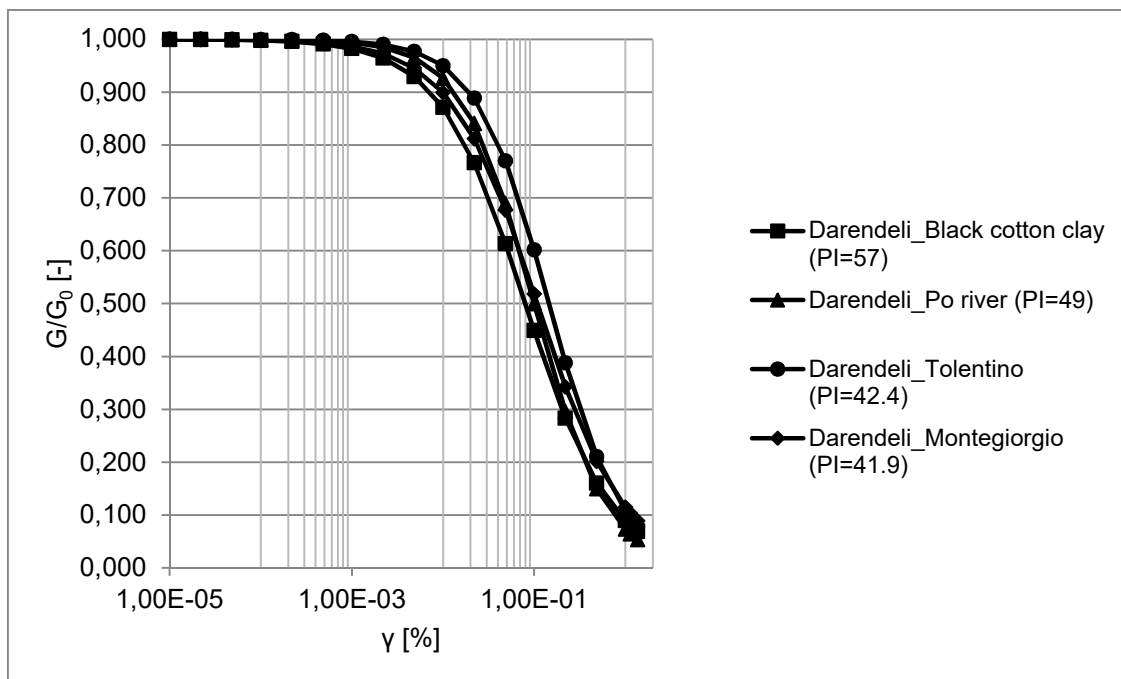


Figure 6.23 – Effect of mean effective confining pressure on normalized shear modulus degradation curves for tested plastic soils

## 7. Conclusions and future implications

The work described in this thesis was carried out at University of Cambridge in the wider context of the WindAfrica research project. In particular, this thesis focuses on the characterisation of two tropical expansive clays from two locations in Africa: Black Cotton Clay from Al Fao, Sudan (SUD) and Atta Clay from Steelpoort, South Africa (SA).

After an initial review of the technical literature on the mechanical and hydro-mechanical behaviour of unsaturated soils, a description of the distribution of tested tropical clay soils (geology, climate, localization and sampling procedures) is presented. On the basis of results obtained by performing particle size distribution and Atterberg limit tests, both clays are classified as slightly sandy silty clay according to BS classification and sandy fat clay (CH) according to ASTM (Table 3. 2).

According to the experimental program the hydraulic behaviour of tested materials is investigated under unsaturated conditions, while the dynamic one under saturated conditions.

Especially, by referring to hydraulic behaviour, soil suction measurements were carried out on four discs for each clay through a WP4C device, with an upper measuring limit equal to -300 MPa, which does not allow to investigate the full drying curve for the tested materials. Primary Drying Curves of SWRCs for both tested tropical clays are plotted as a relationship between the logarithm of suction and either degree of saturation  $S_r$ , void ratio  $e$  or gravimetric water content,  $w$ .

Results highlight that one of main differences between two tested clays regards the saturation level at the limit of dewpoint method (Figure 5. 1 and Figure 5. 6), which is lower ( $S_r=20\%$ ) for Atta Clay with respect to Black Cotton Clay ( $S_r=40\%$ ), since Sudanese soil is more plastic with a high fine content, so greater suctions are generated at comparable stages (Abdalla *et al.*, 2019). Another fundamental aspect resulting from hydraulic characterization is that samples remained almost saturated ( $S_r = 80-90\%$ ) up to suction levels of about 5 MPa, which represents the air-entry value (AEV) of tested materials (Figure 5. 2 and Figure 5. 7). This aspect has been confirmed by results of the fitting process according to Van Genuchten's model, with parameters estimated for both tested clays through the least squares method (Table 5. 4 and Table 5. 5).

On the other hand, small strains dynamic behaviour was investigated under saturated condition, using a suction-controlled Resonant Column-Torsional Shear

apparatus (RCTS), designed specifically to test partly saturated soils by measuring the shear stiffness (G) and the damping ratio (D) in isotropic stress conditions. A detailed description of each part of the RCTS apparatus is presented, together with all preliminary steps of saturation of both water circuits and the High Air-Entry Value (HAEV) porous stone. In particular, the air entry value of tested Black Cotton Clay is higher than the one of the HAEV porous stone installed in the RCTS apparatus, so that only a saturated test was carried out, including a resonant column, a torsional shear and a decay test. Results are presented in terms of obtained normalized shear modulus and damping ratio variation curves (chapter 6), which were compared with both empirical correlations and Italian case studies. The first comparison refers to Darendeli's model (2001) and Vucetic&Dobry's model (1991) and highlights that the last one does not allow to properly reproduce tested clay behaviour at small strains, since unlike Darendeli's model (Figure 6. 10 and Figure 6. 11) it does not take into account effects of confinement pressure and OCR (Figure 6. 12 and Figure 6. 13). As regards Italian case studies, results of RC and TS tests carried out on clays from four different sites (Torre Ghirlandina, Po river, Montegiorgio and Tolentino) are analysed and a comparison with African Black Cotton soil was made by selecting those tests with similar values of liquid limit, plasticity index and clay content (Table 6. 3). As expected, small strains behaviour of such clays with similar properties follows a similar trend in terms of normalized shear modulus and damping ratio variation curves, both in terms of experimental results (Figure 6. 14 and Figure 6. 15) and fitting curves, according to Darendeli's model (Figure 6. 23). Due to the high plasticity index, the influence of effective confinement pressure on the dynamic behaviour is negligible, according to Ishibashi (1992).

The carried out dynamic characterisation at small and medium strains has been limited to saturated conditions due to the interruption forced by coronavirus COVID-19 pandemic, but future implications could include suction-controlled RCTS tests on partly saturated samples, in order to highlight suction effects on the initial shear modulus. According to Vassallo *et al.* (2007), stages of drying and wetting at constant mean net stress show that changes of suction may cause both an increase of initial shear stiffness corresponding to a given stress state and an accumulation of irreversible changes of specific volume and specific water volume.

By referring to partly saturated tests, such a high AEV of tested tropical clays strongly influenced the carried out dynamic characterisation at small and medium strains, through the suction-controlled RCTS set up in the Geomechanics laboratory at the University of Cambridge. Indeed, one of the main limit of this apparatus regards the HAEV porous disc, characterised by an air-entry value of 5 bar and rigidly glued to the pedestal, so that it cannot be changed without substituting the whole base. As a consequence, future modifications could involve

adding to the already existing apparatus a new pedestal with a porous disc with a higher air entry value (e.g. 15 bar), in order to allow suction-controlled RCTS tests on such clays with especially high air-entry values.

Alternatively, the same apparatus can be used avoiding any modifications, by performing RCTS tests at constant water content without controlling sample suction. It means that all water and air circuits are closed during the loading phase, similarly to undrained conditions. Sample water content is previously chosen and imposed by preparing partly saturated compacted samples or by allowing an air drying process on fully saturated reconstituted samples (Tarantino, 2009). Once known the water content, sample suction is obtained through already measured SWRCs or by measuring total suction of a representative portion of the tested sample through a WP4C device, both immediately before setting up and once concluded the test, in order to ensure that sample suction remains constant during the whole test.

The main limit of this procedure regards the impossibility of following drying and wetting stages during loading phases, in order to investigate the combined effect of net stress and suction history on small strain stiffness (Vassallo *et al.*, 2007). Sample suction cannot be changed and, as a consequence, the experimental program could include only tests with loading and unloading stress path at constant suction.



## REFERENCES

- Abdalla, Khalid, *et al.* "Soil water retention curves representing tropical clay soils from Africa." (2019).
- Allen, J. C., and K. H. Stokoe. *Development of resonant column apparatus with anisotropic loading*. Geotechnical Engineering Center, Civil Engineering Department, University of Texas, 1982.
- Al Haj, K. (2014). Mechanical response of two plastic clay soils from Sudan. PhD thesis, Imperial College London, UK.
- Al Haj, K. M. A., and J. R. Standing. "Soil water retention curves representing two tropical clay soils from Sudan." *Géotechnique* 66.1 (2016): 71-84.
- Alonso, E.E., Gens A. and Hight D.W. 1987. Special problem soils. General report. Proceedings of the IX ECSMFE, Dublin, 3, pp. 1087-1146.
- Alonso, E.E., Gens A. and Josa A. 1990. A constitutive model for partially saturated soils. *Géotechnique* 40(3), pp. 405-430.
- Anderson D.G. and Stokoe K.H. 1978. Shear modulus: a time-dependent material property. *Dynamic geotechnical testing*, ASTM STP 654, pp. 66-90.
- ASTM. Standard practice for classification of soils for engineering purposes (Unified Soil Classification System). ASTM-D2487, West Conshohocken, PA, 2011.
- Bishop, A. W. 1959. The principle of effective stress. *Teknisk Ukeblad*. 39, pp. 859-863.
- Bishop A.W. and Blight G.E. 1963. Some aspects of effective stress in saturated and partially saturated soils, *Géotechnique*, 13(3), pp. 177-197.
- Buisson M.S.R. and Wheeler S.J. 2000. Inclusion of hydraulic hysteresis in a new elasto-plastic framework for unsaturated soils. Proc. of an International Workshop on Unsaturated Soils, Trento.

- Burland, J. B. (1990). On the compressibility and shear strength of natural clays. *Géotechnique*, 40(3), 329-378.
- Buursink, J. (1971), Soils of central Sudan, PhD thesis, Rijksuniversiteit te Utrecht.
- Cabarkapa Z., Cuccovillo T. and Gunn M. 1998. A new triaxial apparatus for testing unsaturated soils. *Proc. II Int. Conf. on Unsaturated Soils. UNSAT '98*, Beijing, China, vol. 2, pp. 194-195.
- Cabarkapa Z., Cuccovillo T., and Gunn M. 1999. Some aspects of the pre-failure behaviour of unsaturated soil. *Proc. II Int. Conf. on pre-failure behaviour of geomaterials*, vol. 1, pp. 159-165.
- Chopra, A. K. (2002). Dynamics of Structures. Prentice-hall International Series in Civil Engineering and Engineering Mechanics. William J. Hall, Editor.
- Clayton, C. R. I., *et al.* "The Stokoe resonant column apparatus: effects of stiffness, mass and specimen fixity." *Geotechnique* 59.5 (2009): 429-437.
- Darendeli M.B. (2001). Development of a new family of normalized modulus reduction and material damping curves. Ph.D. Dissertation, The University of Texas at Austin.
- Drnevich, V. P., B. O. Hardin, and D. J. Shippy. "Modulus and damping of soils by the resonant-column method." *Dynamic geotechnical testing*. ASTM International, 1978.
- Foti S., (2019). La caratterizzazione geotecnica per la progettazione in zona sismica. Risposta sismica locale. Comportamento dinamico dei terreni e prove di laboratorio. Dispense dal Corso di Geotecnica Sismica. Politecnico di Torino, Torino.
- Fisher R.A. 1926. On the capillary forces in an ideal soil, *Journal Agr. Science*, 16, pp. 492-505.
- Fredlund D.G., Morgenstern N.R. and Widger R.A. 1978. The shear strength of unsaturated soils. *Canadian Geotechnical Journal*, 15(3), pp. 313-321

- Fredlund D.G. and Rahardjo H. 1993. Soil Mechanics for Unsaturated Soils. Wiley & sons, Toronto.
- Gan J.K.M., Fredlund D.G. and Rahardjo H. 1988. Determination of shear strength parameters of unsaturated soils using direct shear test. *Canadian Geotechnical Journal*, 25, pp. 500-510.
- Garven, E. A., & Vanapalli, S. K. (2006). Evaluation of empirical procedures for predicting the shear strength of unsaturated soils. In *Unsaturated Soils 2006* (pp. 2570-2592).
- Gens A. and Alonso E.E. 1992. A model for the behaviour of unsaturated expansive clays. *Canadian Geotechnical Journal*, 29, pp. 1013-1032.
- Gidigasu, S. S. R., and S. K. Y. Gawu. "The mode of formation, nature and geotechnical characteristics of black cotton soils—a review." *Stand Sci Res Essays* 1.14 (2013): 377-390.
- Hardin B.O. and Black W.L. 1968. Vibration modulus of normally consolidated clay. *J. Geotech. Engrg. ASCE*. 94(2), pp. 353-369.
- Hardin, Bobby O., and Vincent P. Drnevich. "Shear modulus and damping in soils: measurement and parameter effects." *Journal of Soil Mechanics & Foundations Div* 98.sm6 (1972).
- Hilf J.W. 1956. An investigation of pore-water pressure in compacted cohesive soils. *Ph.D. thesis, Technical Memo*, 654, U.S. Department of Interior. Bureau of Reclamation, Design and Construction Division, Denver.
- Isenhower W.M. 1979. Torsional Simple Shear/Resonant Column properties of San Francisco Bay Mud. *M.S. Thesis, The University of Texas at Austin*.
- Ishibashi, I. (1992). Discussion of "Effect of Soil Plasticity on Cyclic Response" by Mladen Vucetic and Ricardo Dobry (January, 1991, Vol. 117, No. 1). *Journal of Geotechnical Engineering*, 118(5), 830-832.
- Jennings J.E. and Burland J.B. 1962. Limitations to the effective stresses in partly saturated soils. *Géotechnique*, 12, pp. 125-144.

- Josa A., Alonso E.E., Lloret A. and Gens A. 1987. Stress-strain behaviour of partially saturated soils. IX Eur. Conf. Soil Mech. Found. Eng., Dublin, 2, pp. 561-564.
- Köppen, W. (1931), Grundriss der klimakunde, W. de Gruyter Berlin, Leipzig.
- Kramer S. L., (1996). Geotechnical earthquake engineering. Prentice Hall, Upper Saddle River, N.J.
- Lanzo, G., & Silvestri, F. (1999). *Risposta sismica locale: teoria ed esperienze*. Hevelius.
- Li, H., H. He, and K. Senetakis. "Calibration exercise of a Hardin-type resonant column." *Geotechnique* 68.2 (2018): 171-176.
- Lloret-Cabot, M., S. J. Wheeler, and M. Sánchez. 2017. "A unified mechanical and retention model for saturated and unsaturated soil behaviour." *Acta. Geotech.* 12 (1): 1–21
- Mancuso, C., Vassallo R. and Vinale F. 2000a. Effects of moulding water content on the behaviour of an unsaturated silty sand. Asian Conference on Unsaturated Soils, Singapore 1:545-550.
- Mancuso C., Vassallo R. and d'Onofrio A. 2002. Small strain behavior of a silty sand in controlled-suction resonant column – torsional shear tests. *Canadian Geotechnical Journal*, vol. 39, 22-31.
- Marinho, F. A. M., Chandler, R. J., & Crilly, M. S. (1995). Stiffness measurements on an unsaturated high plasticity clay using bender elements. In proceedings of the first international conference on unsaturated soils/unsat'95/paris/france/6-8 september 1995. volume 2.
- Masing G. (1926). Eigenspannungen und verfestigung beim messing. Proc. 2nd International Congress of Applied Mechanics, Zurich, Swisse. (in German).
- Matyas E.L. and Radhakrishna H.S. 1968. Volume change characteristics of partially saturated soils. *Géotechnique* 18(4), pp. 432-448
- Miller D.J. and Nelson J.D. 1993. Osmotic suction as a valid stress state variable

in unsaturated soil mechanics. *Unsaturated soils*, ASCE Special Publication 39, pp. 64-76.

Morin, W. J. (1971), 'Properties of african tropical black clay soils', *Journal Fifth Regional Conference for Africa on Soil Mechanics and Foundation Engineering, Angola* (2)(1), pp.46{54.

Mualem, Y. (1976). A new model for predicting the hydraulic conductivity of unsaturated porous media. *Water resources research*, 12(3), 513-522.

Price M. 1985. *Introduction to groundwater*. Chapman & Hall, London.

Quian X., Gray D.H. and Woods R.D. 1991. Resonant column tests on partially saturated sands. *Geotech, Testing Journ., ASCE*, 14(3), pp. 266-275.

Rampello S., Silvestri F. and Viggiani G. 1995. The dependence of  $G_0$  on stress state and history. *Proc. of the 1st Int. Symp. On Pre-failure Deformation of Geomaterials, Sapporo*, 2, pp. 1155-1160.

Rampino C., Mancuso C. and Vinale F. 1999a. Laboratory testing on a partially saturated soil: equipment, procedures and first experimental results. *Canadian Geotechnical Journal*, 36(1), pp. 1-12.

Richards B.J. 1965. Measurement of the free energy of soil moisture by the pycrometric technique using thermistors. *Moisture equilibria and moisture changes in soils beneathcovered areas, a symposium in print*. Australia, Butterworths, pp. 39-46.

Richard, F. E., Woods, R. E., & Hall Jr, J. R. (1970). *Vibration of soils and foundations*.

Sharma R. S. 1998. *Mechanical behaviour of unsaturated highly expansive clays*. Ph. D. thesis, University of Oxford, U.K.

Silvestri F. 1991. *Analisi del comportamento dei terreni naturali in prove cicliche e dinamiche*. Tesi di dottorato, Univ. di Napoli Federico II

Sivakumar V. 1993. *A critical state framework for unsaturated soils*. Ph.D. Thesis, University of Sheffield, U.K.

- Standard, British. "1377 (1990) Methods of test for soils for civil engineering purposes." British Standards Institution, London (2004).
- Standard, British. "5930, 1999. Code for Practice for Site Investigations." *British Standard Institution, London.*
- Stepkowska, E. T., & Pozzuoli, A. (1990). Microstructure and properties of clays. In *Meeting of the Societa Italiana di Mineralogia e Petrologia, Bologna, (MfORANDI N.(ed.)), in print.*
- Suriol J., Gens A. and Alonso E.E. 1998. Behaviour of compacted soils in suction controlled oedometer. II Int. Conf. on Unsaturated Soils, Beijing, 1, pp. 438-444.
- Tarantino, A. (2009). A water retention model for deformable soils. *Géotechnique* 59, No. 9, 751–762, <http://dx.doi.org/10.1680/geot.7.00118>.
- Terzaghi K. 1936. The shearing resistance of saturated soils and the angle between the planes of shear. Proc. 1st Int. Conf. Soil Mech Found. Eng., 1, pp. 54-56.
- Van Genuchten M.T. 1980. A closed-form equation for predicting the hydraulic conductivity of unsaturated soils. *Soil Science Soc. Am. Journal*, 44, pp. 892-898.
- Vaunat J., Romero E. and Jommi C. 2000. An elastoplastic hydro-mechanical model for unsaturated soils. International Workshop on Experimental Evidence and Theoretical Approaches in Unsaturated Soils, Trento, 10-12 aprile 2000, 121-138.
- Vassallo, R. (2003). Comportamento di terreni costipati non saturi a piccole, medie e grandi deformazioni.
- Vassallo R. and Mancuso C. 2000. Soil behaviour in the small and the large strain range under controlled suction conditions. International Workshop on Experimental Evidence and Theoretical Approaches in Unsaturated Soils, Trento, 10-12 aprile 2000, 75-90.
- Viggiani G. and Atkinson J.H. 1995. Stiffness of fine-grained soil at very small

- strains. *Géotechnique*, 45, 2, 249-265
- Vucetic M. and Dobry R. 1991. Effect of soil plasticity on cyclic response. *Journal of Geotech. Eng. ASCE*, 117(1), 89-107
- Wheeler S.J. and Karube D. 1995. State of the art report: Constitutive modelling. *Proc. I Int. Conf. Unsaturated Soils, Paris*, 3, pp. 1323-1356.
- Wheeler S.J. 1996. Inclusion of specific water volume within an elasto-plastic model for unsaturated soils, *Canadian Geotech. Journ.*, 33(1), pp. 42-57.
- Wheeler, S. J., R. S. Sharma, and M. S. R. Buisson. 2003. "Coupling of hydraulic hysteresis and stress-strain behaviour in unsaturated soils." *Géotechnique* 53 (1): 41-54.
- Wroth C.P. and Houlsby G.T. 1985. Soil Mechanics: Property characterisation and analysis procedures. *Proc. XI Int. Conf. on Soil Mech. and Found. Eng.*, San Francisco, 1, pp. 1-57.
- Wu S., Gray D.H. e Richart F.E. 1984. Capillary effects on dynamic modulus of sands and silts. *Journ. Geotech. Eng. Div., ASCE*, 110(9), pp. 1188-1203.
- Zhang, J., Andrus, R. D., & Juang, C. H. (2005). Normalized shear modulus and material damping ratio relationships. *Journal of Geotechnical and Geoenvironmental Engineering*, 131(4), 453-464.